AD-A113 012 CALIFORNIA UNIV LOS ANGELES DEPT OF MATERIALS SCIEN--ETC F/G 11/6
IDENTIFICATION OF FLAWS RESPONSIBLE FOR CRACK INITIATION AND MI--ETC(U)
FEB 82 G SINES, T OKADA AFOSR-77-3425

UNCLASSIFIED AFOSR-TR-82-0225 NL

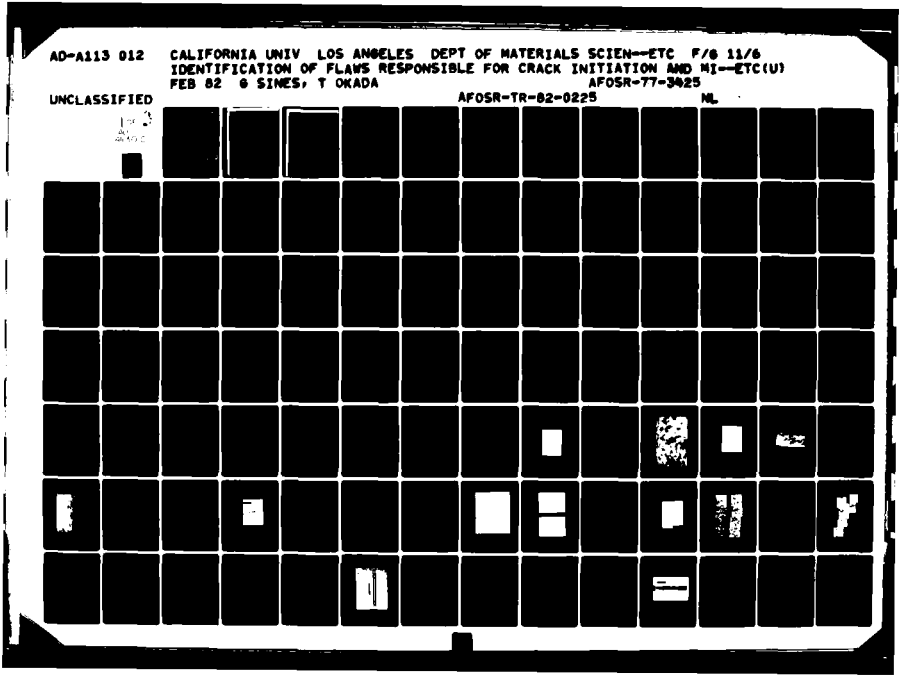

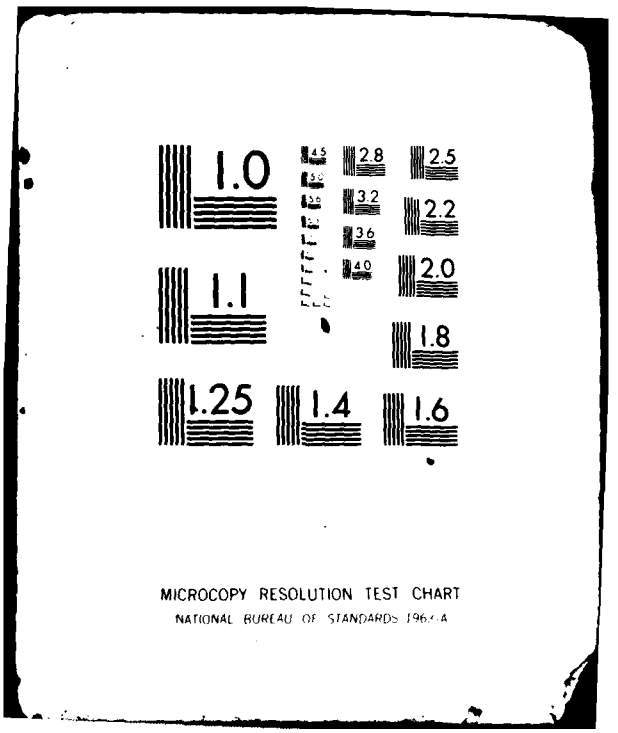
1.0
1.1
1.25
1.4
1.6
1.8
2.0
2.2
2.5
2.8
3.2
3.6
4.0
MICROCOPY RESOLUTION TEST CHART
NATIONAL BUREAU OF STANDARDS 1963-A

UCLA-ENG-82-23
February 1982

FINAL REPORT

Identification of Flaws Responsible for Crack Initiation and Micromechanisms of Slow Crack Growth in the Delayed Fracture of Alumina

by

George Sines

and

Tatsuo Okada

Prepared under contract No. AFOSR 77-3425

for

Air Force Office of Scientific Research

Department of Materials Science and Engineering
School of Engineering and Applied Science
University of California
Los Angeles, California

UNCLASSIFIED

SECURITY CLASSIFICATION OF THIS PAGE *(When Data Entered)*

REPORT DOCUMENTATION PAGE	READ INSTRUCTIONS BEFORE COMPLETING FORM
1. REPORT NUMBER: AFOSR-TR- 82-0225	2. GOVT ACCESSION NO.: AD-A113012
3. RECIPIENT'S CATALOG NUMBER	
4. TITLE *(and Subtitle)*: IDENTIFICATION OF FLAWS RESPONSIBLE FOR CRACK INITIATION AND MICROMECHANISMS OF SLOW CRACK GROWTH IN THE DELAYED FRACTURE OF ALUMINA	5. TYPE OF REPORT & PERIOD COVERED: FINAL REPORT
	6. PERFORMING ORG. REPORT NUMBER: UCLA-ENG-82-23
7. AUTHOR(s): GEORGE SINES, TATSUO OKADA	8. CONTRACT OR GRANT NUMBER(s): AFOSR-77-3425
9. PERFORMING ORGANIZATION NAME AND ADDRESS: UNIVERSITY OF CALIFORNIA, LOS ANGELES, LOS ANGELES, CA 90024	10. PROGRAM ELEMENT, PROJECT, TASK AREA & WORK UNIT NUMBERS: 2306/A2 61102F
11. CONTROLLING OFFICE NAME AND ADDRESS: AFOSR/NE, BOLLING AFB, DC 20332	12. REPORT DATE: FEB 82
	13. NUMBER OF PAGES: 214
14. MONITORING AGENCY NAME & ADDRESS *(if different from Controlling Office)*	15. SECURITY CLASS. *(of this report)*: UNCLASSIFIED
	15a. DECLASSIFICATION/DOWNGRADING SCHEDULE

16. DISTRIBUTION STATEMENT *(of this Report)*

APPROVED FOR PUBLIC RELEASE, DISTRIBUTION UNLIMITED

17. DISTRIBUTION STATEMENT *(of the abstract entered in Block 20, if different from Report)*

18. SUPPLEMENTARY NOTES

19. KEY WORDS *(Continue on reverse side if necessary and identify by block number)*

CRACK INITIATION SLOW CRACK GROWTH, DELAYED FRACTURE, MICROMECHANISMS

20. ABSTRACT *(Continue on reverse side if necessary and identify by block number)*

An eccentricially loaded column testing system was developed to produce a number of crack initiations on the surface of an alumina specimen. Using a specially developed flourescent dye penetration technique, direct observations of early stages of crack extension from inherent flaws were made in the testing system. It was found that a large number of inherent flaws exist on the surface of a ceramic and can, by themselves or as assemblies, become potential crack origins. Cracking sites were found to be multiple in delayed –

DD FORM 1 JAN 73 1473 EDITION OF 1 NOV 65 IS OBSOLETE

UNCLASSIFIED

SECURITY CLASSIFICATION OF THIS PAGE *(When Data Entered)*

fracture. The initial stage of delayed fracture was shown to involve the interaction and coalescence of near-by flaws with extensive intergranular cracking. A model for the delayed fracture, the microscopic slow crack growth and crack interaction and coalescence was proposed. The model gives much better prediction of fracture times than does the conventional single-worst-crack approach. It was found that an assembly of microscopic cracks, which may not be observable, can be much more dangerous than a single macroscopic crack in delayed fracture and that the coalescence of the microscopic cracks may occur in a very short time without being identified because a critical amount of slow crack growth from the individual inherent flaws can be very small.

FOREWORD

This research was performed by the Materials Science and Engineering Department, School of Engineering and Applied Science, University of California, Los Angeles, California under contract numbered AFOSR 77-3425. The program was administered under the direction of Air Force Office of Scientific Research. The contract monitors were first Major W.C. Simmons and later Captain Steven Wax.

This final report describes the work conducted between August 1, 1977 and December 31, 1981. Personnel responsible for carrying out the research program were George Sines and Tatsuo Okada.

ABSTRACT

Direct observation of the early stages of crack extension form inherent flaws is made in order to identify flaws responsible for crack initiation and to study micromechanisms of slow crack growth in the delayed fracture of alumina. Although difficulties are experienced using optical and scanning electron microscopy even with special techniques, a microscopic examination technique is developed to locate the onset of crack extension from inherent flaws using fluorescent dye penetrant and scanning electron microscopy. The specimen surface is immersed in the dye while cracks are forming which allows the dye to penetrate into the fine cracks. Once the cracking sites are located, a high magnification scanning electron microscopy is used for detailed identification of the nature and characteristics of the flaws.

An eccentrically loaded column testing system is developed to produce a number of crack initiations on a surface of a specimen. With this mechanical testing technique, some cracks may propagate dynamically while many cracks are initiating without causing catastrophic failure of the specimen. The testing technique has another significance, that of being able to compare delayed fracture phenomena between tension and compression, since the ratio of tensile and compressive stresses can be precisely controlled.

By combining the microscopic examination technique and the mechanical testing technique, crack origins are identified and micromechanisms of slow crack growth in delayed fracture are studied. A surface of a ceramic contained a large number of inherent flaws which, either by themselves or as assemblies, become potential crack origins. Cracking sites are found to be multiple in delayed fracture. The initial stage of delayed fracture is shown to involve the interaction and coalescence of near-by flaws with extensive intergranular cracking. A model for the

delayed fracture, the microscopic slow crack growth law and the crack interaction and coalescence, is proposed as opposed to the conventional single-worst-crack approach. The proposed slow crack growth law gives much better prediction compared with the conventional approach. It is found that an assembly of microscopic cracks, which may not be observable, can be much more dangerous than a single macroscopic crack in delayed fracture and that the coalescence of the microscopic cracks may occur in a very short time without being identified because a critical amount of slow crack growth from the individual inherent flaws can be very small.

Applicability of existing time-to-failure calculations and the proof testing concepts is reexamined. It is demonstrated that the existing concepts give non-conservative prediction in time-to-failure; but the non-conservative prediction is *partially or sometimes excessively* compensated by conservative estimation of the initial crack size.

Some suggestions for material selection and improvement of resistance to slow crack growth are made based upon findings in the present study. Finally, modes of failure (whether intergranular or transgranular) and slow crack growth in compression are briefly discussed.

TABLE OF CONTENTS

FIGURES

TABLES

CHAPTER I

INTRODUCTION AND SCOPE OF STUDY

I. Introduction

High strength ceramics have begun to play an important role as load bearing structural materials because of their high chemical and physical stabilities over a wide range of temperature. Among some of the strength limiting factors such as brittleness and high temperature creep, stress corrosion cracking from inherent flaws is a critical one to be considered when ceramics are used for an extended period of time.

The phenomenon of environment assisted fatigue crack growth--a time dependent fracture process--is known to exist for most engineering materials. The phenomenon is called stress corrosion cracking, static fatigue, or delayed fracture; and it can be defined as "environmentally induced subcritical crack growth under dynamic or static loading." An adverse environment may contain a variety of chemical species which react with the material, such as hydrogen for metallic and water for ceramic materials. Theories and experimental results of subcritical crack growth have been studied extensively and reviewed.[1-6]

The linear elastic fracture mechanics approach proved to be applicable in studying fracture of ceramics, both instantaneous and delayed fracture. Since the fracture

mechanics relates fracture strength with crack size and shape, the study of crack origins especially their nature and size became essential in order to understand fracture behavior. Crack origins have been studied by examining the fracture surfaces; however, it is often found that the origins are very difficult to find in certain classes of ceramics such as alumina studied in the present research. Therefore, it was thought necessary to observe the onset of crack extension from inherent flaws in order to locate crack origins exactly.

The direct observation of the initial stage of crack growth from inherent flaws is important not only because the crack origins can be identified but also the micro-mechanisms of crack growth may be determined. Study of subcritical crack growth has been conducted using special specimens, double torsion or double cantilever beam specimens, which contain macroscopic precracks. There has been a controversy whether the macroscopic crack growth in those specimens is the same as the microscopic crack growth in the bending specimens in the delayed fracture tests.

In the fracture of ceramics, the critical crack size is very small even in delayed fracture, where applied stresses are generally smaller than the fracture strength of the material. When a crack is small, in a microscopic dimension, it may grow differently from a macroscopic crack due to factors such as the residual stresses from thermal

expansion anisotropy and from machining, the local heterogeneity of grain orientation, the strength anisotropy of different crystal planes, and the interaction of preexisting flaws. Therefore, the validity of direct extrapolation of macroscopic crack growth data to microscopic crack growth becomes questionable. It is thus convenient to divide the process of delayed fracture into two stages: the microscopic crack growth stage and the macroscopic crack growth stage. The former involves crack extension from inherent flaws under the influence of the factors mentioned previously. The microscopic crack growth stage ends when a crack becomes sufficiently large that the microstructural effect is negligible. The macroscopic crack growth stage is characterized by the well-established slow crack growth law given by

$$da/dt = B(K/K_{IC})^n \qquad (1\text{-}1)$$

provided that there are no macroscopic crack interactions. The macroscopic crack growth stage has been studied extensively by many investigators. However, it is the microscopic crack growth stage that controls the time-to-failure in delayed fracture in ceramics since the critical crack size is in a microscopic dimension. Therefore, detailed observation of crack initiation and propagation from inherent flaws becomes essential.

The objectives of the present study are to identify the flaws responsible for the initiation of subcritical crack growth and to determine the micromechanisms of crack growth by directly observing the onset of crack growth from inherent flaws in the delayed fracture of alumina.

2. Scope and Chart of the Dissertation

In order to achieve the objectives--identification of flaws and determination of the micromechanisms of crack growth--a microscopic examination technique to observe the onset of crack extension from the inherent flaws and a mechanical testing technique to create many crack extensions had to be developed.

The scope of the present dissertation is the following:

(1) Description of the microscopic examination technique to reveal the early stage of crack extension from the inherent flaws using fluorescent dye penetrant and scanning electron microscopy,

(2) Description of the mechanical testing technique, the eccentrically loaded column testing, which induces many crack extensions on a surface of a specimen without causing catastrophic failure of the specimen,

(3) Identification of crack origins and determination of the micromechanisms of crack growth in the delayed fracture of a dense alumina.

Fracture mechanics of brittle materials and static fatigue of glasses and ceramics will be reviewed in Chapter II, and some problem areas will be identified. The new microscopic examination technique to reveal crack origins will be described in Chapter III. The mechanical testing

technique to create many cracks will be introduced in Chapter IV. The inherent flaws responsible for the initiation of slow crack growth will be identified, and the micromechanisms of slow crack growth and the time-to-failure based upon the proposed model will be discussed in Chapter V. Finally, the concluding remarks will be made in Chapter VI.

CHAPTER II

BACKGROUND AND LITERATURE

1. Fracture Mechanics of Brittle Materials

The observed tensile fracture strength of a brittle material is much lower than its theoretical strength derived from the atomic cohesive strength. The large discrepancy between the actual and theoretical strength was first explained by using the concept of stress concentration at a crack tip. Inglis[7] in 1913 obtained the maximum stress at a crack tip, by analyzing a plate containing an elliptical hole under uniaxial tensile stress applied perpendicular to the major axis, as follows:

$$\sigma_{max} = \sigma[1 + 2(\frac{a}{\rho})^{1/2}] \qquad (2\text{-}1)$$

$$\simeq 2\sigma(\frac{a}{\rho})^{1/2} \qquad \text{for } a >> \rho$$

where σ_{max} = maximum stress at the end of the major axis

σ = applied stress

a = half major axis of the ellipse

ρ = radius of curvature at the crack tip

In 1920, Griffith[8] formulated a fracture criterion based upon energy balance. The elastic strain energy per unit thickness of a cracked body can be expressed, using the stress analysis by Inglis[7] in plain strain, as follows:

$$U = 4a\gamma_s - \frac{\pi\sigma^2 a^2}{(1-\nu^2)E} + U_o \qquad (2\text{-}2)$$

where U = the elastic strain energy per unit thickness of the plate containing an elliptical crack of length a

U_o = the elastic strain energy per unit thickness of the plate without the crack

σ = applied stress

a = one-half crack length

E = modulus of elasticity

γ_s = surface energy

ν = Poisson's ratio

By applying the equilibrium condition

$$\frac{\partial U}{\partial a} = 0 \qquad (2\text{-}3)$$

the Griffith fracture criterion can be written as follows:

$$\sigma_f = \left[\frac{2E\gamma_s}{\pi a(1-\nu^2)}\right]^{1/2} \qquad (2\text{-}4)$$

where σ_f = the fracture strength.

Equation (2-4) is a necessary condition for elastic crack propagation in brittle fracture. The energy balance

concept was later modified by Orowan[9] to include the energy absorbed by plastic deformation

$$\sigma_f = \left[\frac{2E(\gamma_s + \gamma_p)}{\pi a(1 - \nu^2)}\right]^{1/2} \qquad (2\text{-}5)$$

where γ_p = plastic deformation energy

Also at the same time, it was modified by Irwin[10] who used the notion of the strain energy release rate,

$$\sigma_f = \left[\frac{2EG}{\pi a(1 - \nu^2)}\right]^{1/2} \qquad (2\text{-}6)$$

where G = the strain energy release rate = $\frac{\partial U}{\partial a}$

Meanwhile, there was another approach to the crack problem. Westergaard[11] was able to determine the nature of the crack tip stress field using Airy stress functions. The stress fields around a crack tip can be divided into three major modes of loading[12] which involve different crack surface displacement as shown in Fig. 2-1, and the stresses for the notation given in Fig. 2-2 can be expressed as follows:

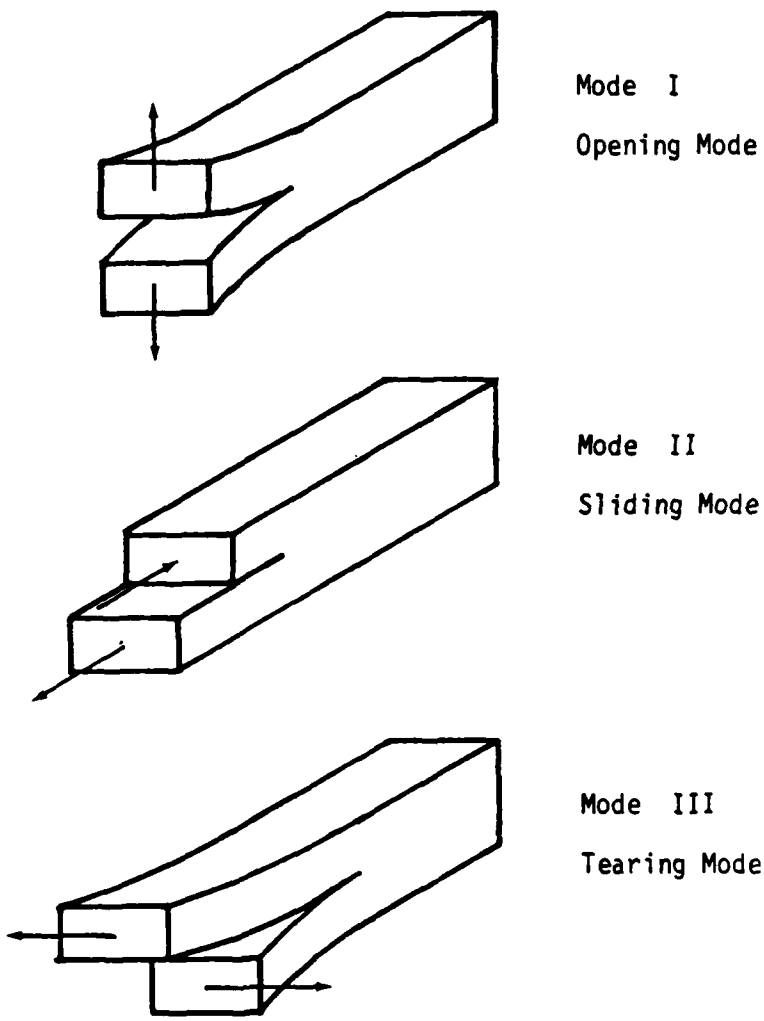

Fig. 2-1. Modes of Fracture.

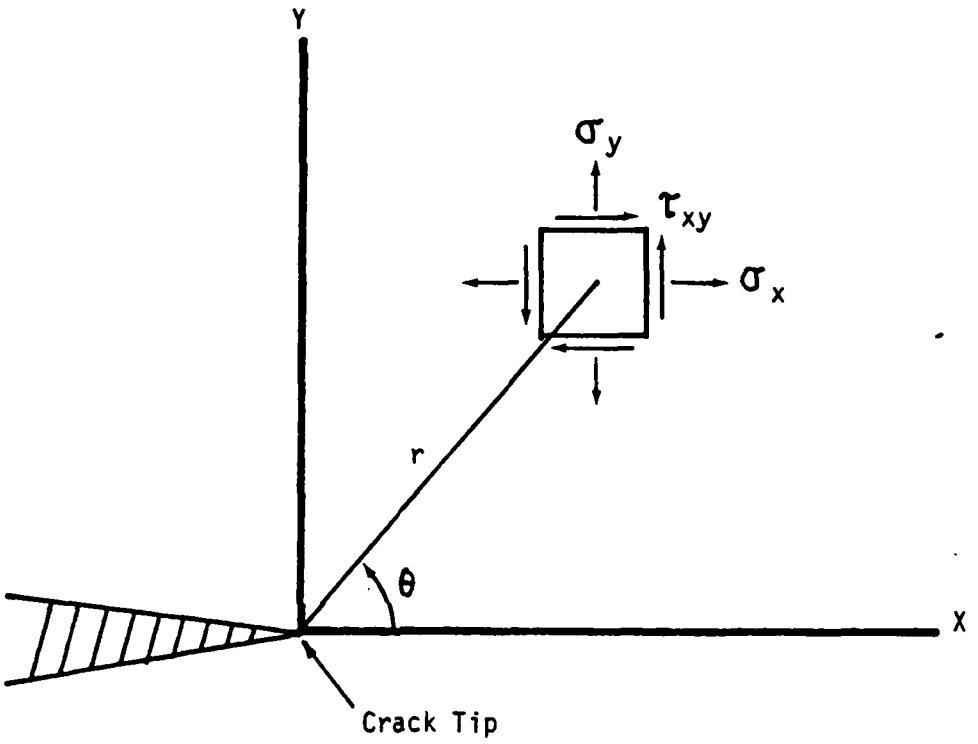

Fig. 2-2. The Notation for the Stresses Near Crack Tip.

$$\sigma_x = \frac{K_I}{\sqrt{2\pi r}} \cos(\frac{\theta}{2}) [1 - \sin(\frac{\theta}{2}) \sin(\frac{3\theta}{2})]$$

$$- \frac{K_{II}}{\sqrt{2\pi r}} \sin(\frac{\theta}{2}) [2 + \cos(\frac{\theta}{2}) \cos(\frac{3\theta}{2})] + \ldots$$

$$\sigma_y = \frac{K_I}{\sqrt{2\pi r}} \cos(\frac{\theta}{2}) [1 + \sin(\frac{\theta}{2}) \sin(\frac{3\theta}{2})]$$

$$+ \frac{K_{II}}{\sqrt{2\pi r}} \sin(\frac{\theta}{2}) \cos(\frac{\theta}{2}) \cos(\frac{3\theta}{2}) + \ldots \qquad (2\text{-}7)$$

$$\tau_{xy} = \frac{K_I}{\sqrt{2\pi r}} \cos(\frac{\theta}{2}) \sin(\frac{\theta}{2}) \cos(\frac{3\theta}{2})$$

$$+ \frac{K_{II}}{\sqrt{2\pi r}} \cos(\frac{\theta}{2}) [1 - \sin(\frac{\theta}{2}) \sin(\frac{3\theta}{2})] + \ldots$$

where K_I = stress intensity factor in Mode I

K_{II} = stress intensity factor in Mode II

When $K_{II} = 0$, Irwin[13] showed that for plain strain under uniaxial tension

$$G = \frac{(1 - \nu^2) K_I^2}{E} \qquad (2\text{-}8)$$

Therefore, the energy balance approach and the stress intensity factor approach are essentially equal under uniaxial tension. In this dissertation the notion of the stress intensity factor will be used extensively. Then the fracture criterion becomes

$$K = K_{IC} \tag{2-9}$$

where K_{IC} = critical stress intensity factor or fracture toughness which is a material constant

The stress intensity factor is a function of the applied stress, crack length, and crack and loading geometry; and it can be expressed for simple cases as

$$K = Y\sigma\sqrt{a} \tag{2-10}$$

where Y = geometrical constant

For specific crack and loading configurations, one can refer to existing handbooks such as Rooke and Cartwright.[14] Since the critical stress intensity factor is a material constant, the fracture stress can be predicted if the applied stress and the crack size are known. The stress intensity factor approach, the linear elastic fracture mechanics, serves as an important tool for quantitative understanding of fracture mechanics of brittle materials.

Another fracture criterion discussed earlier in this chapter, the stress concentration factor approach, was used for a crack problem under biaxial loading by Griffith[15] in 1924. In biaxial stress condition, the potential energy expression was not available then, and Griffith failed to use the energy balance concept established earlier.

Griffith showed that the uniaxial compressive strength was eight times the uniaxial tensile strength assuming a sharp elliptical crack in a plate. This approach was later extended by Babel and Sines,[16] and successfully applied to a porous ceramic material. It should be noticed that the maximum stress criterion is more applicable when there is a very small process zone at a crack tip.

The above discussed fracture criteria can be modified to predict the time-dependent aspect of brittle fracture as will be shown in the later sections.

2. Static Fatigue

Delayed fracture of glass is by no means a recent problem. The phenomenon was reported as early as in 1899 by Grenet,[17] who observed stress rate dependence of the strength of a glass and delayed fracture after some time under a sustained load. At that time French champagne makers probably had a working experience on delayed fracture; they never refilled their bottles a second time in order to avoid explosion of bottles of precious Seltzer water. Since then, many theories and experimental results have been published to explain the phenomena of delayed fracture. In the following sections, the theories and experimental methods and results will be briefly reviewed. For more details, one can refer to rather complete review papers available today.[1-6]

2.1 Theories of Static Fatigue

Theories of static fatigue were developed initially based upon delayed fracture of glasses. Poncelet[18] amended the Griffith theory, assuming that cracks nucleate in flaw-free surface of a glass due to the conjoint action of applied stresses and thermal fluctuations within the glass. His theory was, therefore, based upon the thermal agitation and wave propagation. The time-to-failure is the time necessary for crack propagation. Murgatroyd[19] derived an expression for time dependence of the strength of glass assuming that Griffith flaws consist of pockets of quasi-viscous material and yield with time as stressed. Taylor[20] showed that the rate-controlling factor for the delayed fracture is the activation energy for the orientation or rearrangement of the atomic network under an applied stress. Stuart and Anderson[21] derived an expression for crack velocity in terms of the rate of breaking chemical bonds, dN/dt; where N is the number of chemical bonds. The equations fit very well with the experimental results obtained by Mould and Southwick[22] and are nearly identical to the ones derived from chemical reaction theory by Charles and Hillig.[23]

The chemical reaction theory was later extended to brittle crystalline solids by Hillig and Charles,[24] and it is generally accepted as a theory of static fatigue of glass and ceramics. They considered changes in crack tip geometry due to stress enhanced chemical reaction as shown in

Fig. 2-3. The theory was derived assuming the following:

(1) the reaction rate is not controlled by the transport of reactant to the reaction sites,

(2) the reaction between the solid and the chemical species in the environment is stress dependent, and

(3) the activation energy is derived from an Arrhenius plot of the corrosion rate versus temperature and is a function of the local tensile stress.

Then the local velocity normal to the surface is given in the following form:

$$v = v_o \exp(-E^* - \gamma V_m/\rho + \sigma V^*)/RT \qquad (2\text{-}11)$$

where v = local velocity normal to the surface of the crack

v_o = preexponential kinetic factor

E^* = experimental activation energy in absence of stress

γ = interfacial surface energy between the original material and reaction product

V_m = the molar volume of the material

ρ = the radius of curvature of the crack tip

σ = the local stress

V^* = the activation volume

R = gas constant = 1.987 cal/mol-deg

T = absolute temperature.

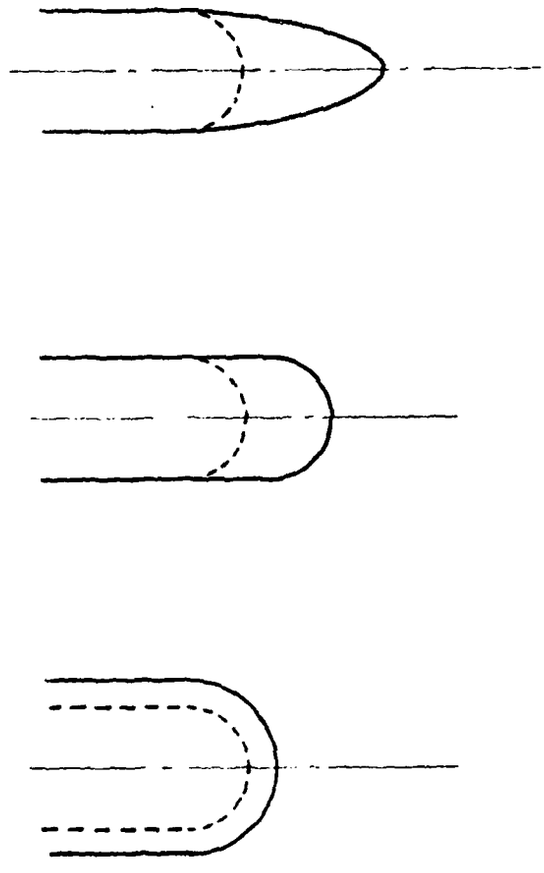

(a) Crack Tip Radius Decreases with Time. (Crack Tip Sharpening)

(b) Crack Tip Radius Stays Constant with Time.

(c) Crack Tip Radius Increases with Time. (Crack Tip Blunting)

Fig. 2-3. Change in Crack Tip Geometry.[24]

The factors tending to increase the stress concentration at the crack tip are increased driving force and decreased activation energy due to local tensile stresses. The factors tending to decrease the stress concentration at the crack tip are thermodynamic driving force due to increase in crack tip curvature and plastic or visco-elastic relaxation. Assuming an initial flaw geometry being an ellipse, and using Muskhelishivili's[25] stress distribution around an ellipse, they were able to derive an expression for the total time-to-failure. They defined the fatigue limit as a critical applied stress for which the stress concentration at the crack tip remain constant with time.

The Charles and Hillig equation was modified by Wiederhorn and Boltz,[26] who used the stress intensity factor to express local stress instead of the stress concentration factor. For a two-dimensional Griffith crack, the local stress at the crack tip can be expressed using the stress intensity factor in the following form:

$$\sigma = \frac{2K_I}{(\pi\rho)^{1/2}} \qquad (2\text{-}12)$$

where K_I = stress intensity factor in Mode I

ρ = radius of curvature at the crack tip

Equation (2-12) has a significance of relating the maximum local stress and stress intensity factor. Combining eq. (2-11) and eq. (2-12), Wiederhorn and Boltz rewrote the

expression for the local crack velocity as follows:

$$v = v_o \exp\left[-E^{**} + 2V^* K_I/(\pi\rho)^{1/2}\right]/RT \qquad (2\text{-}13)$$

where $E^{**} = E^* + \gamma V_m/\rho$

Both eq. (2-11) and (2-13) contain the radius of curvature; therefore, crack sharpness is an important factor for determination of the fracture strength. Importance of crack sharpening effect in addition to lengthening was reemphasized by Doremus[27] recently.

2.2 Experimental Observations of Static Fatigue

Static fatigue data can be presented by three different fatigue curves: the failure strength versus the logarithm of the time-to-failure[28-30] as shown in Fig. 2-4, the universal curve[22,31] as shown in Fig 2-5, and the logarithm of crack velocity versus the stress intensity factor[31-33] as shown in Fig. 2-6. The last one is by far the most common method to describe static fatigue of ceramics. The experimental data are taken from double cantilever beam or double torsion specimens, and DT specimens are widely used due to ease of taking measurements in different environments. Detail description of the DT test was published by Evans.[31]

In region I of Fig. 2-6, the slow crack growth is due to a stress enhanced chemical reaction between the material and the environment, and the empirical relation can be expressed as follows:

$$\frac{da}{dt} = v = A K_I^n \qquad (2\text{-}14)$$

where $da/dt = v$ = crack velocity

A = constant

n = crack growth exponent

K_I = stress intensity factor in Mode I

or it can be expressed[34,35] as follows:

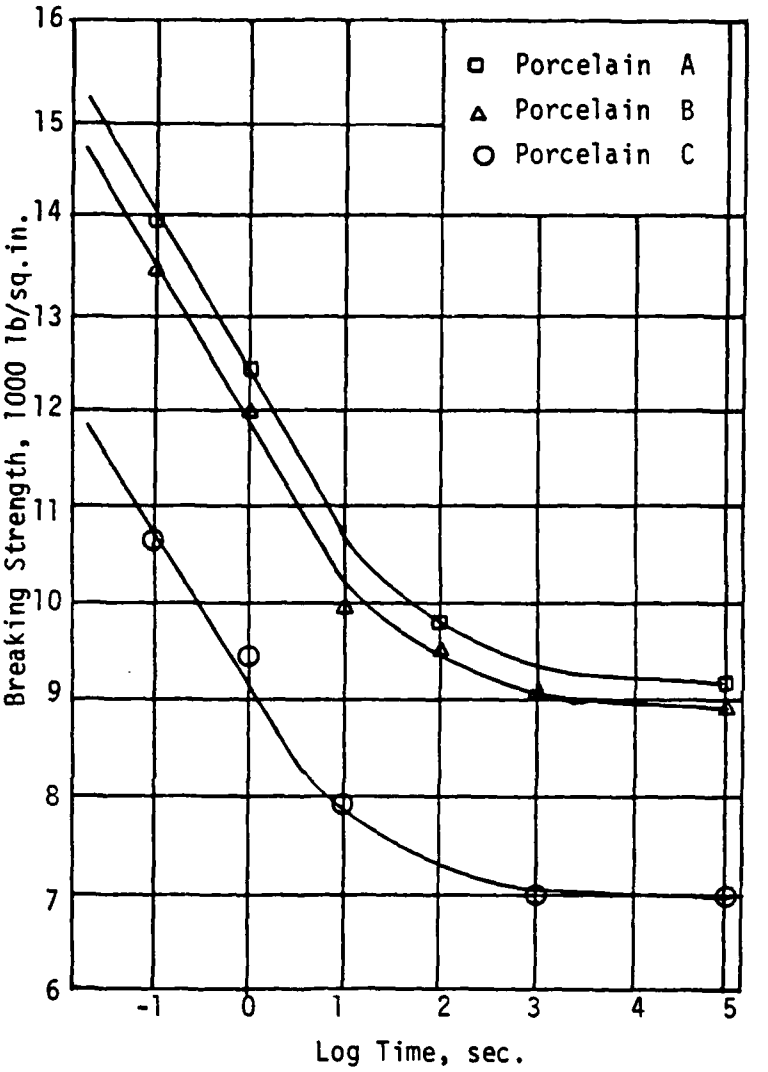

Fig. 2-4. Breaking Strength versus Time-to-Failure.[6]

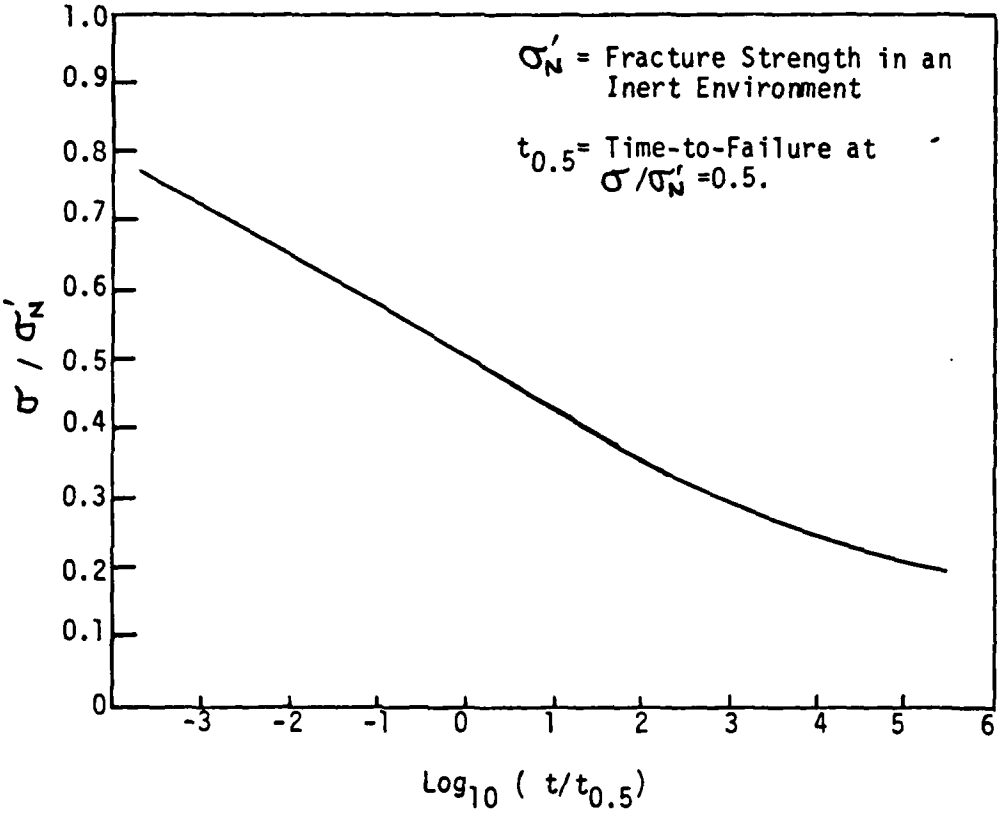

Fig. 2-5. Universal Fatigue Curve.[22]

Notice that a single curve was obtained from six different surface conditions by normalizing the data.

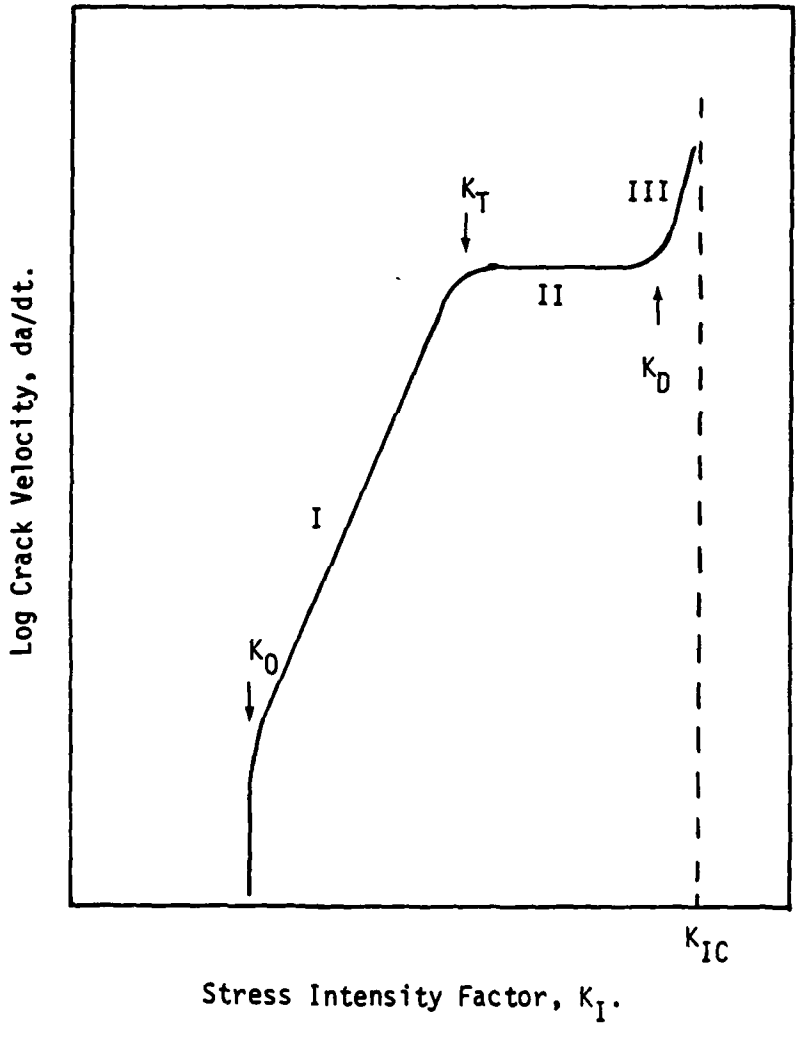

Fig. 2-6. Crack Velocity versus Stress Intensity Factor.[31]

$$\frac{da}{dt} = v = B\left(\frac{K_I}{K_{IC}}\right)^n \qquad (2\text{-}15)$$

where B = constant

In region II, the crack velocity is nearly independent of the stress intensity factors, but strongly dependent upon the amount of reactive species in the environment. It is believed that the rate controlling factor in this region is the rate of transport of the species to the crack tip. The crack velocity in this region is constant and can be written as

$$\frac{da}{dt} = v' \qquad (2\text{-}16)$$

where v' = constant

In region III, crack growth is rapid and due to purely mechanical failure; therefore, it is independent of the environment.

The constants A, B, v', and n are used to predict the time-to-failure for a particualr combination of the applied stress and the environment provided that the initial crack size is known or assumed.

The effect of different environments is readily shown in Fig. 2-7; the crack velocity is also dependent on temperature[36] and grain size[37] as shown in Fig. 2-8 and

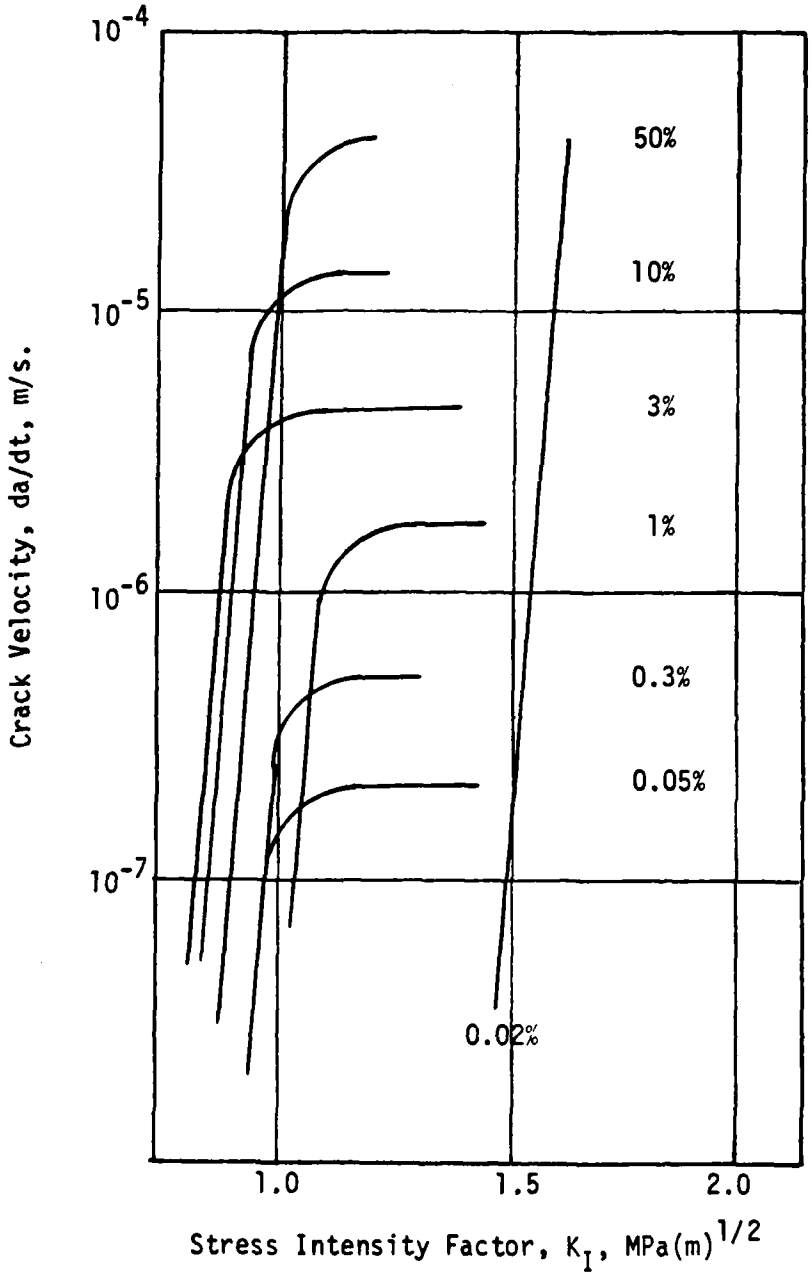

Fig. 2-7. Environment Dependence of Crack Velocity.[4]

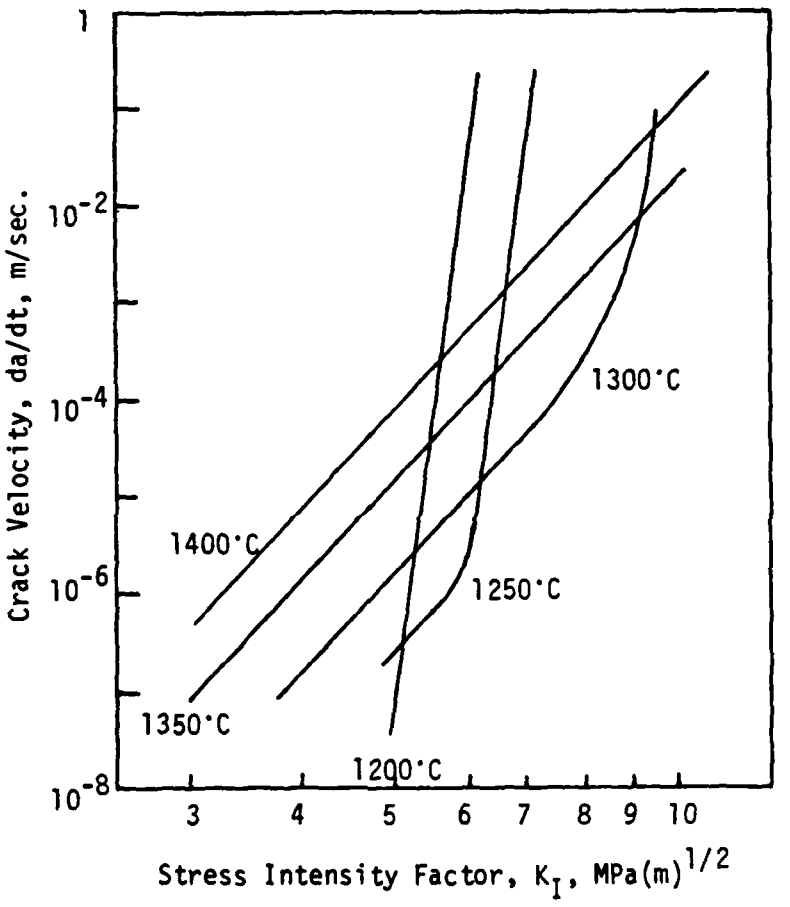

Fig. 2-8. Temperature Dependence of Crack Velocity.[36]

Fig. 2-9 respectively. Notice that in Fig. 2-9 the large grained aluminas have higher resistance to crack growth as well as higher fracture energy than the small grained aluminas. It is contrary to what was expected since fine grained materials are generally stronger. The reason why the larger grained aluminas have higher fracture energy than the small grained aluminas has not been fully explored.

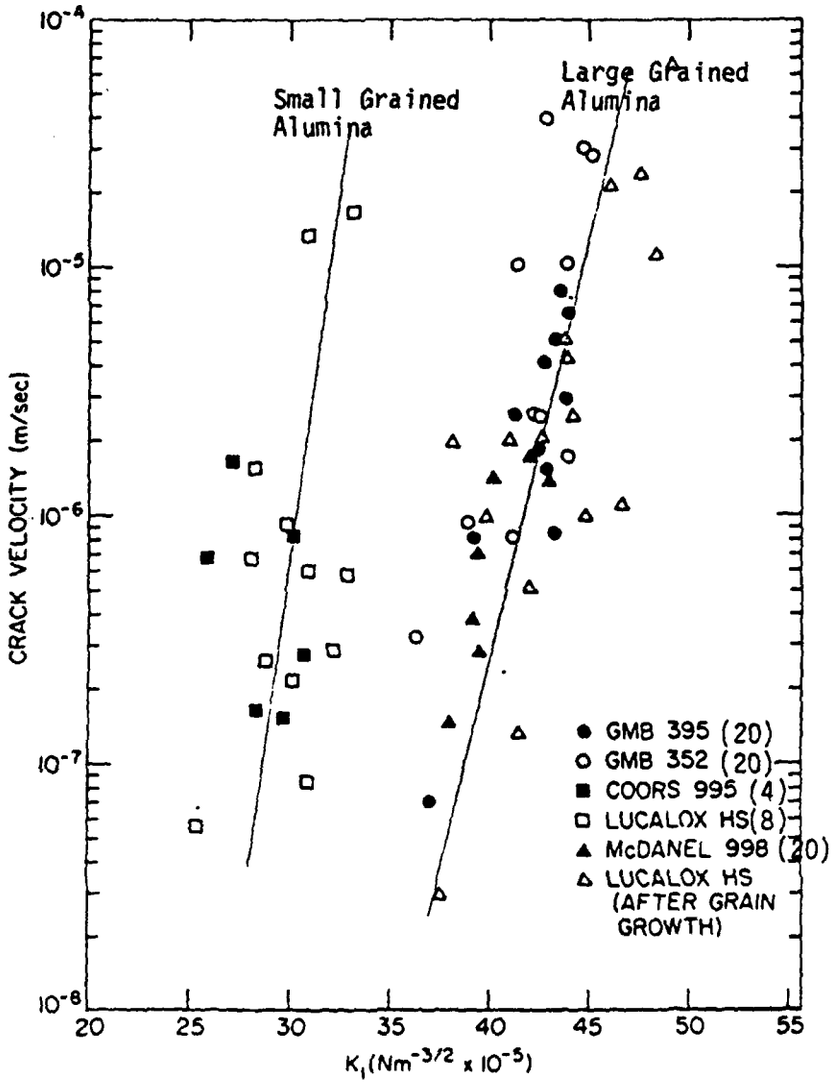

Fig. 2-9. Grain Size Dependence of Crack Velocity.[37]

2.3 Time-to-Failure Prediction

After the constants are evaluated from double torsion tests, the time-to-failure under a constant applied stress can be calculated (see Appendix A). Assuming that most of the life is spent in region I, the time-to-failure can be given as follows:

$$t_f = \frac{2K_{IC}^n}{Y^2\sigma^2 B(n-2)K_{Ii}^{n-2}} \qquad (2\text{-}17)$$

where t_f = time-to-failure

K_{IC} = critical stress intensity factor

K_{Ii} = initial stress intensity factor

σ = applied stress

Y = geometrical constant

It is important to realize the assumptions made to derive the expression in eq. (2-17), they are:

(1) a single worst flaw propagates according to the crack growth law given in eq. (2-15),

(2) a crack does not propagate until the applied stress reaches σ,

(3) the macroscopic crack growth law, in which artificially induced macroscopic cracks propagate, is directly applicable to the microscopic crack growth in delayed fracture.

Since it is difficult, if not impossible, to measure the initial crack size, the proof test[38] can be used to estimate the maximum possible initial crack size (see Appendix A). The time-to-failure after the proof test is given by

$$t_f = \frac{2K_{IC}^2 \sigma_p^{n-2}}{Y^2 \sigma^n B(n-2)} \tag{2-18}$$

where σ_p = the proof stress

Since the concept is conservative, the stress level of the proof test should be sufficiently high that a few specimens fail during the proof test. This concept was applied to predict life time of the Space Shuttle window.[39]

When time-to-failure is short, dynamic loading condition should be taken into account.[40] In other words, cracks can propagate during loading. Using this concept, an expression for the observed fracture strength in constant stress rate experiment has been derived in terms of the stress rate and the initial strength in the absence of subcritical crack growth (see Appendix A) as follows:

$$\sigma_f = \left\{\frac{2\dot{\sigma}K_{IC}^2(n+1)\sigma_f^{*(n-2)}}{BY^2(n-2)}\right\}^{\frac{1}{n+1}} \tag{2-19}$$

or

$$\sigma_f^* = \left\{\frac{BY^2(n-2)\sigma_f^{n+1}}{2\dot{\sigma}K_{IC}^2(n+1)}\right\}^{\frac{1}{n-2}} \tag{2-20}$$

where σ_f = observed fracture strength

σ_f^* = initial strength in the absence of sub-critical crack growth

$\dot{\sigma}$ = the stress rate

Equation (2-20) can be used to estimate the initial stress intensity factor. This will be combined with the statistical nature of brittle fracture to generate strength-probability-time relationships in the following section.

2.4 Statistical Aspect of Time-to-Failure

Brittle materials exhibit statistical distribution in fracture strength. Figure 2-10 shows a typical flexural strength distribution of alumina obtained by Chen.[41] Using the Weibull-type[42] distribution, the cumulative failure probability can be expressed as follows:

$$P = 1 - \exp\left[-\left(\frac{\sigma_f - \sigma_u}{\sigma_v}\right)^m\right] \qquad (2\text{-}21)$$

where P = the cumulative failure probability

σ_f = the observed fracture strength

σ_u = the stress below which fracture does not occur

σ_v = normalizing constant

m = Weibull modulus.

The cumulative failure probability can be determined experimentally by

$$P = i/(N+1) \qquad (2\text{-}22)$$

where i = the rank of the specimen

N = the total number of measurements.

In order to evaluate σ_u and m, the logarithm of eq. (2-21) was taken twice, which yields

$$\log\log[1/(1-P)] = m\log(\sigma_f - \sigma_u) + C \qquad (2\text{-}23)$$

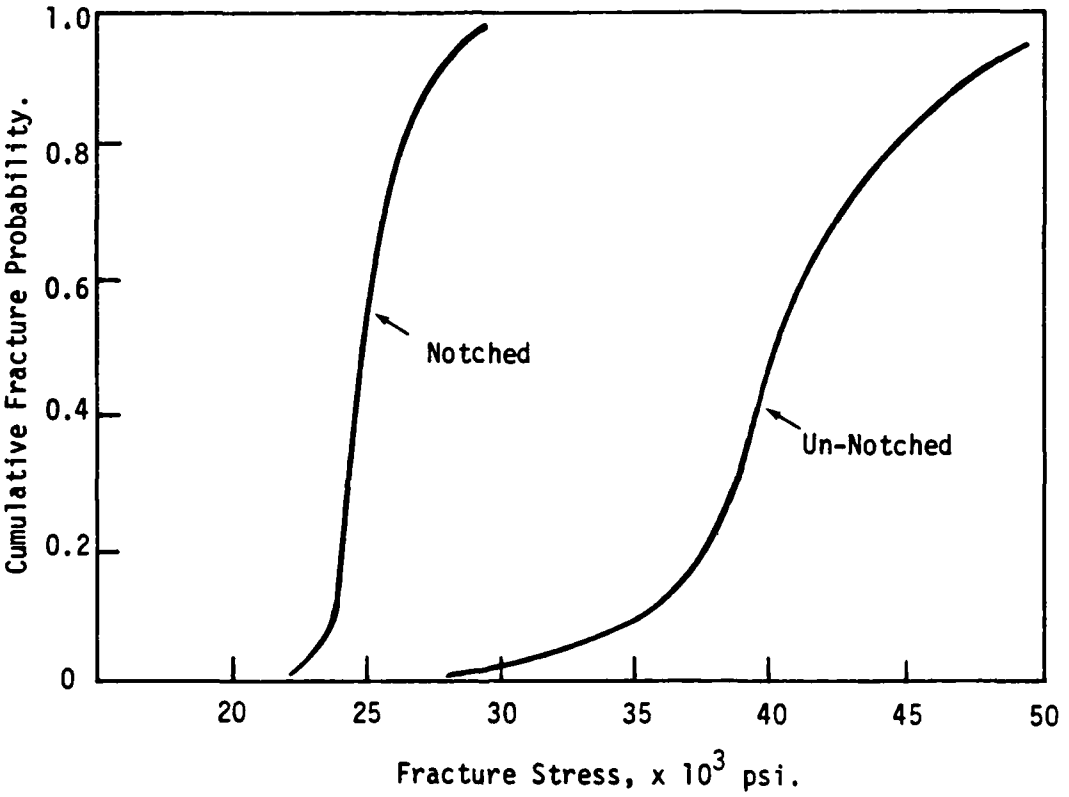

Fig. 2-10. Flexural Strength Distribution of Alumina.[41]

where $C = \log \log e - m \log \sigma_v$

and $\log \log [1/(1-P)]$ is plotted against $\log(\sigma_f - \sigma_u)$. By adjusting the value of σ_u, a straight line should be obtained; the slope of the line is m. The value of m should be used together with the average fracture strength of the material in order to properly estimate the mechanical performance of the material. The larger the value of m, the less scatter in strength; therefore, there is less size effect.

When the statistical distribution is taken into account, time-to-failure can be expressed as follows (see Appendix A)

$$\log t_f = \log \frac{1}{\sigma^n (n+1) \dot{\sigma}} + \frac{n+1}{m} \{\log \log [1/(1-P)] - C\} \tag{2-24}$$

This relationship is called the strength-probability-time (SPT) relation.

Davidge[43] showed that for different strain rates, $\dot{\varepsilon}_1$ and $\dot{\varepsilon}_2$, fracture strength σ_1 and σ_2 are related as

$$\left(\frac{\sigma_1}{\sigma_2}\right)^{n+1} = \frac{\dot{\varepsilon}_1}{\dot{\varepsilon}_2} \tag{2-25}$$

Equation (2-25) may be used to obtain the value of n from three- or four-point bending tests instead of from the DT tests.

2.5 Problem Areas

In calculating the time-to-failure using the linear elastic fracture mechanics such as eq. (2-17), some areas of uncertainty exist. Ones that are discussed here are:

(1) K_{IC} is not a constant but depends upon the testing method and the crack-to-grain size ratio when the crack is small,

(2) the crack growth exponent obtained in the constant strain rate experiment, eq. (2-25), is usually different from the one obtained in slow crack growth experiment, eq. (2-14),

(3) discrepancy has been reported between the calculated and observed time-to-failure in the long life regime, and

(4) the simplistic assumption that a single worst flaw propagates according to the macroscopic crack growth law is not valid when there are many inherent flaws close together.

Use of the linear elastic fracture mechanics requires precise evaluation of the critical stress intensity factor which is supposed to be a material constant. However, there have been some discrepancies reported in K_{IC} values resulting from different testing methods for large grain size materials,[44-47] also resulting from different crack-to-grain size ratio[48-51] recently. The schematic drawing in Fig. 2-11 illustrates a functional relationship between the

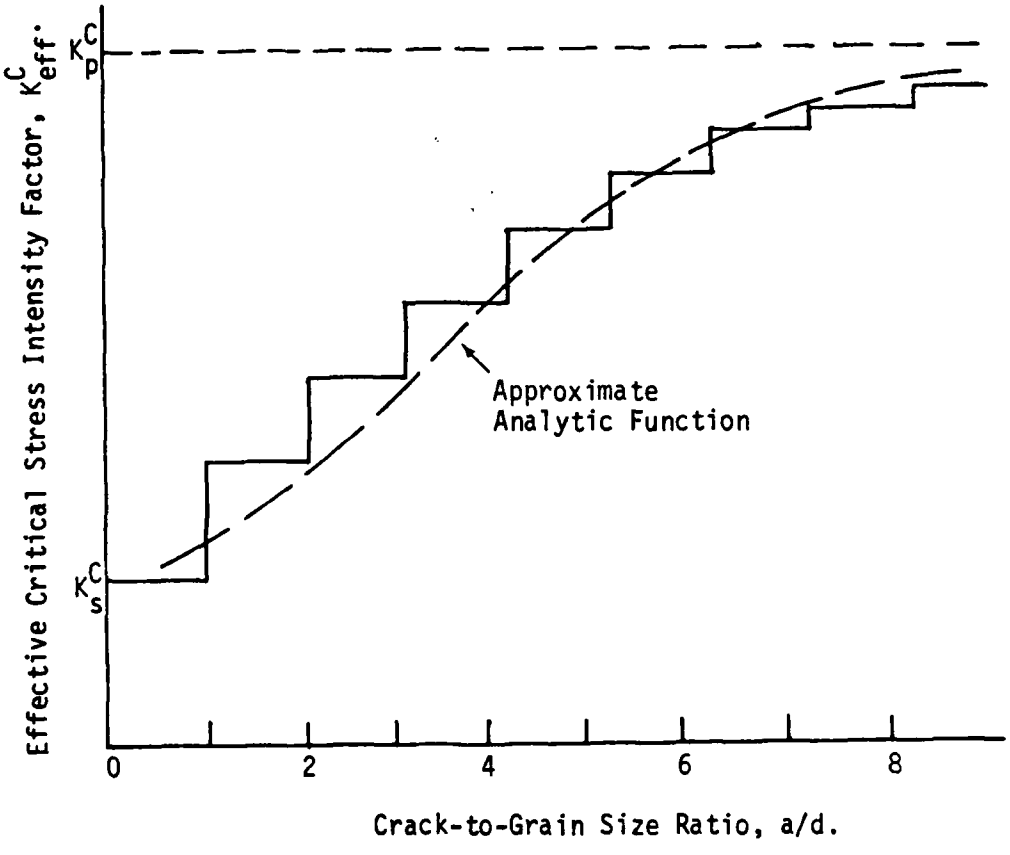

Fig. 2-11. Schematic Drawing of Variation in Effective Critical Stress Intensity Factor, K^C_{eff}, with Crack Length Relative to Grain Diameter, a/d.[49]

effective critical stress intensity factor and the crack-to-grain ratio. Evans[49] showed the emergence of a $d^{-1/2}$ dependence of strength as a natural law for fracture in the coarse-grained ceramics, and Virkar et al.[51] demonstrated that the potential for stable crack growth preceding fracture in polycrystalline ceramics depends upon the functional relationship between the local toughness and the crack length. Davidge et al.[43] found that values of n obtained from bending tests were different from the values obtained from double torsion tests. They pointed out the discrepancy is due to a difference in crack growth behavior between a micro- and macro-crack. Soma et al.[52] reported a discrepancy between a calculated and the observed time-to-failure in long-life regime, $t_f > 1000$ sec. They calimed that there is a need for a new crack growth law in that regime. A surface of a ceramic material contains many inherent flaws either intrinsic or extrinsic. When a large surface area is stressed, those cracks and flaws tend to interact to result in a different stress intensity factor. Therefore, the simplistic assumption of a single worst flaw does not apply any more. Although crack interaction and coalescence behavior has been studied statistically[53,54] and mathematically,[55-57] and more recently the concept was applied to ceramic fracture and slow crack growth,[58,59] the direct observation of crack extension from inherent flaws and the analysis of time-to-failure using the concept have not been done.

CHAPTER III

MICROSCOPIC EXAMINATION TECHNIQUE

It is generally accepted that fracture of a brittle material originates at inherent flaws. By examining a fracture surface, sometimes an obvious origin of the crack can be found; it is often a large void, an inclusion, or a machining crack.[60-62] Sometimes a crack origin can be found by carefully studying topographical features on the fracture surface such as pore tails, cleavage steps, fracture mirrors,[63-65] gull-wings, rib marks, and Walner lines.[66] However, sometimes ceramics exhibit no obvious features on the fracture surface so that identification of crack origins is impossible. Chung[67] was able to locate an area from which a crack grew by examining the microbranching with a fluorescent dye penetrant.

While the above mentioned techniques are sometimes powerful in locating crack origins, direct observation of the on-set of crack growth from inherent flaws is essential in order to identify the nature and characteristics of flaws responsible for the initiation of cracking and to study micromechanisms of slow crack growth in delayed fracture. Crack extension from inherent flaws is extremely difficult to observe, unlike crack propagation from a machined notch or an artificially induced crack, not only because there are too many flaws for the microscopic examination as re-

reported by Noone and Mehan[68] but also because cracks are small and tightly closed.

In addition to conventional optical and scanning electron microscopy, other techniques were used in this study. They were fluorescent dye penetrant or special illumination systems such as Leitz Ultropak for the optical microscopy and crack decoration by silver nitrate solution for the scanning electron microscopy. Since there is no need to explain conventional optical and scanning electron microscopy, only the latter three techniques will be described in this chapter. Difficulties experienced in locating the onset of crack extension from the inherent flaws and a solution to the problems will also be presented in this chapter.

1. The Fluorescent Dye Penetrant Technique

The fluorescent dye used in this study is a commercially available product, ZYGLO ZL-54.[69] ZL-54 is fluorescent, ultra-high sensitive, water-washable penetrant. It is composed of petroleum solvents, surface active agents, and fluorescent dyes. Available information on its properties is given in Table 3-1.

The basic principle is to let the fluorescent dye penetrate into a crack, and then by irradiating the area with an ultraviolet light to excite another light in a visible range, so that the existence of the crack can be revealed. The procedures are very simple as follows:

(1) Precleaning a specimen with an ultrasonic cleaner with acetone first, then with water,

(2) Drying the specimen by blowing air,

(3) Applying the fluorescent dye on a surface of the specimen by brushing while the specimen is on a hot plate at 50-70°C,

(4) Keeping the specimen on the hot plate for 15-30 minutes to allow dye penetration,

(5) Rinsing by running tap water to remove excess dye on the surface for 20-30 seconds with controlled water pressure of 30-50 psi,

(6) Drying by blowing air--hot air can be used but never more than 100°C to avoid excess dryness,

Table 3-1 Properties of ZL-54

Viscosity at 37.8°C	10.1 cs
Flash Point	>93.3°C(P.M.C.C.)
Density	949 gms/l
Water Tolerance	27.0%
Sulfur	>1000 ppm
Chlorine	> 600 ppm
Sodium	> 100 ppm
Fluorine	> 100 ppm

(7)* Applying a developer, an absorbent powder, to enlarge the fluorescent area,

(8) Inspection by an optical microscope with an appropriate ultraviolet light source and filtering system.

Figure 3-1 shows a schematic representation of the apparatus for the microscopic examination. The wave length of the light source used in this study was 4,000-4,5000 Å. When the dye penetrant is subjected to the electromagmetic radiation, it will emit another electromagnetic radiation of longer wave length in the visible spectrum. The wave length of the emitted radiation is λ = 6,000 Å, yellow-green in color. This technique worked very well in detecting microbranching as small as 80 microns in length.

The specimen surface was examined before and after loading with the fluorescent dye penetrant technique as described previously. The dye could penetrate into sites on a surface such as open pores, grain pull-outs, machining or lapping cracks, and grain boundary groovings. When rinsing, the excess dye could be washed out from the sites; however, the fluorescent light from the residual dye inside the damaged area was intense enough for the detection. A low magnification micrograph taken on a potential tensile surface of the specimen, shown in Fig. 3-2, exhibits many small fluorescent spots and a relatively large spot of 150

*Process (7) was omitted in the present study.

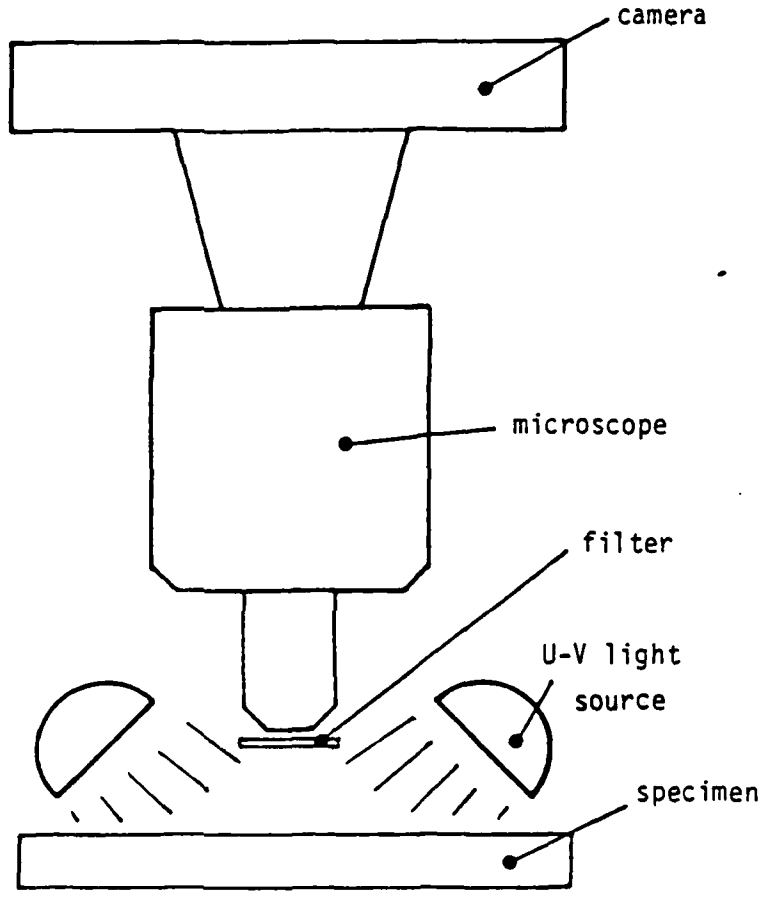

Fig. 3-1 Schematic Drawing of the Microscopic Examination Apparatus.

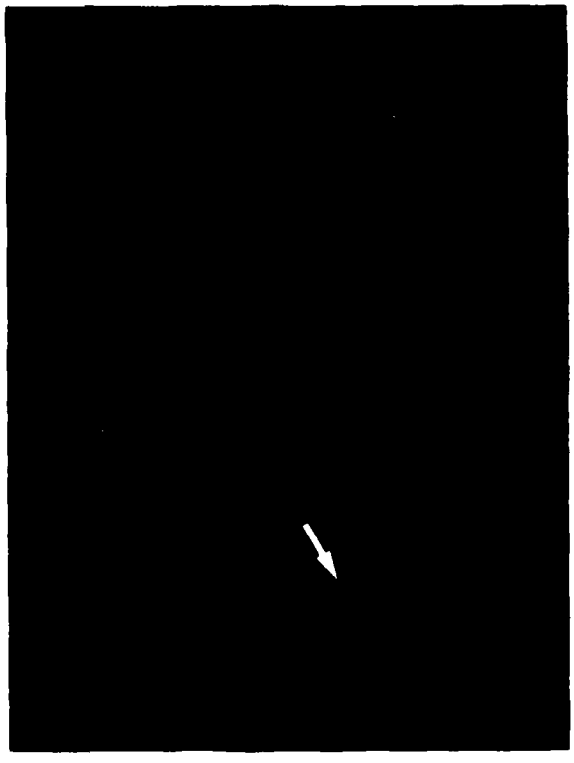

Fig. 3-2 Low Magnification Optical Micrograph with Fluorescent Dye Penetrant (12 X)

Notice that a large spot can be seen as in dicated by the arrow.

microns in diameter. The size of the small spots is generally one to a few grain size as can be seen in Fig. 3-3. Notice that intense fluorescent spots can be observed around voids or grain pull-outs, indicating existence of grain size damage such as grain boundary separation.

After the microscopic examination of the potential tensile surface, the specimen was loaded to 124 MPa in tension for several hours. Then it was unloaded and cleaned for another microscopic examination. Figure 3-4 shows a crack which dynamically propagated from the spot identified in Fig. 3-2. The crack was induced with a special loading system developed for this study, details of which will be described in Chapter IV. The micrograph was taken on the same area as shown in Fig. 3-2, and therefore, still the surface of the specimen, not the fracture surface. Although the crack propagated dynamically in the transverse direction, it did not cause catastrophic failure of the specimen due to the special loading system.

The crack shown in Fig. 3-4 was later broken into two halves to examine the nature of the large spot revealed by the dye in Fig. 3-2. The scanning electron micrograph of the fracture surface is shown in Fig. 3-5. A large unsintered void of 150 μ in diameter can be recognized with a number of small particles around it. Notice that the fracture mode is mainly transgranular, indicating fast fracture, but no obvious feature such as pore tails or cleavage steps can be seen.

Fig. 3-3 High magnification optical micrograph with fluorescent dye penetrant (500 X)

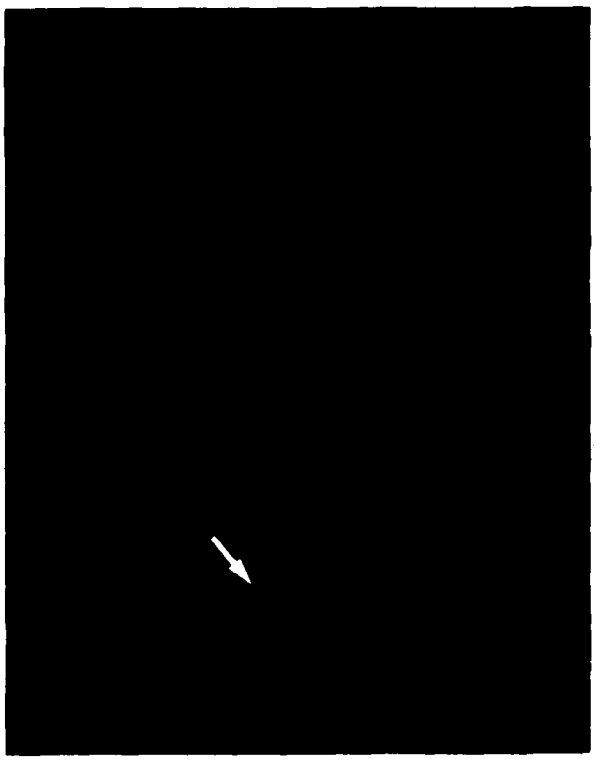

Fig. 3-4 Low Magnification Optical Micrograph with Fluorescent Dye Penetrant after Cracking (12 X)

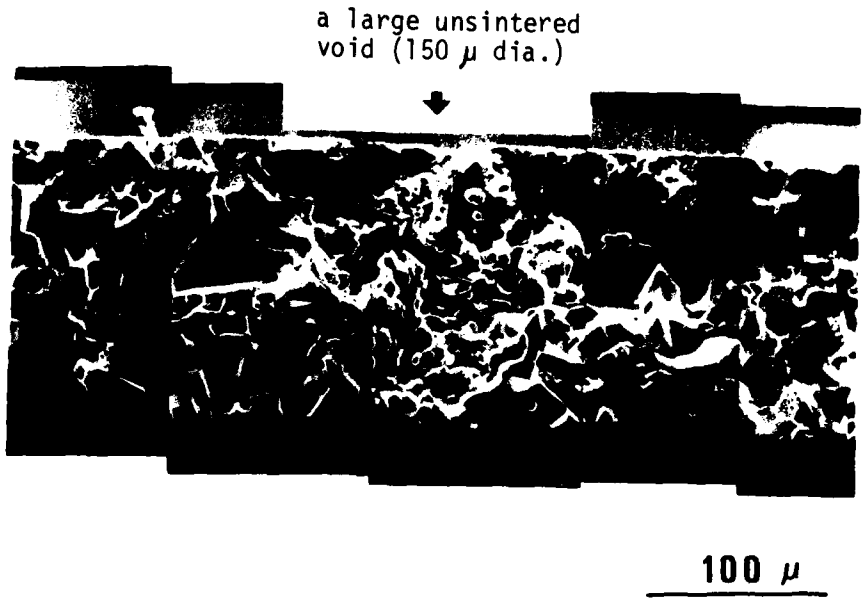

Fig. 3-5 Composite Scanning Electron Fractograph of the Crack Origin Revealed by the Fluorescent Dye Penetrant in Fig. 3-2.

2. Leitz Ultropak Illumination System

A special incident light illuminator, Ultropak, which permits observation to a greater depth in translucent material by minimizing light scattering, was used on the optical microscope, Leitz Ortholux. A typical micrograph revealing a crack by the Leitz Ultropak is shown in Fig. 3-6. This optical micrograph was taken on a portion of the crack shown in Fig. 3-4. The crack was revealed better by blocking one-half of the incident light to enhance the contrast between one side of the crack and the other. In the micrograph, the incident light on the left side was blocked.

Fig. 3-6 Optical Micrograph with Leitz Ultropak Revealing a Crack. (500 X)

3. Crack Decoration with Silver Nitrate Solution

This technique is the counterpart for the scanning electron microscopy of the fluorescent dye penetrant for the optical microscopy. The basic principle is to let the silver nitrate solution penetrate into a crack, and then by irradiating with an electron beam to excite electrons in the silver, the existence of the crack can be revealed. The procedures are as follow:[70]

(1) polishing a specimen to eliminate large machining cracks for better resolution,

(2) applying 2 mol silver nitrate solution* by immersing the specimen overnight,

(3) rinsing by running tap water to remove excess silver nitrate solution,

(4) drying by blowing air,

(5) vapor deposition of a conductive material for the scanning electron microscopy (SEM)--gold coating of approximately 200 A in thickness was used in this study,

(6) SEM examination in the primary mode instead of the secondary mode; the highly energetic electrons coming out of the silver, which is trapped in the cracked sites, can be seen as bright white lines.

*Preparation of 2 mole $AgNO_3$ solution from chemically pure crystal $AgNO_3$. Weight per mol of $AgNO_3$ is 169.87 gm/mol. For example, to make 2 mol solution in 25 cc, 0.05 mol of $AgNO_3$ is needed. Therefore, 8.49 gm of $AgNO_3$ crystal is necessary to make 2 mol solution in 25 cc of water.

A typical scanning electron micrograph revealing a crack by this technique is shown in Fig. 3-7. Portions appearing whiter than the background indicate trapped silver. The crack was induced by thermal shock, and the photograph is a small portion of the entire crack length. The white line was somewhat discontinuous; nevertheless, the crack was successfully revealed by this technique. Notice there is a secondary crack observed above the main crack plane.

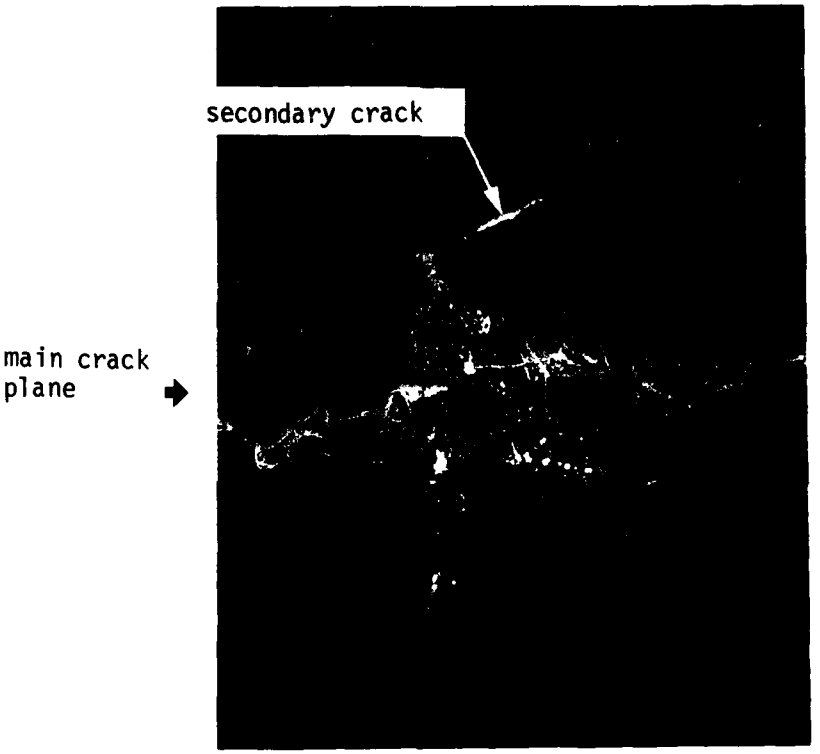

Fig. 3-7 Scanning Electron Micrograph with Silver Nitrate Solution Revealing a Crack. (700 X)

Notice that a secondary crack can be seen above the main crack plane.

4. The Problem Encountered and Its Solution

In spite of an extensive effort to locate the early stage of crack extension from inherent flaws, the fluorescent dye penetrant, Leitz Ultropak illumination, and the crack decoration by silver nitrate solution techniques did not work. Although a crack which had propagated dynamically in large scale was readily observed by the techniques, the on-set of crack growth from the inherent flaws could not be seen at all. It might be because when a crack propagates dynamically in large scale, some debris may be left in the crack to keep the crack open, whereas the crack might be very small and tightly closed in the early stage of crack extension from the inherent flaws.

It was finally found, after numerous trials, that the dye penetrant or silver nitrate solution could penetrate into a crack only when the penetrant was present at the sites while cracks were forming. The dye or the solution could penetrate into the fine cracks by capillary effect unhindered by contained air or contamination of the crack surface. Therefore, a newly designed three-point bending test fixture was made to explore the possibility of dye penetrant and silver nitrate solution technique. The tensile surface of a specimen was immersed in either the fluorescent dye penetrant or the silver nitrate solution while the load was applied. The test fixture is shown in Fig. 3-8. Notice that the penetrant or the solution is maintained in the reservoir.

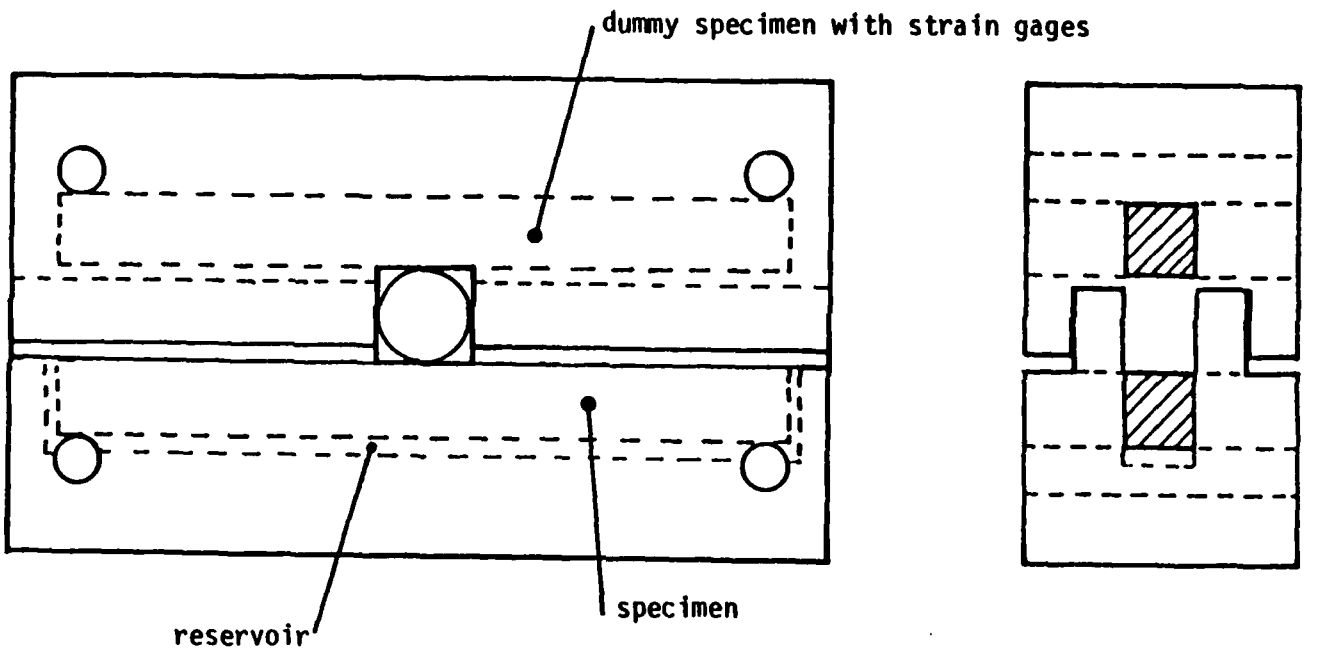

Fig. 3-8 The Three-Point Bending Apparatus Designed to Hold the Fluorescent Dye Penetrant in the Reservoir.

The preliminary delayed fracture test was conducted using the three-point bending fixture with the fluorescent dye penetrant in the reservoir. The specimen failed after 25 minutes at 131 MPa, which is 68% of the average fracture strength. The broken halves were attached together, and the tensile surface was subjected to the microscopic examination using the optical microscopy with the ultraviolet light. Figure 3-9 shows the composite optical micrograph taken on the tensile surface of the failed halves together. In addition to the main crack which caused failure of the specimen, some smaller linear arrays of fluorescent spots can be seen. A linear array might indicate a crack or a cluster of small cracks extended from the inherent flaws. Notice that there are no linear arrays of fluorescent dye spots far away from the center, where stresses were much less, indicating that the arrays of spots were not induced by machining or lapping, but by the applied tensile stress.

While the preliminary tests with the fluorescent dye penetrant were successful in locating the early stage of crack extension from the inherent flaws, the silver nitrate solution technique had an additional problem; the solution is so highly corrosive that no metallic parts could be used in the testing fixture. Therefore, only the fluorescent dye penetrant will be used to reveal the sites of crack initiation in the present study.

Figure 3-10(a) shows a higher magnification (100 X) optical micrograph of a linear array of fluorescent dye

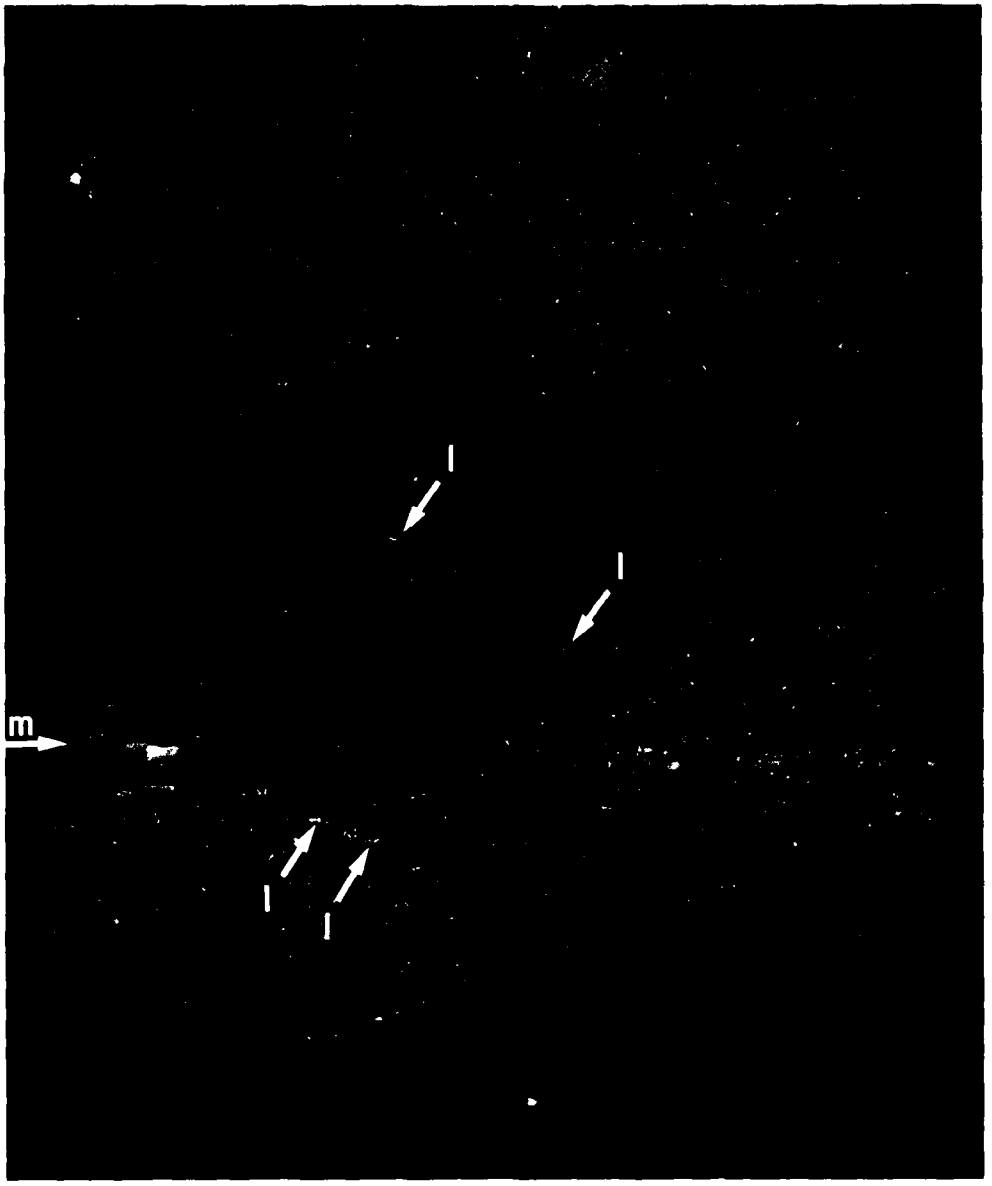

Fig. 3-9 Composite Optical Micrograph with Fluorescent Dye Penetrant after Fracture in Three-point Bending. (12 X)

Notice that in addition to the main crack(m), a few linear arrays(l) can be observed.

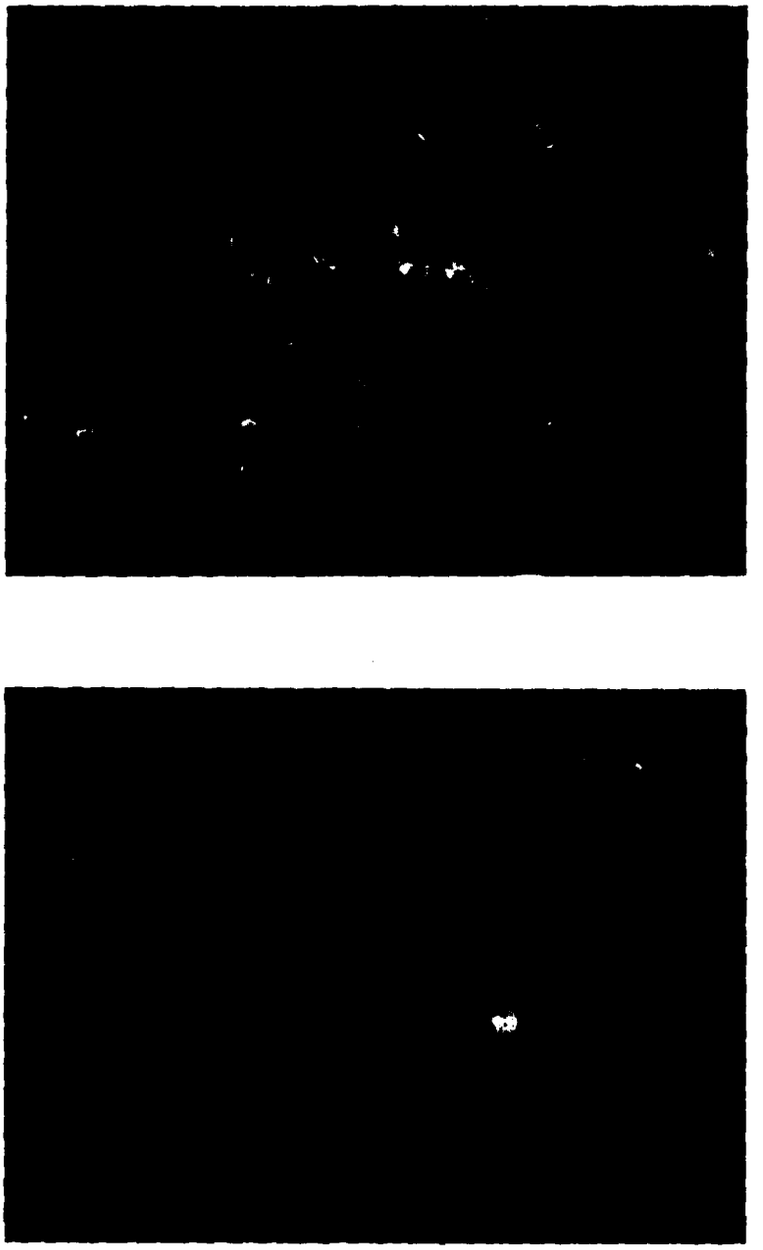

(a)

(b)

Fig. 3-10 (a) Linear Array of Fluorescent Dye Spots,

(b) The Same Dye Spots Superimposed on the Optical Micrograph.

spots obtained by the previously mentioned technique. Notice that the crack width seems to be broad in the photograph because the spots are the projected area of what is probably a very complicated three-dimensional crack or a cluster of small cracks. In order to correlate the fluorescent spots and the surface topography, the ultraviolet light and the conventional optical illumination were superimposed. Figure 3-10(b) shows the superimposed micrograph of the same area as shown in Fig. 3-10(a). The trace of the crack path can be seen relative to the surface image. Dark spots and lines in the micrograph are an indication of flaws such as grain pull-outs, pores, or machining cracks. Notice that the fluorescent spots are located next to or between the dark spots. Further examination of the microscopic features and crack origins and crack paths was carried out by comparing the optical micrographs and the scanning electron micrographs. Figure 3-11(a) shows another linear array of dye spots. The spots were superimposed on the optical micrograph to obtain the trace of the crack path. Figure 3-11(b) shows the optical micrograph at a higher magnification; the shaded areas represent where the fluorescent spots appeared. Again notice that the spots exist next to or between the inherent flaws. Figure 3-11(c) shows the scanning electron micrograph of the same area. The surface topography is clearly shown; however, no crack can be seen at this magnification (500 X) even though the

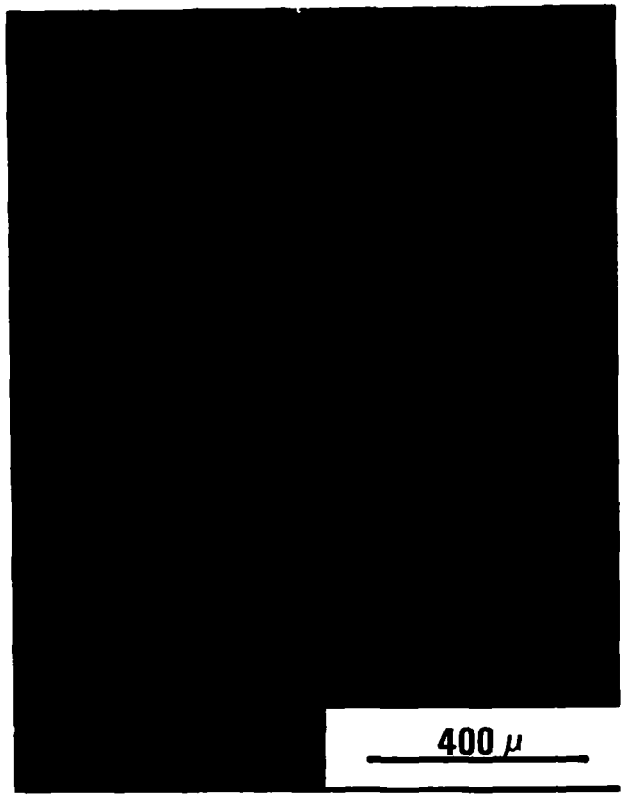

Fig. 3-11(a) A Linear Array of Fluorescent Spots.

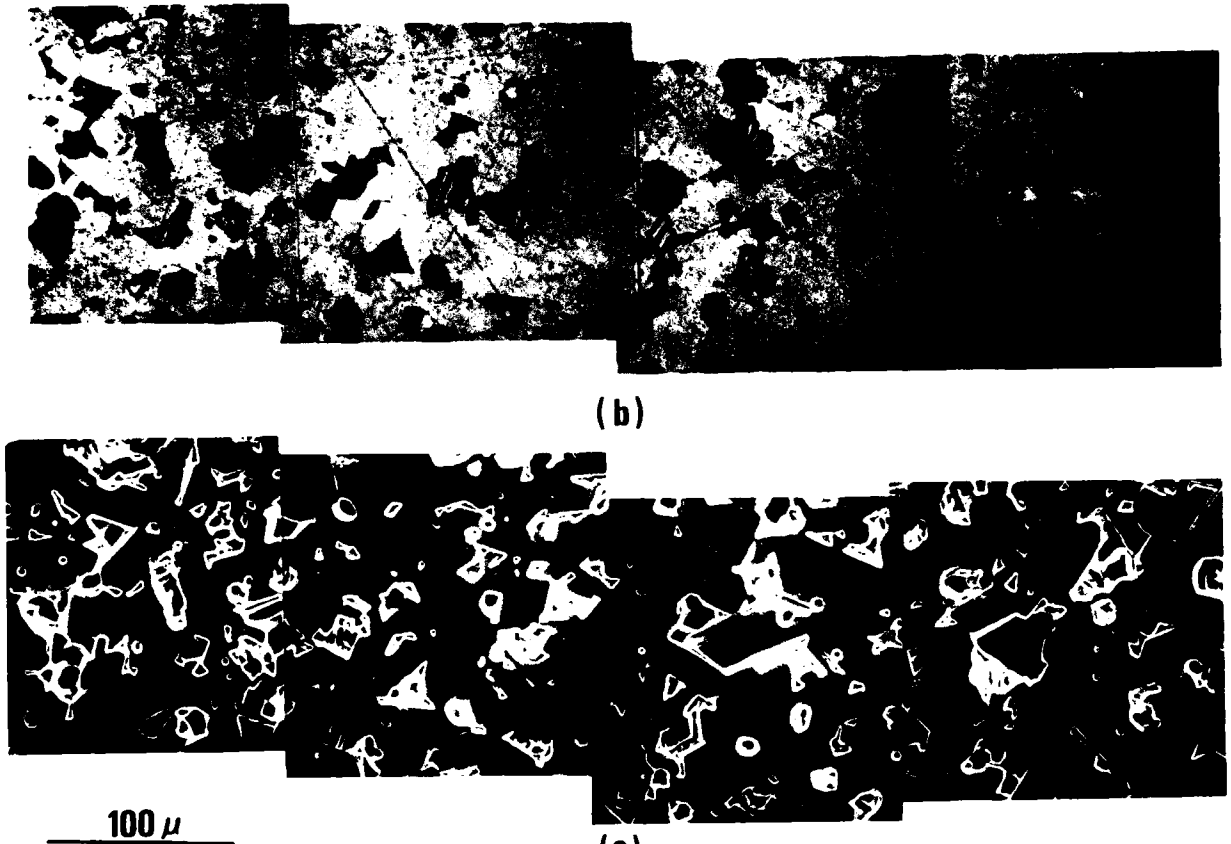

Fig. 3-11 (b) Optical Micrograph of Fig. 3-11(a) at Higher Magnification (Fluorescent Dye Spots are Indicated as Shaded Areas) (c) Scanning Electron Micrograph of the Same Area as Fig. 3-11(b).

existence of the crack had been confirmed by the fluorescent dye penetrant experiment. This is in agreement with the unsuccessful attempts to observe slow crack growth from inherent flaws using scanning electron microscopy and optical microscopy with special techniques.

Figure 3-12 shows a small portion of Fig. 3-11(c) at much higher magnification. Some inherent flaws are seen to be connected by fine intergranular cracks as indicated by arrows, but the cracks could only be observed along a small portion of the entire crack length as revealed by the dye.

Inability of the scanning electron microscopy to clearly reveal this kind of cracks was true for all the cracks observed in the present study. Observation of only a small portion of a crack, even when its location is exactly known, confirms superiority of revealing small cracks by the fluorescent dye penetrant technique.

Although the adverse environment of the fluorescent dye might affect the crack velocity, study of slow crack growth initiated at inherent surface flaws by this method is meaningful. The objectives of the present study are to identify the flaws responsible for the initiation and to study micromechanisms of slow crack growth in delayed fracture, not to study the effect of a specific environment on the rate of crack growth.

Now that a microscopic examination has been successfully developed to reveal locations of the early stage of

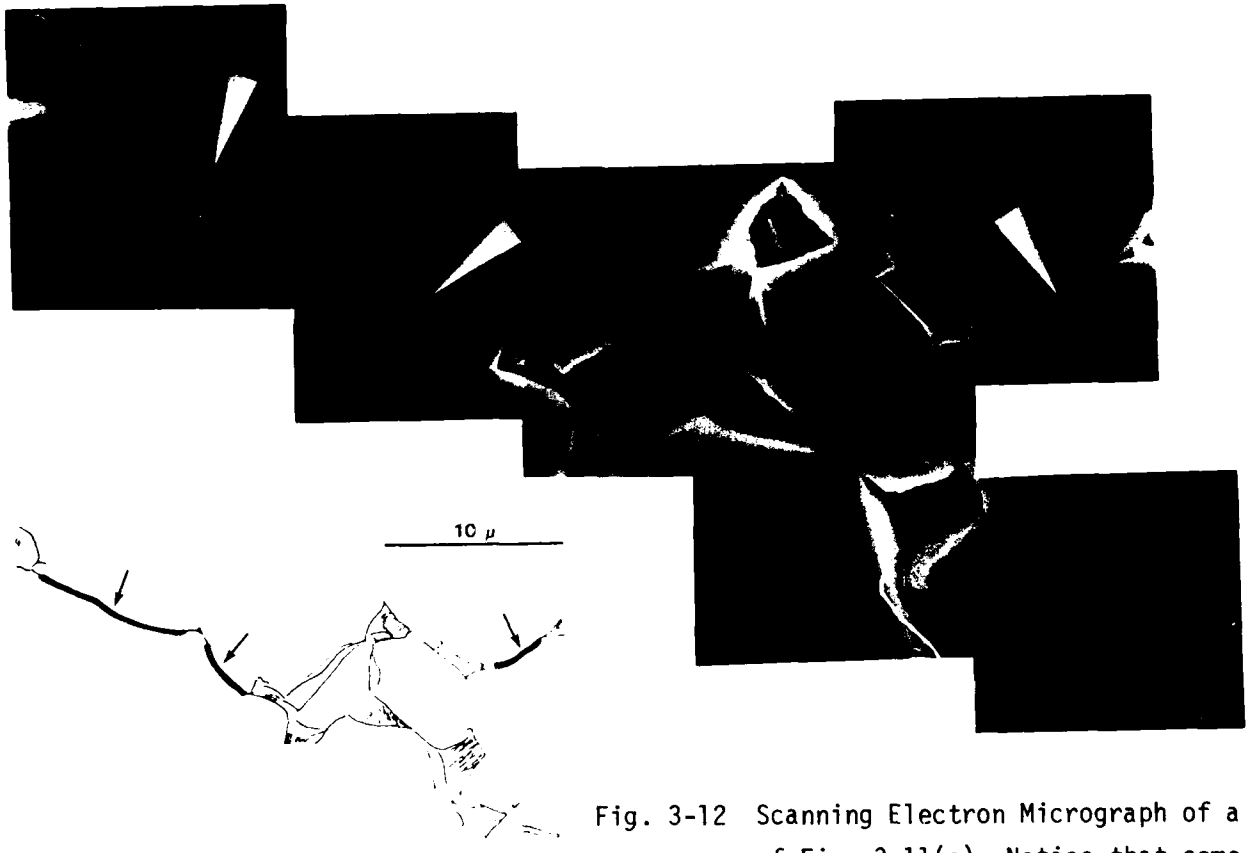

Fig. 3-12 Scanning Electron Micrograph of a Portion of Fig. 3-11(c). Notice that some inherent flaws are seen to be connected by fine intergranular cracks indicated by arrows.

crack extension from the inherent flaws, which permits identification of flaws and leads to determination of the micromechanisms of slow crack growth. The next objective is to develop a mechanical testing system to create a number of cracks on a surface of a specimen without causing catastrophic failure.

CHAPTER IV

MECHANICAL TESTING AND MATERIAL

The objectives of the present study are to identify flaws responsible for the crack initiation and to study the micromechanisms of slow crack growth in the delayed fracture of alumina. Two major hurdles to overcome were foreseen in order to achieve the objectives: (1) a fine-crack detection technique to reveal location of the early stage of crack extension from inherent flaws and (2) a mechanical testing technique to create many crack initiations on a surface of a specimen for economic reasons. The first has been discussed in Chapter III in detail.

In studying delayed fracture, three- or four-point bending tests have been used widely. However, if there was a large void, inclusion, or any other flaw present on a surface of a specimen, then once the crack started to grow, it would cause catastrophic failure of the specimen in these bending tests. It is economically undesirable to study one worst flaw per specimen. Therefore, a new testing system was needed which had a capability of creating a number of crack initiations from inherent flaws without causing catastrophic failure of the specimen. For this, the eccentrically loaded column testing apparatus was developed.

In this chapter, the material used in the present study will be explained briefly and a detailed description of the eccentrically loaded column testing apparatus will be presented.

1. Specimen

1.1 Material

The ceramic material used in the present study is sintered alumina, WESGO Aℓ-300.* Chemical composition and physical properties are given in Table 4-1 and Table 4-2 respectively. The material was chosen because of the following reasons:

(1) it is optically opaque to some depth, ∿100 μ, which makes optical inspection by both Zeiss microscope with the fluorescent dye penetrant and Leitz microscope with Ultropak possible,

(2) mechanical and physical properties are available on the material.

1.2 Specimen Dimensions and Surface Finish

The billet was cut into 50 by 50 by 100 mm blocks by Ceradyne.** The ends of those blocks were then lapped within five wavelengths by WESGO and then returned to Ceradyne for the final slicing into 10 by 10 by 100 mm specimens. Thirty-two specimens of Aℓ-300 were prepared.

For ease of crack detection, ten Aℓ-300 were sent back to WESGO for an additional lapping. One surface and two edges were lapped to eliminate machined cracks and edge effects. The specimen is shown in Fig. 4-1.

---

*Western Gold and Platinum Co., Belmont, California 94004.
**Ceradyne, Santa Ana, California 92705.

Table 4-1. Chemical Composition of Al-300 (wt %)

Si	Mg	Ca	Na	Cr	Fe	Ga	Ti
1.25	0.02	0.60	0.02	0.001	0.07	0.015	0.025

Table 4-2. Physical Properties of Al-300

Average Strength	191.7 MPa (27,800 psi)*
Young's Modulus	327.5 GPa (47,500 ksi)
Average Grain Size	32 microns

* Stress Rate, 20 MPa/sec.

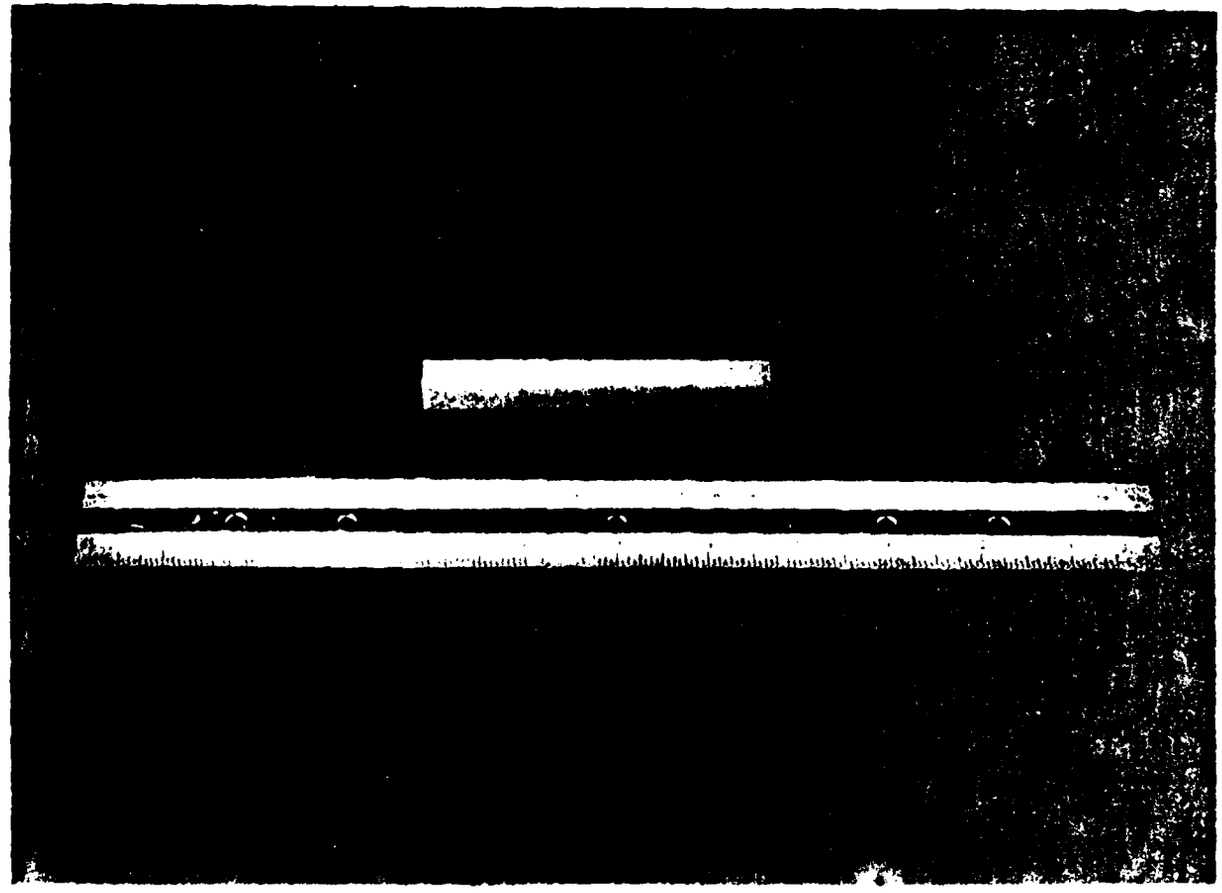

Fig. 4-1 Specimen (Al-300)

2. Eccentrically Loaded Column Testing Apparatus

2.1 Basic Principle

The basic concept is to arrest cracks, which have emanated from inherent flaws before they propagate to cause catastrophic failure of the specimen. This can be achieved by superimposing a compressive axial load P and a bending moment M_{xy} as shown in Fig. 4-2. The axial load P is applied in x-direction, and the bending moment M_{xy} is applied so that tensile stresses are induced on a surface and large compressive stresses are induced on the opposite surface of the specimen. The superimposed loading condition can be obtained by the eccentrically loaded column testing apparatus. When a crack starts to propagate on the tensile surface, it grows slowly until the crack size becomes critical. The shape of the crack may be a portion of an ellipse due to a nonuniform stress field as shown in Fig. 4-3, which makes detection from the surface easier. When it reaches the critical value, the crack will propagate dynamically in the z-direction but not in the y-direction (depth-wise). Therefore, the cracking does not cause catastrophic failure of the specimen. A crack which propagated dynamically in the z-direction to form the final shape indicated by the shaded area in Fig. 4-4 will be called an all-the-way-across crack hereafter in the dissertation. An all-the-way-across crack depth was revealed by the fluorescent dye penetrant as shown in Fig. 4-5. In

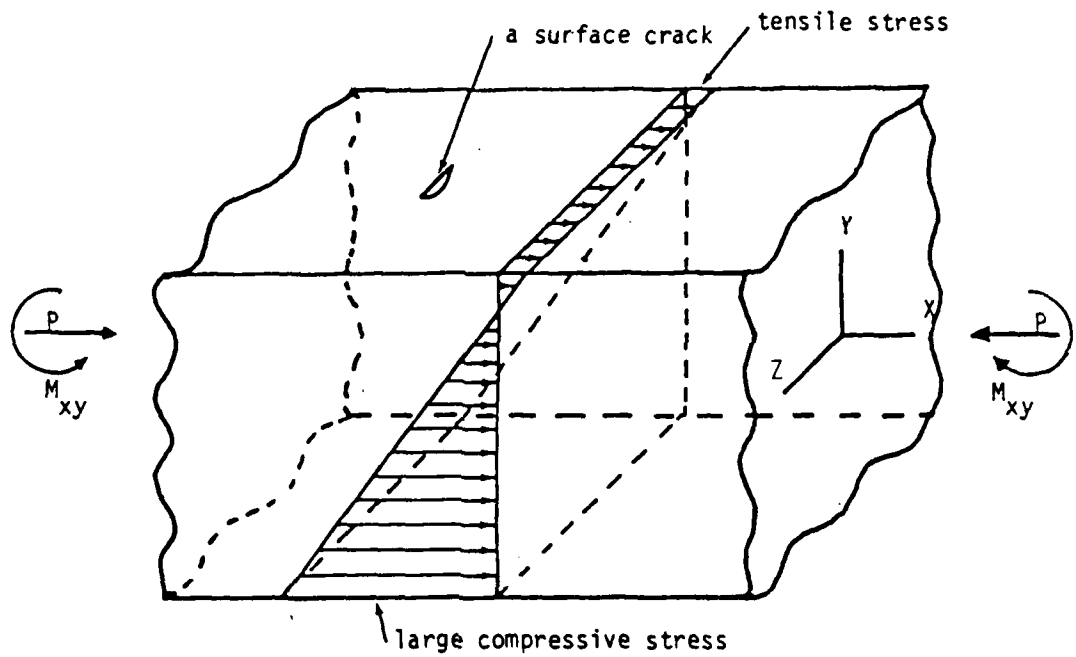

Fig. 4-2 Idealized State of Stress Induced by Superimposed Compression and Bending.

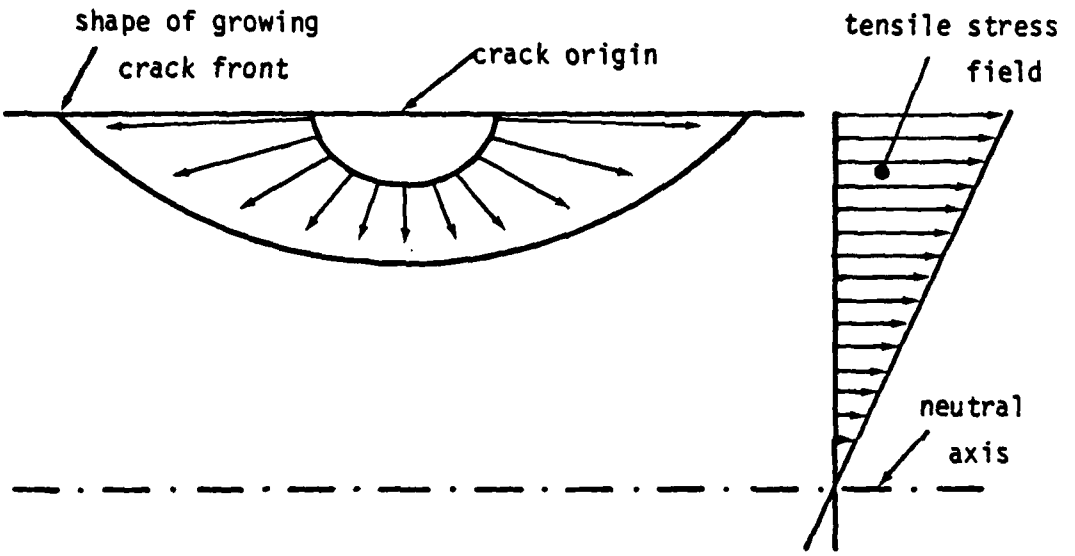

Fig. 4-3 Shape of a Growing Crack; not semicircular due to the steep stress gradient.

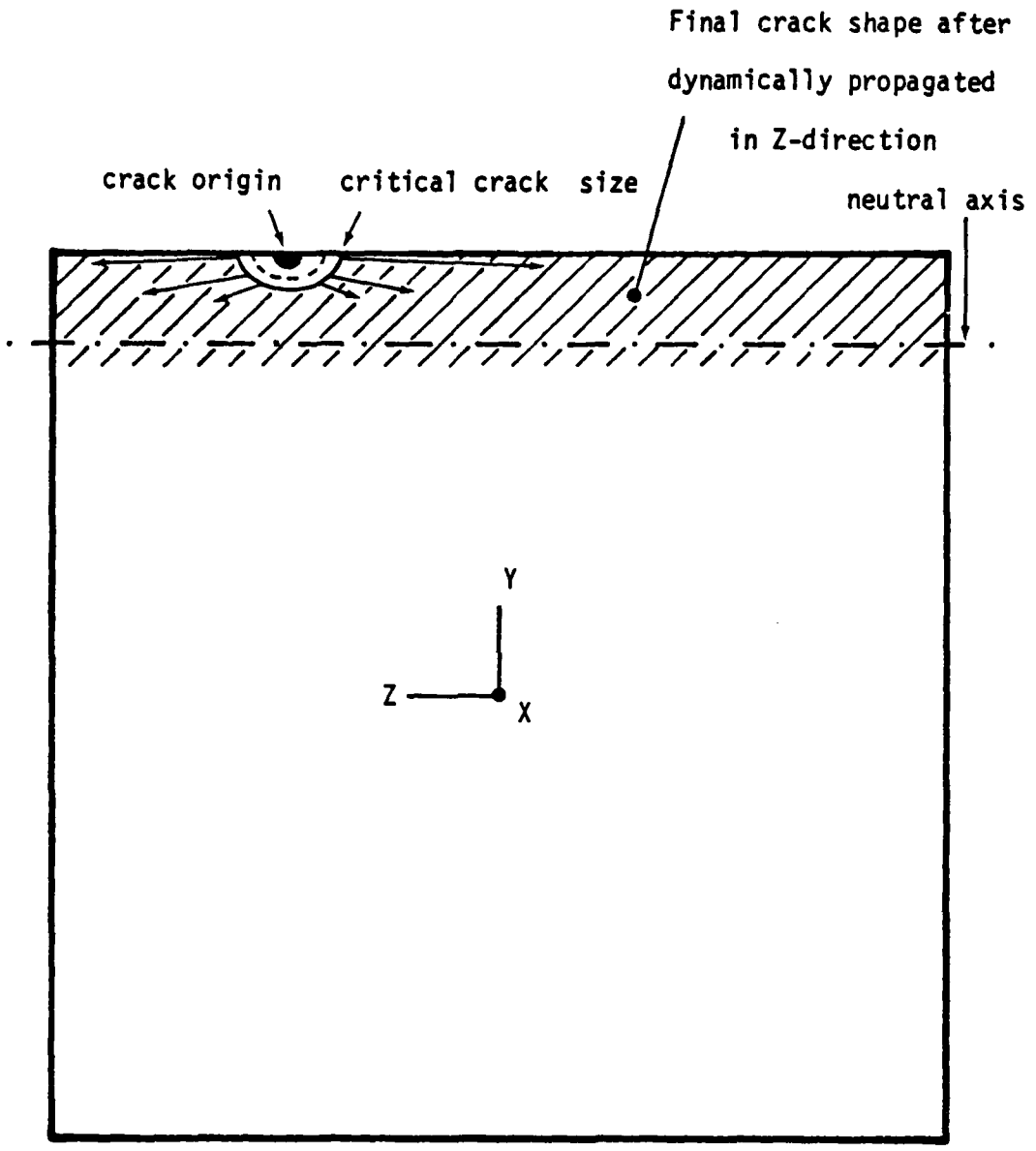

Fig. 4-4 Cross Section of a Specimen and Crack Propagation Behavior.

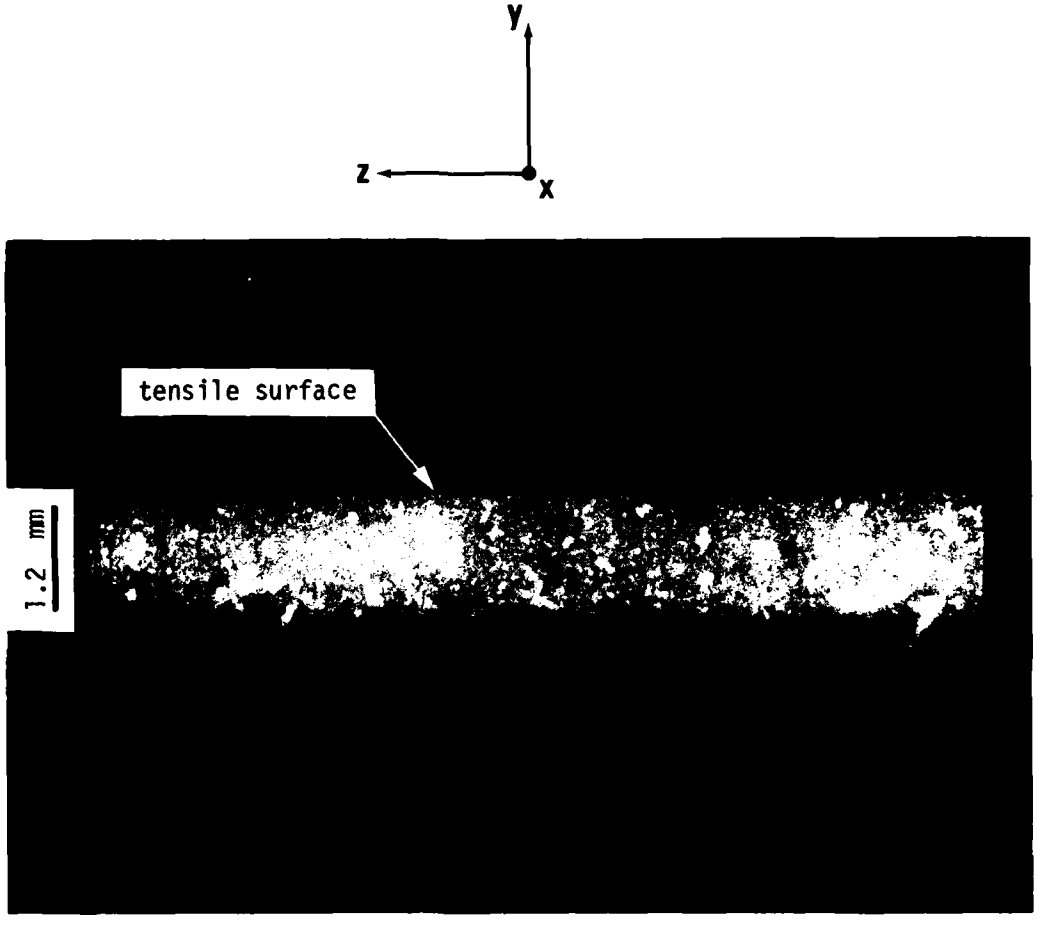

Fig. 4-5 Penetration Depth of the Fluorescent Dye When a Crack Runs All-the-Way-Across the Specimen in the Z Direction. (12 X)

Fig. 4-5, the optical fractograph was taken after the all-the-way-across crack was formed, the fluorescent dye was applied, and the crack was opened by fracture. Notice that the crack was arrested in the y-direction due to the compressive stresses; the crack depth is about 1.2 mm and the neutral axis of the specimen is 1.0 mm from the tensile surface in this case.

2.2 Apparatus

The eccentrically loaded column testing apparatus was developed to induce tensile stresses on a surface and large compressive stresses on the opposite surface of a specimen. The apparatus was designed to maintain the stress for a long period of time with good reproducibility. It consists of loading blocks made out of hardened 4340 steel and an alignment jig made out of aluminum as shown in Fig. 4-6. The hardened steel components of the loading blocks, starting from each end of the specimen, consist of a truncated pyramid, a cylindrical roller, a V-grooved block, a second cylindrical roller transverse to the first, and a second V-grooved block. All the components fit into the alignment jig, and the eccentricity is machined into the alignment jig as shown in Fig. 4-7. This eccentricity induces a bending moment on a surface of the specimen, combined with the large axial compression, producing tensile stresses on a surface while inducing much higher compressive stresses on the opposite surface of the specimen. The ratio between the tensile and compressive stress is controlled by the amount of eccentricity built into the alignment jig; thus, the ratio can be accurately controlled.

Difficulties arise when a ceramic material is subjected to high compressive stresses through a metallic component; the ceramic tends to crack due to the difference in Poisson's ratio as illustrated in Fig. 4-8. This is often called

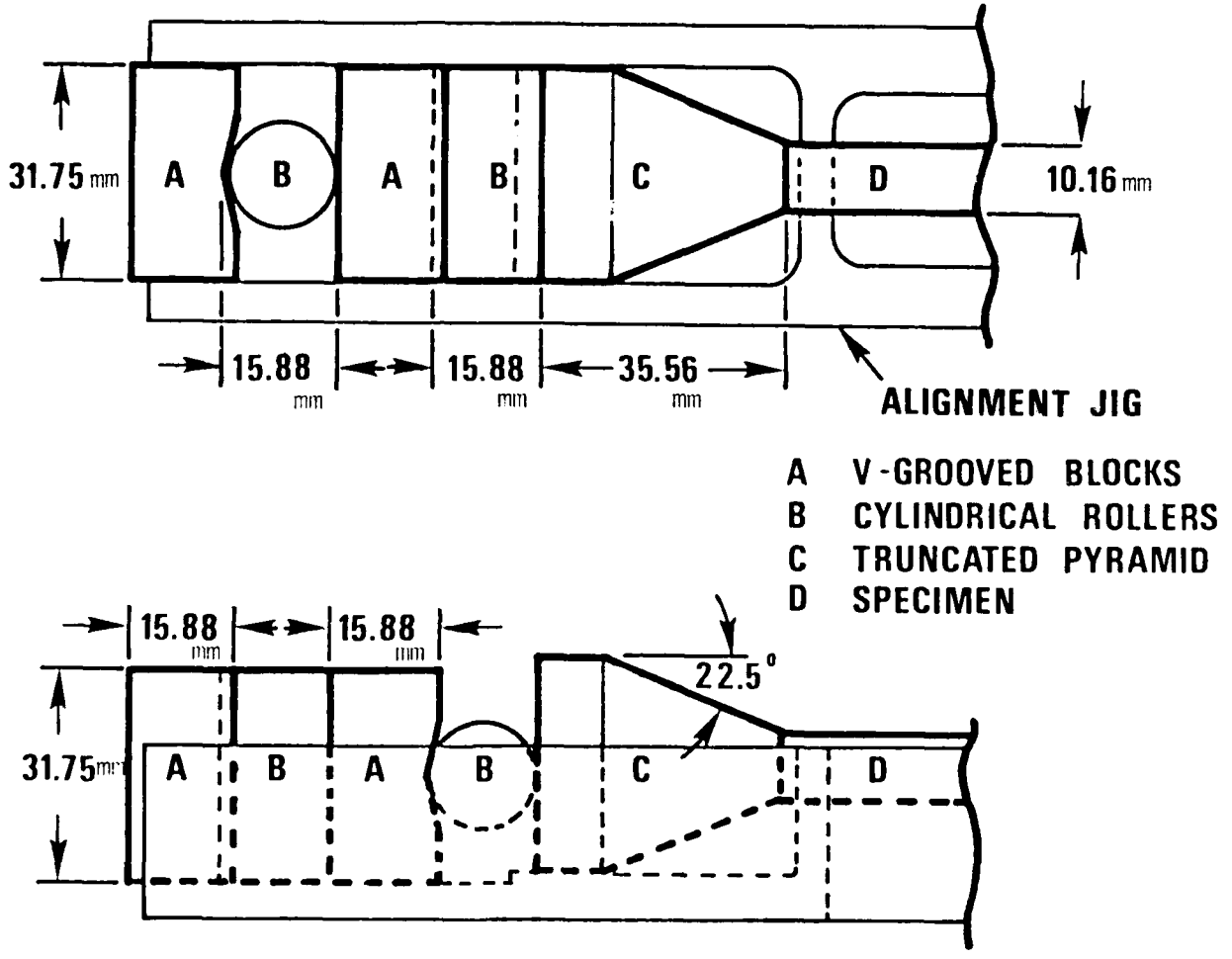

Fig. 4-6 Loading Blocks and Alignment Jig.

AD-A113 012 CALIFORNIA UNIV LOS ANGELES DEPT OF MATERIALS SCIEN--ETC F/G 11/6
IDENTIFICATION OF FLAWS RESPONSIBLE FOR CRACK INITIATION AND MI--ETC(U)
FEB 82 G SINES, T OKADA AFOSR-77-3425

UNCLASSIFIED AFOSR-TR-82-0225 NL

2 3

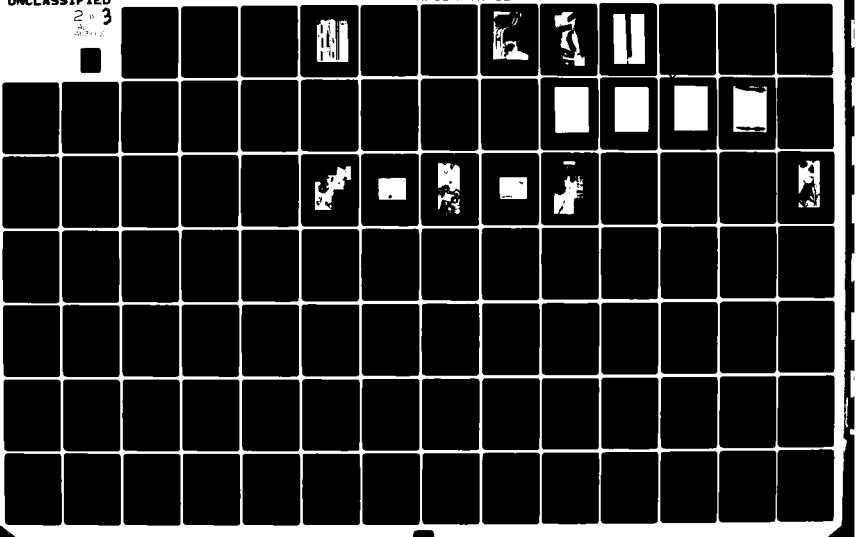

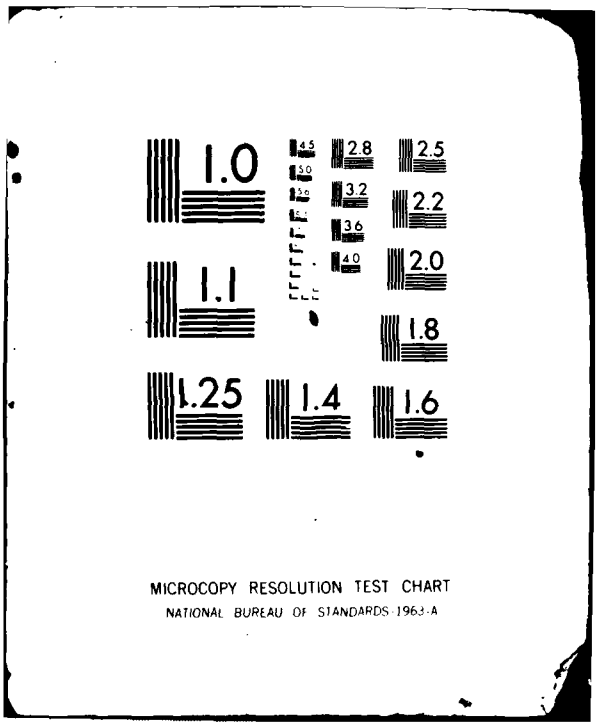
1.0
1.1
1.25
1.4
1.6
1.8
2.0
2.2
2.5
2.8
3.2
3.6
4.0
4.5
5.0
5.6
MICROCOPY RESOLUTION TEST CHART
NATIONAL BUREAU OF STANDARDS 1963-A

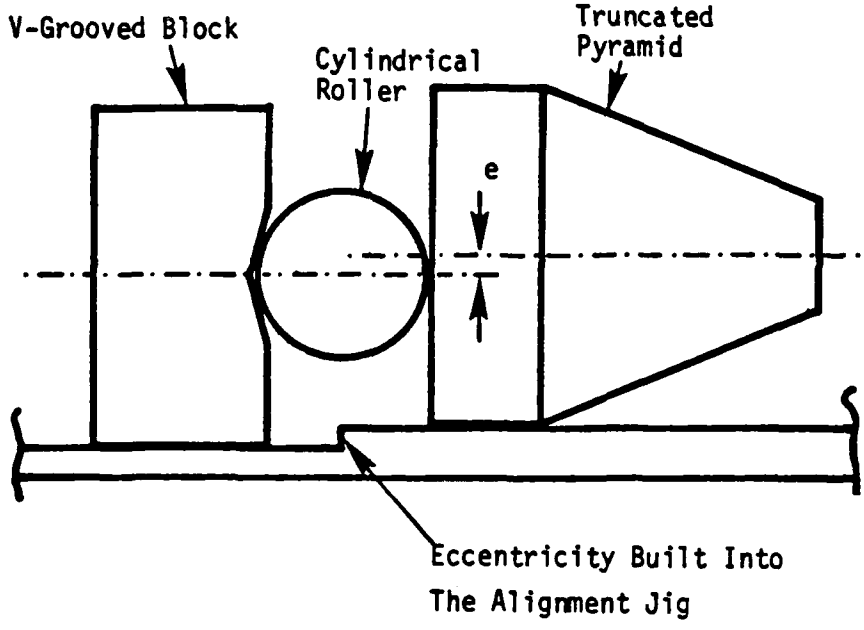

Fig. 4-7 Built-in Eccentricity in the Alignment Jig.

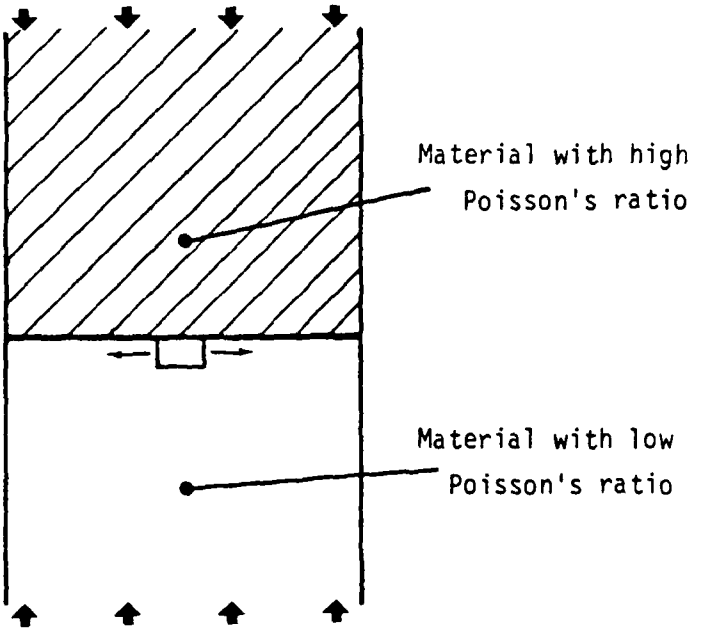

Fig. 4-8 Induced Tensile Stress Due to Difference in Poisson's Ratio.

"end-splitting". In order to avoid the failure, closer matching of the transverse compliance was needed; this was achieved by using the truncated pyramids to reduce the stress in the steel components next to the ceramic specimen. Also paper was placed between the steel and the ceramic to reduce friction. Detail of the difficulties and solutions in testing of ceramics in compression has been discussed by Sines and Adams.[71]

It might be thought that other compressive loading devices could serve the same purpose. For example, a spherical joint instead of the double cross cylinders has been successfully used in some cases; however, friction between the mating surfaces makes the joint ineffective upon application of very high loads. Another apparatus to be considered are a pressurized fluid layer between the mating surfaces[72] and an air bearing[73] as load bearing, friction-less components. These apparatuses are very complicated and expensive so that they are inappropriate for the present study.

The eccentrically loaded column testing apparatus is self-contained, and it provides a very accurate load path on a specimen by any loading frame which may not have an accurately controlled load path. All the components and the alignment jig and the specimen are fitted together in the photograph shown in Fig. 4-9. The alignment jig was left intact with the loading blocks all the time to provide

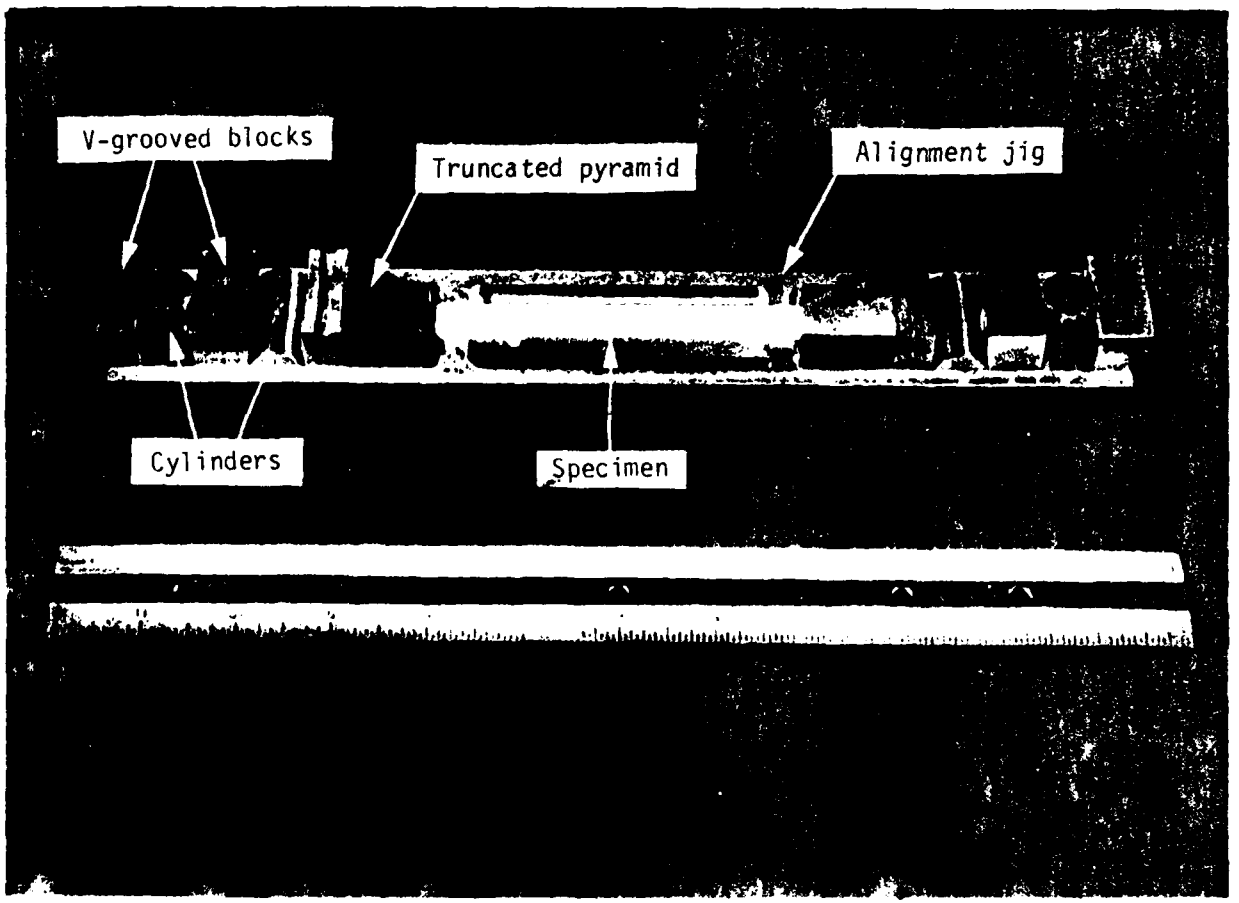

Fig. 4-9 Photograph Showing the Loading Blocks and Specimen Fit into the Alignment Jig.

the accurate load path and to keep the blocks from flying away in case of premature failure.

2.3 Loading Frame

An essential problem that had to be solved was how to maintain a high constant load on the apparatus over periods of a few days. The 100,000 lb Riehle mechanical beam machine was ideal for this application because of its simplicity and stability. The beam machine was modified to give even more reliability and accuracy of the constant load by a secondary motor as shown in Fig. 4-10. The secondary motor drives the loading cross head at about 0.008 of the speed of the regular drive. If the load falls off, the microswitch senses the drop of the beam and activates the secondary motor until the correct load is obtained.

By some minor modifications, such as shape of the alignment jig and shape and depth of the V-grooves in the loading blocks, the results of the test improved from premature failure of the specimen shown in Fig. 4-11 to very stable multiple crack formation without catastrophic failure of the specimen as shown in Fig. 4-12.

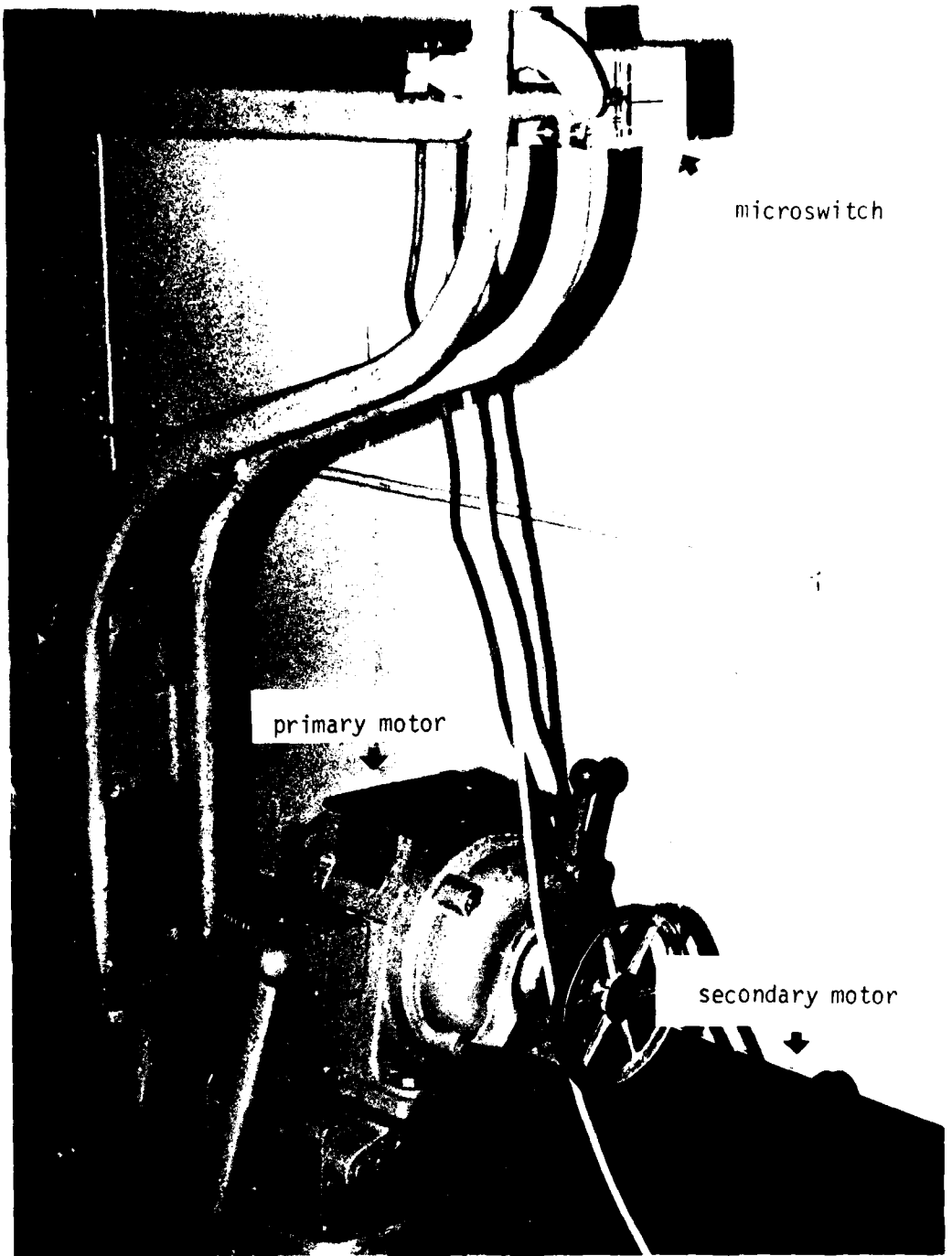

Fig. 4-10 The Secondary Motor and The Microswitch Attached to The Beam Machine.

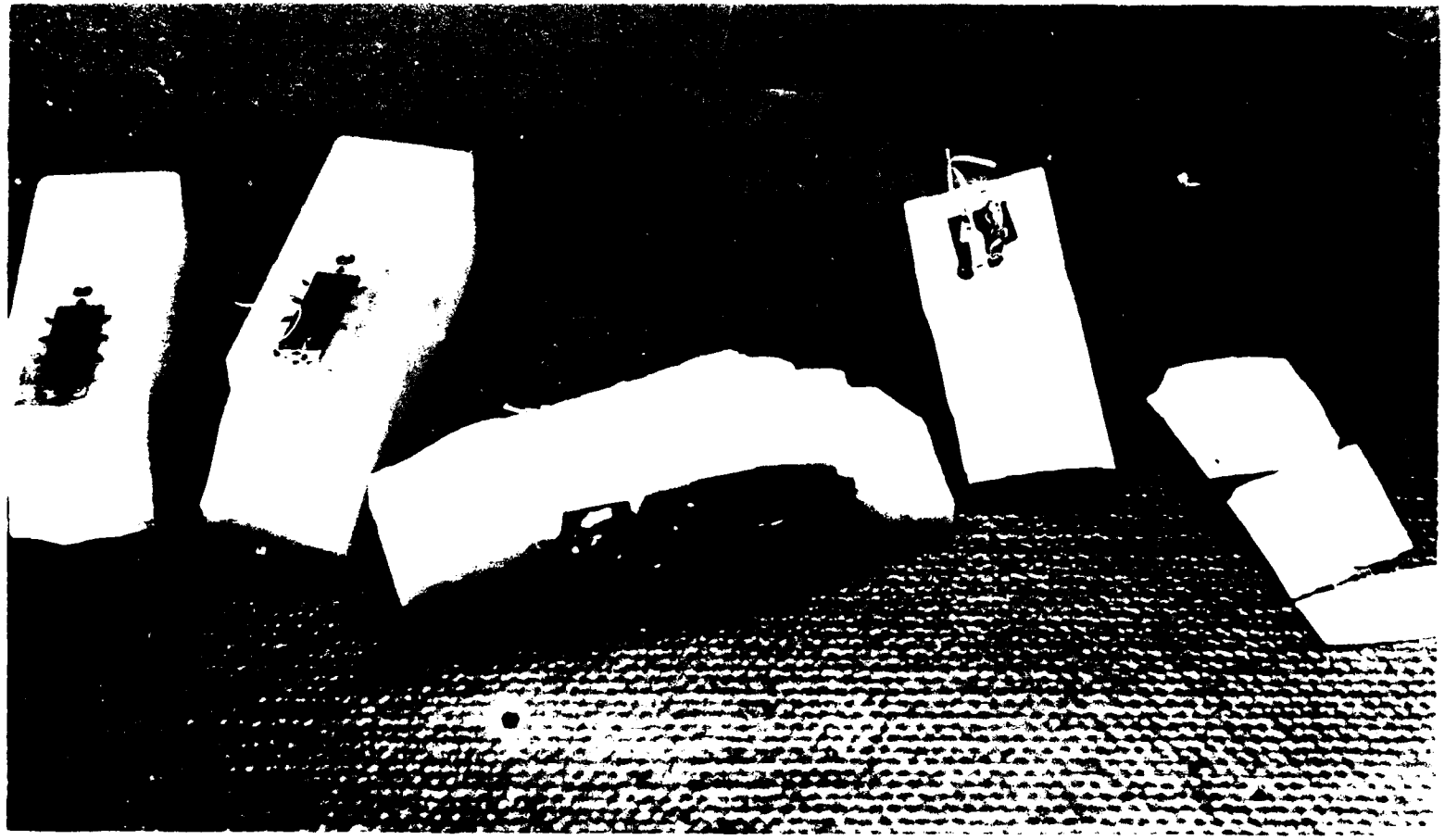

Fig. 4-11 Premature Failure Due to Shifts in Loading Path.

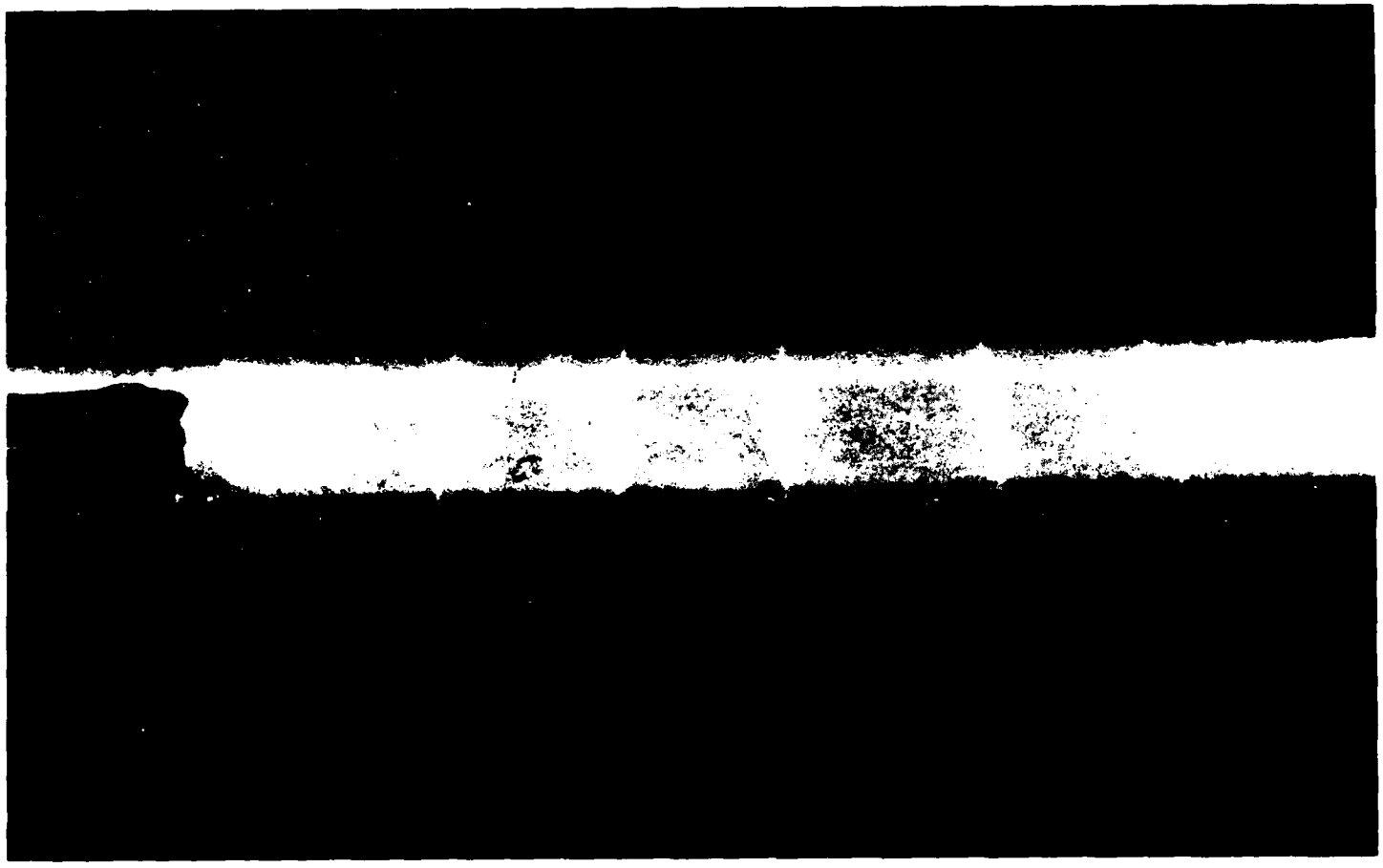

Fig. 4-12 Stable Multiple Cracks Obtained From The Improved Testing Apparatus.

2.4 Analysis of the Eccentrically Loaded Column

When a column is subjected to an eccentric compressive load as shown in Fig. 4-13, the displacements in y-direction along x-axis can be obtained in the following manner:

The differential equation for the problem is

$$v^{IV}_{(x)} + k^2 v''_{(x)} = 0 \qquad (4\text{-}1)$$

The general solution to eq. (4-1) can be given by

$$v_{(x)} = C_1 + C_2 x + C_3 \sin(kx) + C_4 \cos(kx) \qquad (4\text{-}2)$$

where $k^2 = P/EI$

The boundary conditions are

$$\begin{aligned} v_{(\ell)} &= 0 \\ v'_{(0)} &= 0 \\ M_{(\ell)} &= Pe \\ V_{(\ell)} &= 0 \end{aligned} \qquad (4\text{-}3)$$

eq. (4-3) gives

$$\begin{cases} v_{(\ell)} = C_1 + C_2\ell + C_3 \sin k\ell + C_4 \cos k\ell = 0 & (4\text{-}4a) \\ v'_{(0)} = C_2 + C_3 k = 0 & (4\text{-}4b) \\ M_{(\ell)} = EIv''_{(x)} = EI(-C_3 k^2 \sin k\ell - C_4 k^2 \cos k\ell) = Pe & (4\text{-}4c) \\ V_{(\ell)} = 0 & (4\text{-}4d) \end{cases}$$

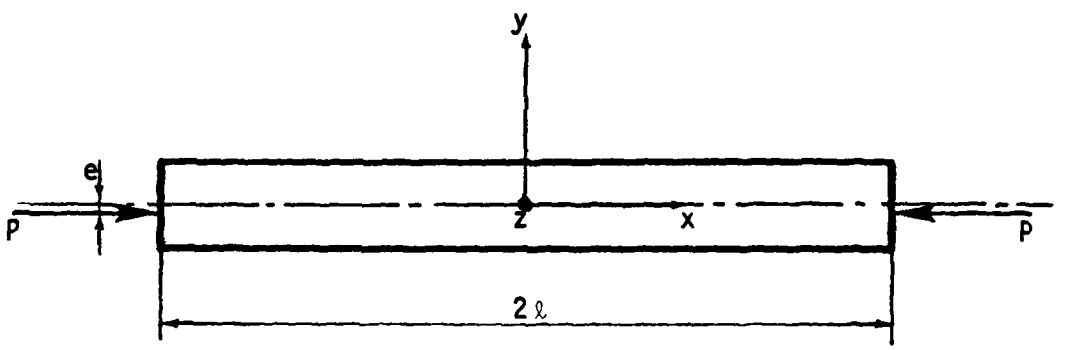

Fig. 4-13 A Column Subjected to an Eccentric Compressive Load.

From eq. (4-4d)

$$V = -Pv' - M' = -Pv' - EIv''' = 0$$

$$V_{(\ell)} = P(C_2 + C_3 k\cos k\ell - C_4 k\sin k\ell) - EI(-C_3 k^3 \cos k\ell + C_4 k^3 \sin k\ell)$$

$$= -PC_2 - k(P - EIk^2)(C_3 \cos k\ell - C_4 \sin k\ell) = 0$$

By definition,

$$p = EIk^2,$$

Therefore,

$$C_2 = 0$$

From eq. (4-4b)

$$C_3 = 0$$

From eq. (4-4c)

$$C_4 = -\frac{Pe}{EIk^2 \cos k\ell} = -\frac{e}{\cos k\ell}$$

From eq. (4-4a)

$$C_1 = e$$

Thus,

$$v_{(x)} = e\left(1 - \frac{\cos kx}{\cos k\ell}\right) \qquad (4\text{-}5)$$

at $x = 0$

$$v_{(0)} = e\left(1 - \frac{1}{\cos k\ell}\right) = e\left[1 - \frac{1}{\cos\left(\frac{P}{EI}\right)^{1/2}\ell}\right]$$

Once the displacements in y-direction are obtained, the axial strain in x-direction is expressed as follows:

$$\varepsilon_{xx} = -\frac{P}{AE} + v''_{(x)}y$$

Then,

$$\varepsilon_{xx} = -\frac{P}{AE} + \frac{e}{\cos k\ell}k^2(\cos kx)y$$

$$= -\frac{P}{AE} + \frac{e\frac{P}{EI}y}{\cos(\frac{P}{EI})^{1/2}\ell}[\cos(\frac{P}{EI})^{1/2}x] \qquad (4\text{-}6)$$

Equation (4-6) gives the axial strain on the surface of the specimen. As we can see from eq. (4-6), when the bending contribution from the transverse displacement is sufficiently large, tensile stresses can be induced on one side and large compressive stresses on the opposite surface of the specimen.

2.5 Amount of Eccentricity and the Load Path Accuracy

In order to ensure the load path accuracy and high reproducibility of the newly developed testing system, considerable strain gage measurements were taken. Nine strain gages were installed on surfaces of a specimen as shown in Fig. 4-14 to see if the calculated stress distribution was obtained, if the desired tension-to-compression ratio was obtained, and if the stresses were constant across the specimen.

Numerous data were obtained and are summarized in Fig. 4-15 and Table 4-3. Figure 4-15 illustrates the stress distribution on the tensile surface of the specimen with three alignment jigs with different eccentricities. Notice that the distance of 50.8 mm from the end of the specimen is that center of the column. Also notice that the larger the eccentricity, the more uniform the stress distribution on a tensile surface. Table 4-3 shows side-by-side accuracy as well as the tensile-to-compressive stress ratio for a given load. By selecting an appropriate amount of eccentricity, the ratio between the tension and compression can be controlled. Consequently comparison in slow crack growth behavior between tension and compression may be made. As shown in Table 4-3, 0.53, 0.76, and 1.02 mm of eccentricities resulted in 14.1 to 1, 11.9 to 1, and 10.1 to 1 ratios between the maximum compressive and tensile stresses at 64% of the tensile strength of A?-300. For example, the

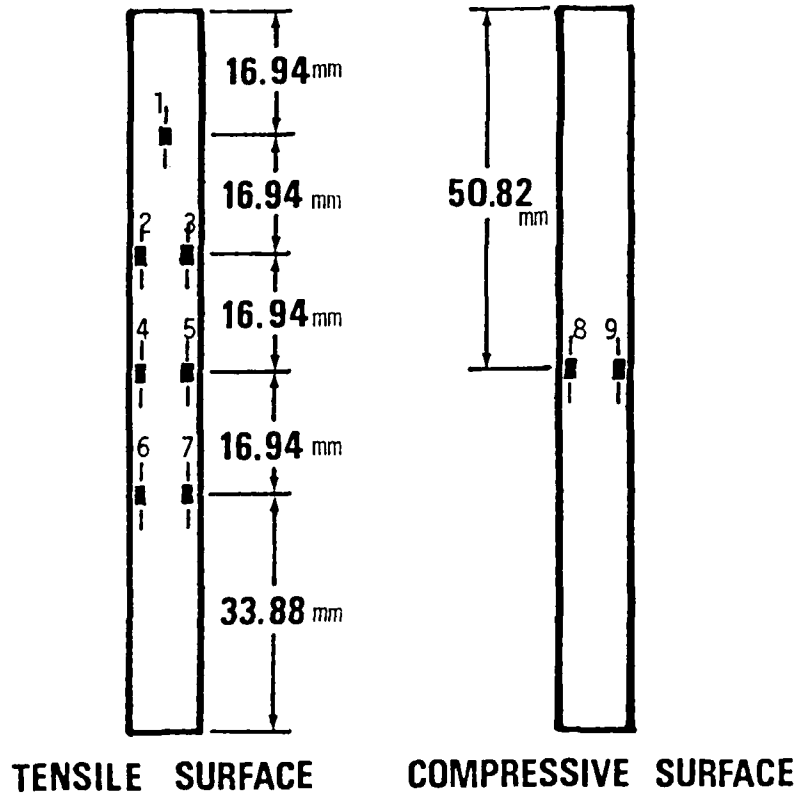

Fig. 4-14 Specimen with Nine Strain Gages for Calibration.

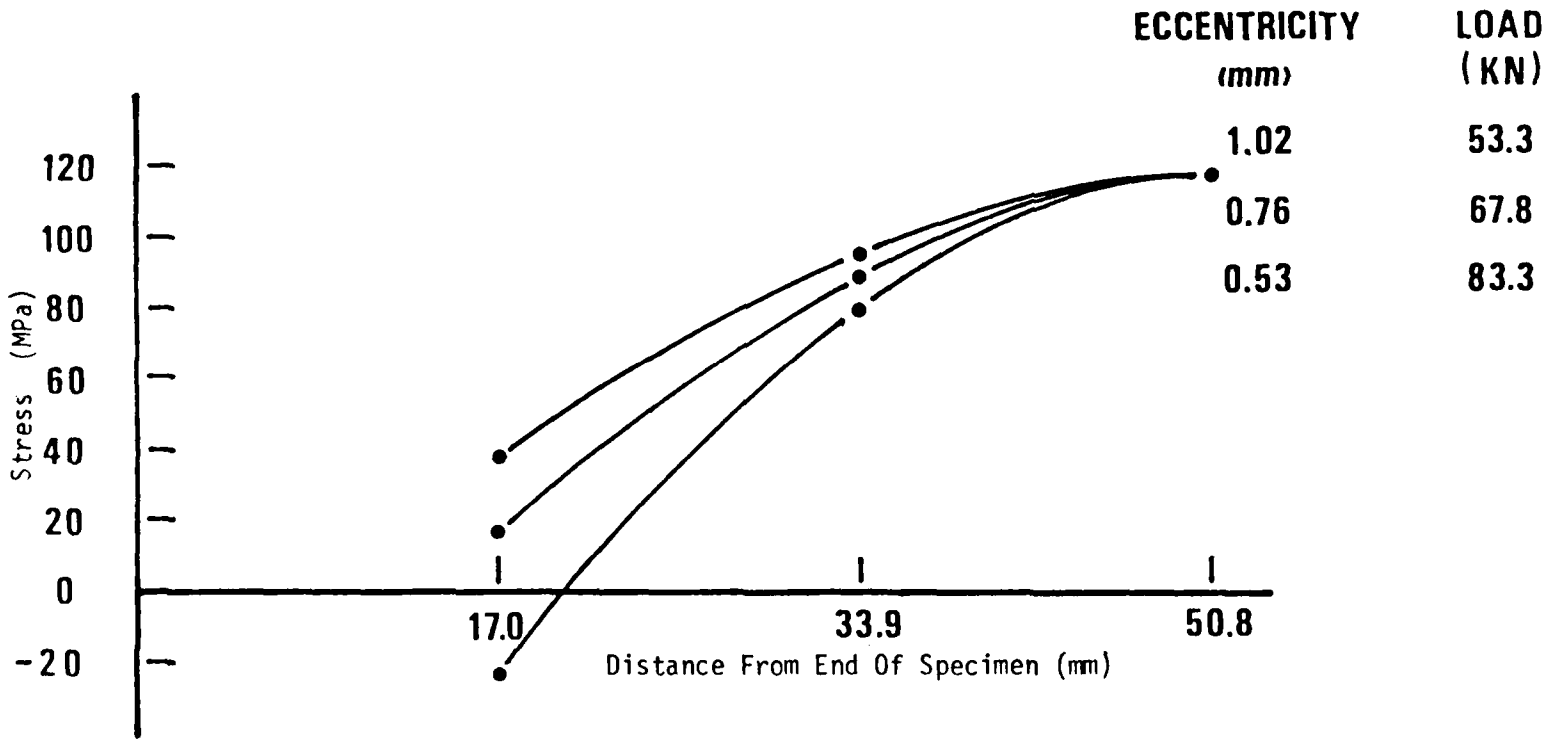

Fig. 4-15 Stress Distribution on the Tensile Surface of the Specimen.

Table 4-3. Load Path Accuracy of the Testing Apparatus

Eccentricity (mm)	Side-by-Side Accuracy (%)				Ratio	Load (kN)
	2 & 3	4 & 5	6 & 7	8 & 9		
0.53	NA	2.78	NA	0.35	14.1	83.4
0.76	3.63	2.13	3.73	0.42	11.9	67.8
1.02	NA	1.28	NA	0.41	10.1	53.4

1.02 mm jig induced 3838×10^{-6} in compressive and 380×10^{-6} in tensile strain at 53.4 kN.

The reservoir for the fluorescent dye penetrant was made out of plastic, and glued to the specimen directly with silicon glue as shown in Fig. 4-16. The reservoir was detached every time the specimen was unloaded for the microscopic examination.

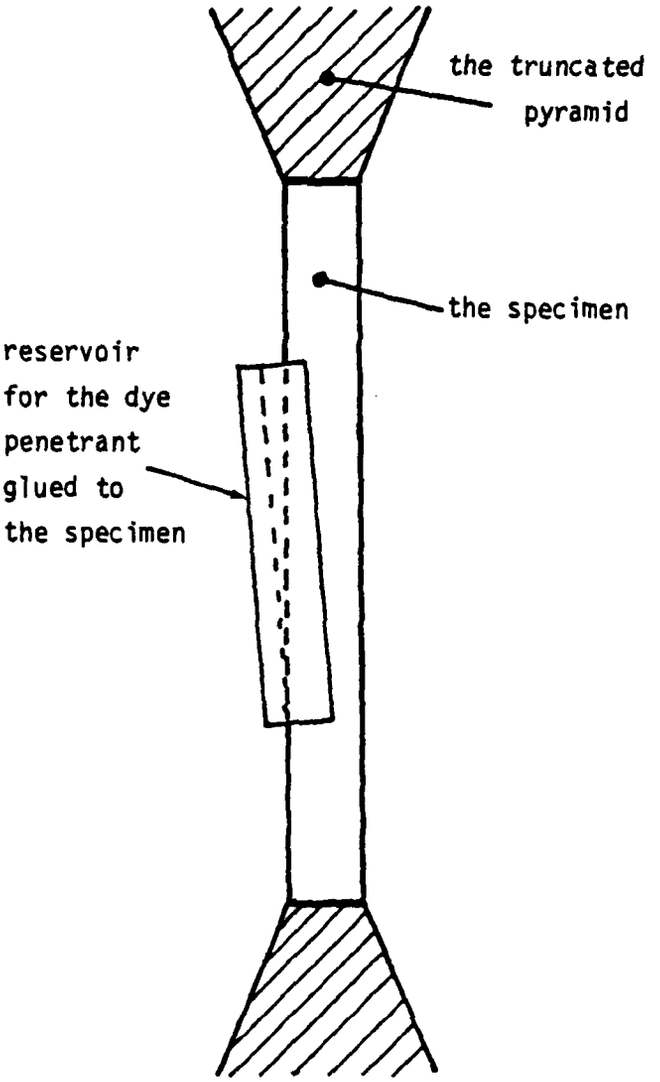

Fig. 4-16 Reservoir for the Fluorescent Dye Penetrant Attached to the Eccentrically Loaded Column Specimen.

CHAPTER V

CRACK ORIGINS AND MICROMECHANISMS

Instead of examining fracture surfaces to locate the inherent flaws responsible for the initiation of flow crack growth in the delayed fracture of alumina, direct observation of the onset of crack extension from the flaws was successfully carried out as discussed in Chapter III. The microscopic examination technique was combined with the mechanical testing technique, the eccentrically loaded column testing, described in Chapter IV to identify many potential crack sites on a surface of a specimen. When the techniques were combined, the cracks would start to emanate from the inherent flaws and would be revealed by the fluorescent dye penetrant technique. Procedure of the technique is:

(1) the specimen was cleaned with an ultrasonic cleaner,

(2) the fluorescent dye penetrant reservoir was glued to the specimen,

(3) the specimen was loaded in the eccentrically loaded column testing apparatus to a certain stress level, which was sufficiently low so that the delayed fracture would occur over from one to several days,

(4) the specimen was unloaded, and the reservoir was

detached for the microscopic examination approximately every 24 hours.

The following four figures, Fig. 5-1 to Fig. 5-4, show the composite optical micrographs with the fluorescent dye after 24, 48, 166, and 324 hours, respectively at a stress level of 124 MPa, which is 65 percent of the average fracture strength. In Fig. 5-1, notice that there is a large handling flaw or a chip at an edge of the specimen, but no linear array of the fluorescent dye spots is observed. The composite micrograph in Fig. 5-2 was taken 24 hours after Fig. 5-1. Notice that the linear array of the spots can be seen next to the handling flaw as expected. In Fig. 5-3, some more of the linear arrays of the spots can be seen while the one observed in Fig. 5-2 did not grow. Notice that the largest is found at an edge away from the center. Figure 5-4 was taken 158 hours after Fig. 5-3. The largest crack identified in Fig. 5-3 and another one went catastrophic in the transverse direction while some more of the linear arrays of the spots can be seen. As indicated in Chapter III, cracked areas that have been revealed by the dye will be examined with the scanning electron microscopy in detail to identify the critical flaws.

In section 1, the inherent flaws responsible for the initiation of slow crack growth will be identified using scanning electron micrographs of the cracked portion of the specimen surface. The microscopic cracks in this section

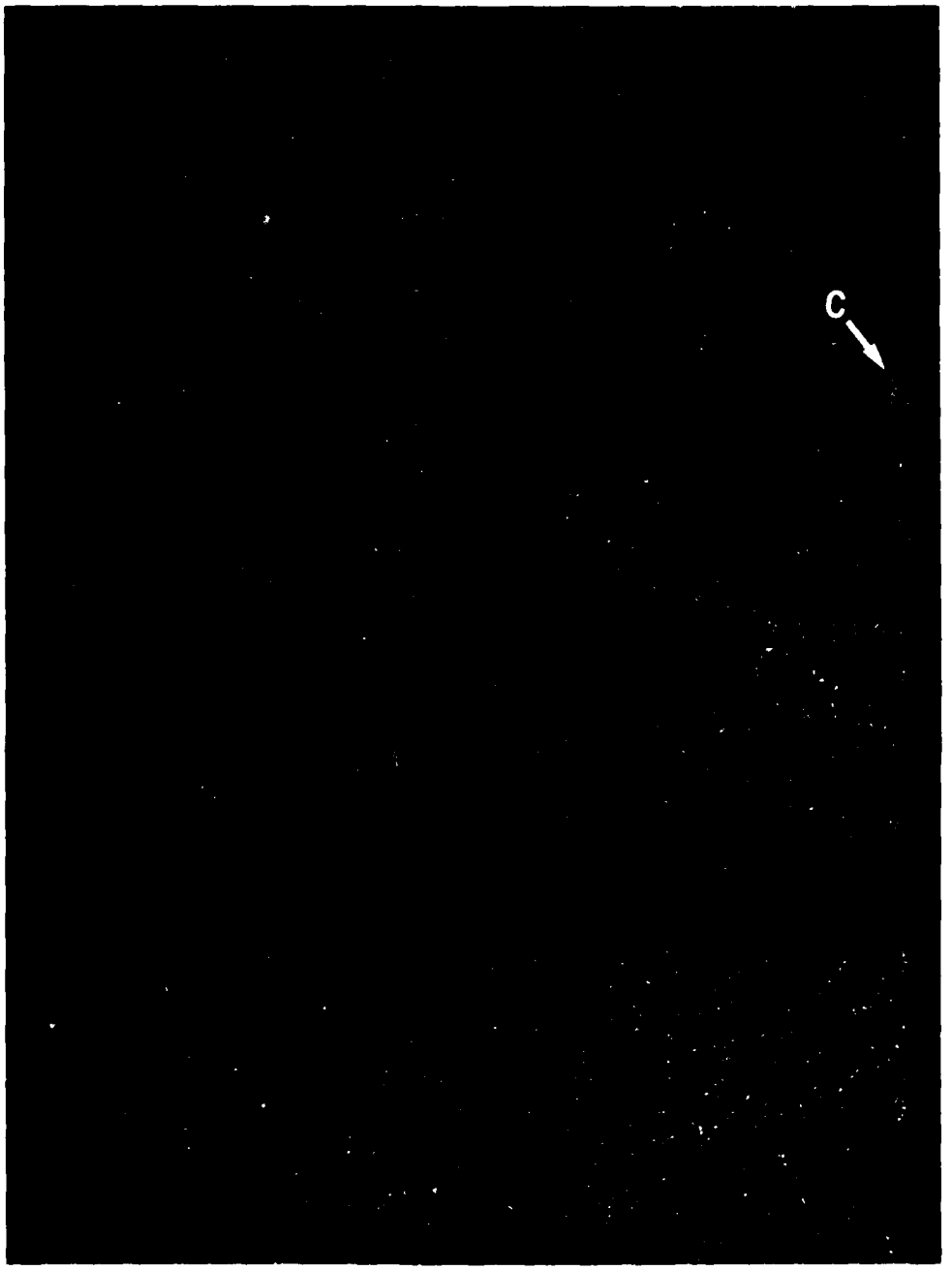

Fig. 5-1 Composite Optical Micrograph with Fluorescent Dye Penetrant after 24 hours at 124 MPa.

Notice that there is a handling flaw(C) at an edge of the specimen, but no linear array of fluorescent spots is seen.

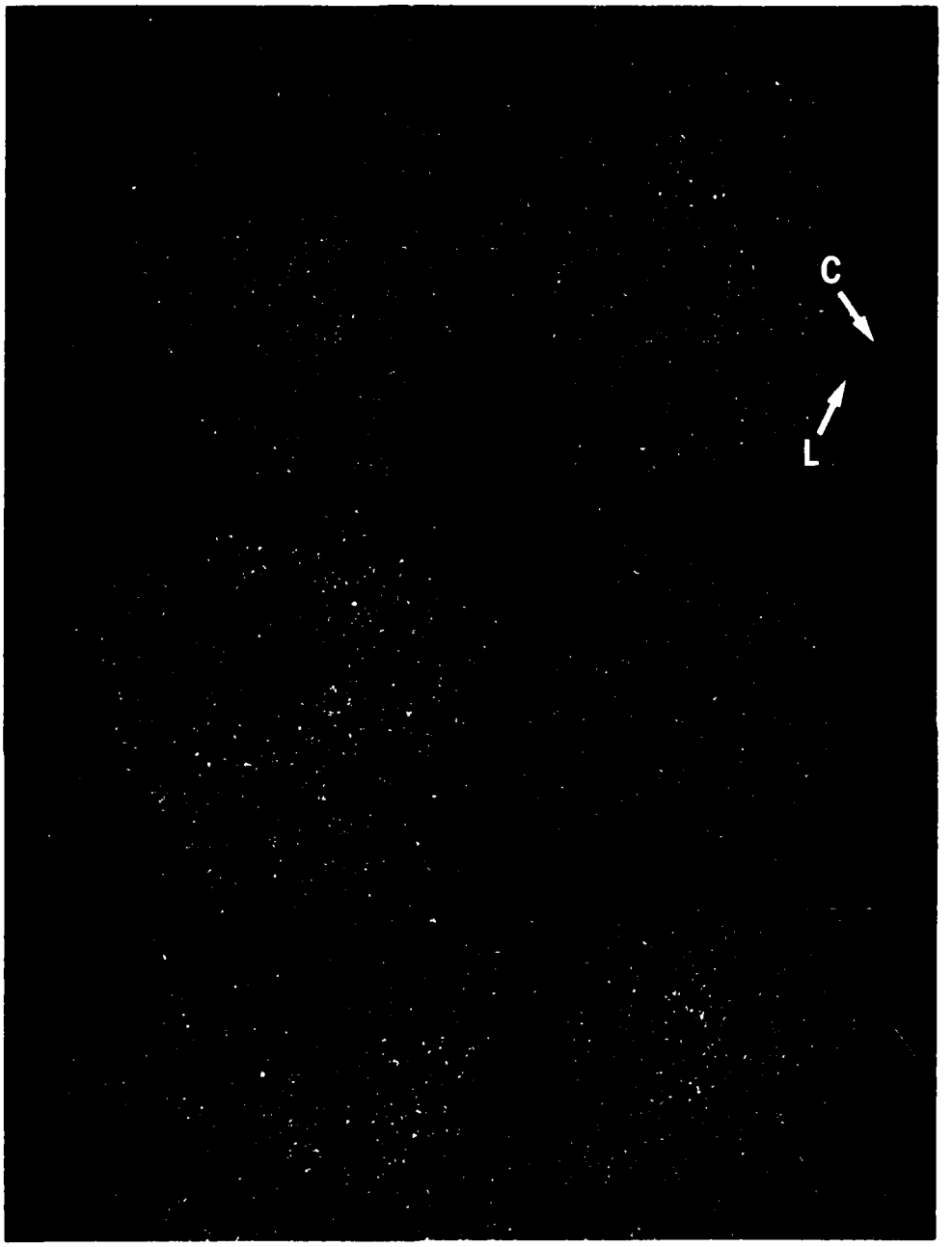

Fig. 5-2 Composite Optical Micrograph with Fluorescent Dye Penetrant after 48 hours at 124 MPa.

Notice that there is a linear array of fluorescent spots(L) near the handling flaw(C)

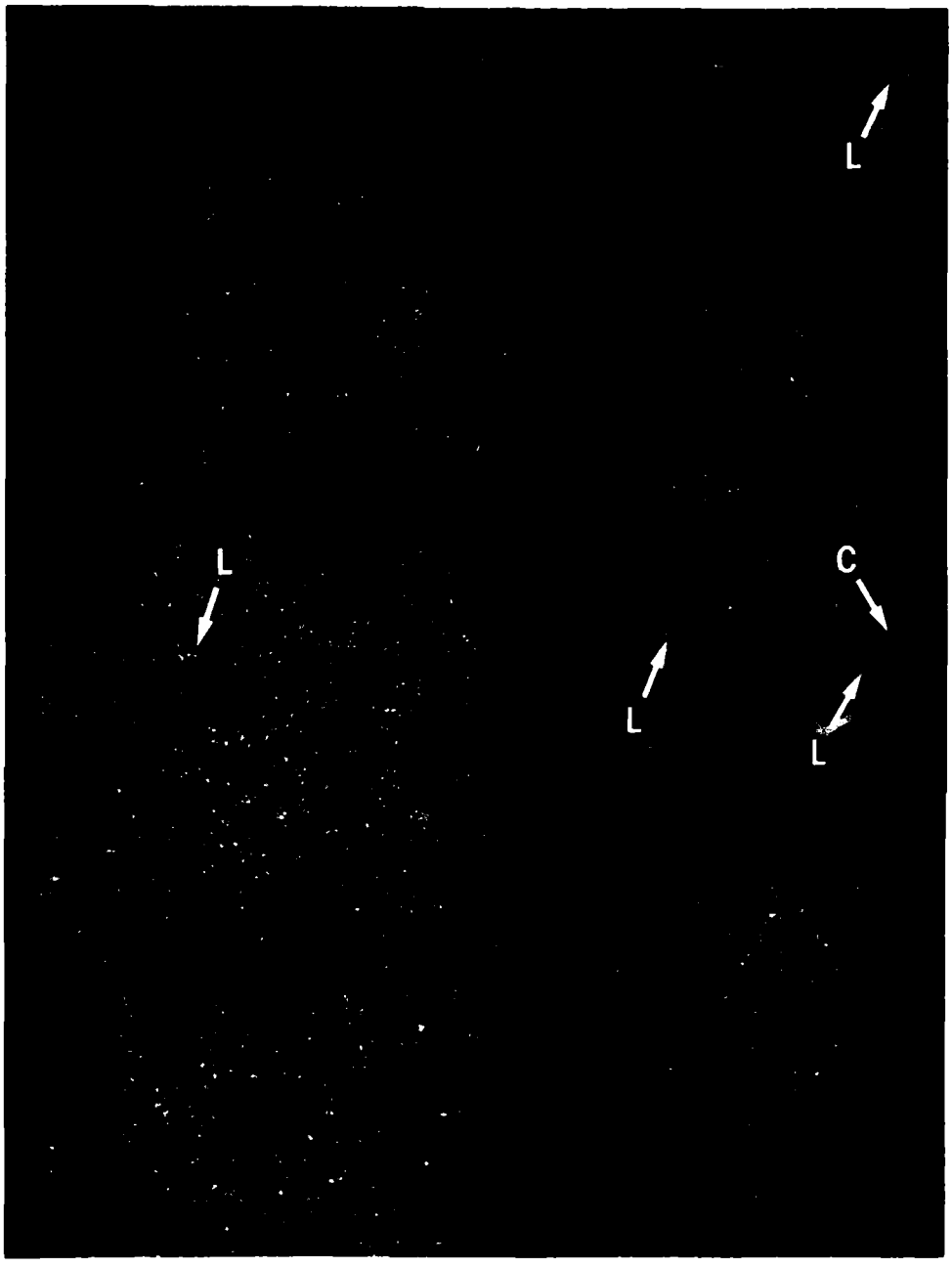

Fig. 5-3 Composite Optical Micrograph with Fluorescent Dye Penetrant after 166 hours at 124 MPa.

Notice that a few more of the linear arrays(L) appeared the largest one is located at an edge of the specimen

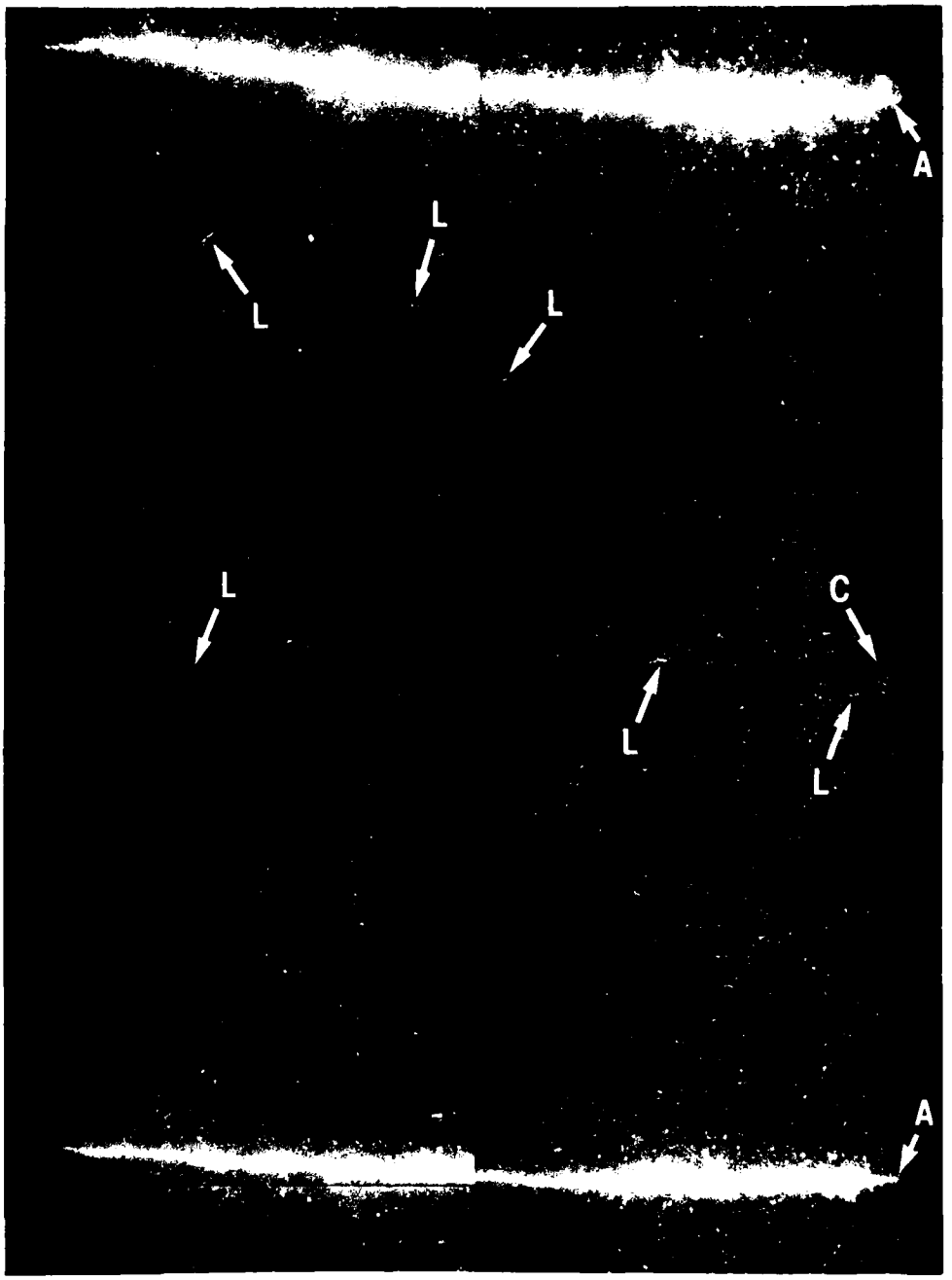

Fig. 5-4 Composite Optical Micrograph with Fluorescent Dye Penetrant after 324 hours at 124 MPa.

Notice that two cracks dynamically propagated all-the-way-across(A) while some more of the linear arrays appeared.

are the ones which did not propagate dynamically although they might have been formed by dynamic coalescence of microscopic cracks ("Pop-in"). In section 2, the micromechanisms of slow crack growth in delayed fracture will be studied based upon the experimental observation in the present study. The generalized microscopic crack growth law, based upon the local effective critical stress intensity factor and the interaction and coalescence of cracks, will be proposed. It will be shown that the proposed model gives much better prediction of time-to-failure compared with the conventional approach. In section 3, applicability of the conventional time-to-failure calculation and proof testing concept will be reexamined. Some suggestions will be made on the improvement of crack growth resistance in section 4. Failure modes, whether intergranular or transgranular, and slow crack growth in compression will be discussed briefly in section 5 and section 6, respectively.

1. Crack Origins

It is generally accepted that brittle materials fail due to cracking from preexisting flaws upon application of an external load. The preexisting flaws, intrinsic or extrinsic, may be called inherent flaws of the material. The inherent flaws which can be the potential crack origins are summarized and listed in Table 5-1.

Techniques have been developed to identify flaws responsible for the initiation of slow crack growth in delayed fracture of alumina as shown previously. It was expected that small cracks emanating from a worst flaw on a surface of a specimen could be revealed by the fluorescent dye penetrant, thereby the nature and characteristics of the flaw could be identified. However, a single worst flaw acting by itself as a crack origin was not found in the present study with the only exception of the large unsintered void shown in Fig. 3-2 in Chapter III. The actual crack origins were found to be assemblies of near-by inherent flaws connected by very fine intergranular cracks.

Since surfaces of the specimen contain a great number of inherent microscopic flaws closely distributed as can be seen in Fig. 3-11, it is obvious that there is interaction of near-by flaws. The interaction can result in higher stress intensity factors at the tips of the flaws for a given applied stress; ultimately, it can lead to dynamic coalescence ("Pop-in") of the cracks.

Table 5-1. Inherent Flaws of Ceramics

Intrinsic	Extrinsic
Pores	Machining or lapping
Grain boundary triplets	Grain pull-outs
Pores within grains	Machining cracks transverse normal
Large un-sintered voids	Grain boundary separation
Microcracks due to	
Thermal expansion anisotropy	Handling flaws
	Chips
Second phase	Impact cracks lateral cracks median cracks
Inclusions (impurities)	
Glassy phase at grain boundaries	
Twin Boundaries	

Delayed fracture is a result of the environmentally assisted slow crack growth; therefore, crack origins are on a surface of the material where an adverse chemical species can react with the material. There is numerous evidence[4] that the water of the environment interacts with the ceramic, especially with a glassy phase. The alumina used in the present study contains some silicon, calcium, and sodium which tend to form a glassy phase at grain boundaries. The glassy phase is susceptible to attack by the water. Therefore, the observation of extensive intergranular cracking, along grain boundaries, is reasonable.

Another reason why grain boundaries are likely to crack is simply because the effective fracture energy of a grain boundary is lower than the polycrystalline value due to crystal mismatch at a grain boundary. Also since alumina has the hexagonal structure, difference in thermal expansion coefficient between the c-axis and a-axis, approximately $1 \times 10^{-6}\ K^{-1}$, can cause residual strain to build up near grain boundaries. If there is a grain boundary triplet as shown in Fig. 5-5, the residual strain might be large enough to cause spontaneous cracking upon cooling[74] or to lead to premature cracking upon external loading. For larger grain sized materials, the spontaneous grain boundary cracking due to thermal anisotropy is more pronounced because the elastic strain energy available for fracture is a function of d^3, where d is grain size, whereas the effective fracture

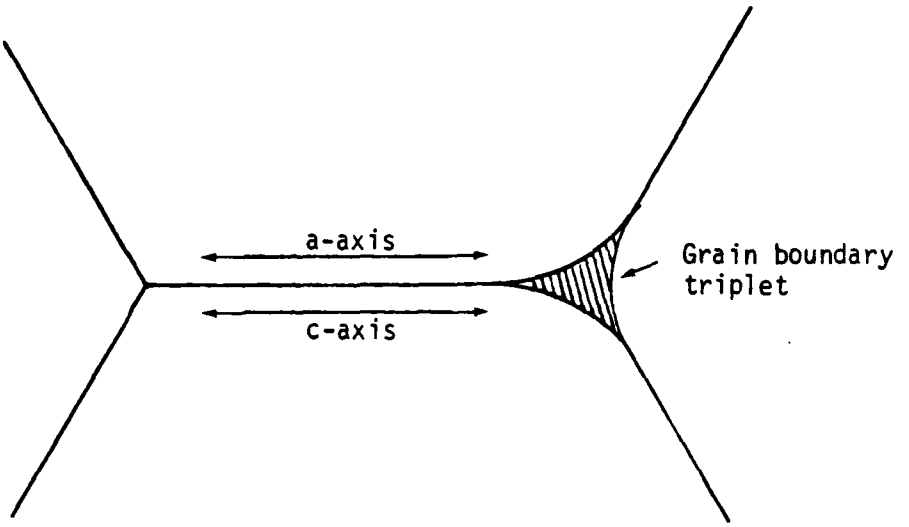

Fig. 5-5. Geometrical Configuration Which Gives Rise to Grain Boundary Cracking Due to Thermal Expansion Anisotropy Between a-axis and c-axis.

energy is a function of d^2. This is analogous to nucleation and growth of a particle, where there is a critical particle size for stable nucleation and growth.

Some clear examples of crack origins which involve the interaction and coalescence of inherent flaws are shown in Fig. 5-6 to Fig. 5-9. The cracks shown did not propagate dynamically; notice that some inherent flaws are seen to be connected by very fine intergranular cracks. It is now clear that the interaction and coalescence of multiple cracks must be considered in slow crack growth of alumina instead of the simplistic single-worst-flaw concept. It is also clear that the effective fracture energy may be controlled by the grain boundary fracture energy which is significantly lower than its polycrystalline value and is somewhat close to the single crystal cleavage energy.

Another typical example of the early stage of crack growth is shown in Fig. 5-10. A machining or lapping flaw and an inherent flaw are seen to be connected by a fine crack. Machining and lapping are known to create a surface damage layer, consisting of a machining crack and a plastic deformation zone as schematically shown in Fig. 5-11. The plastic zone acts as a wedge leaving a localized residual stress at the crack tip. This is similar to damage caused by the indentation process. Figure 5-12 illustrates an example of machining or lapping damage which occurred when a hard machining particle intersected an inherent flaw.

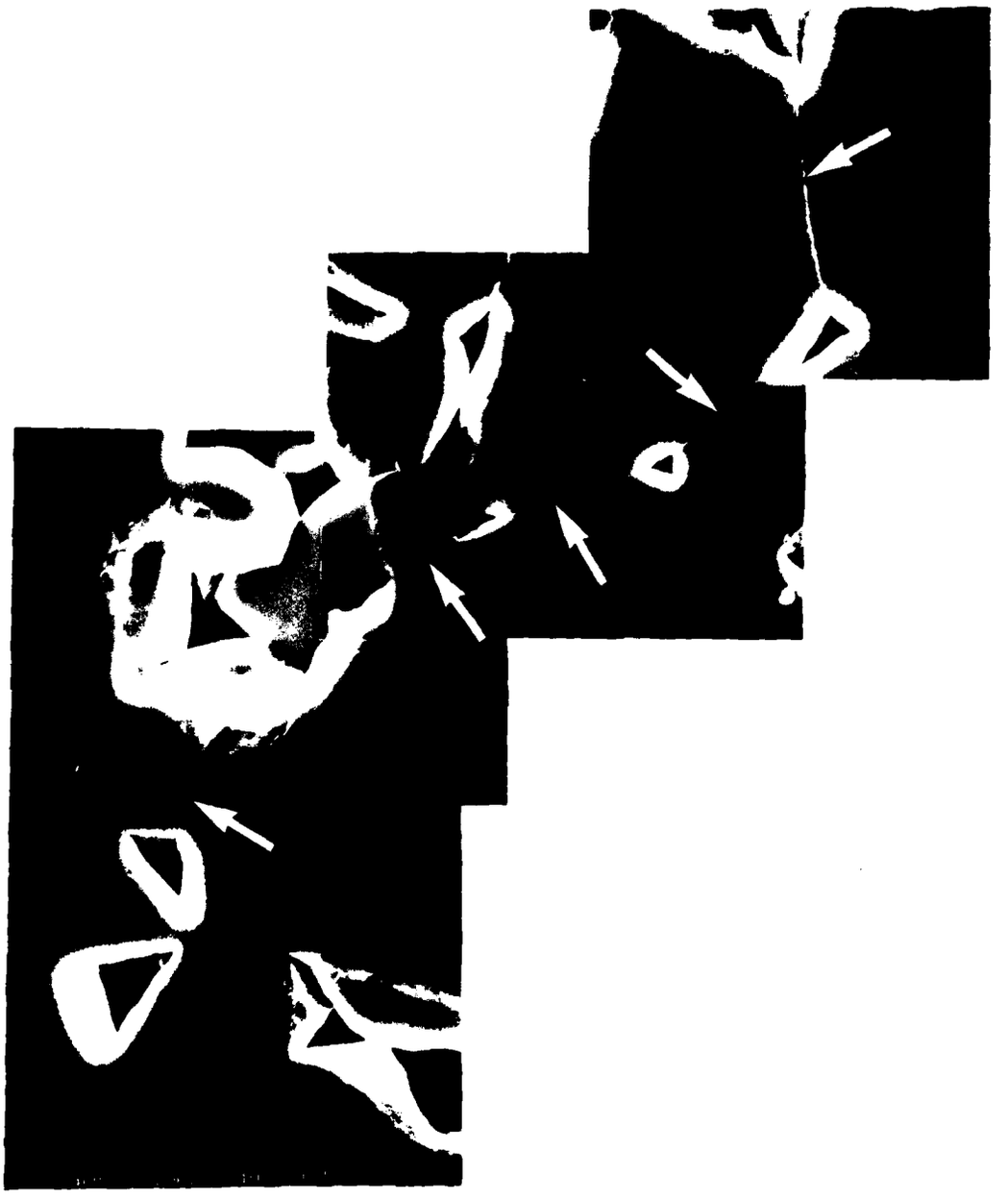

Fig. 5-6 Scanning Electron Micrograph Revealing Some Inherent Flaws and Intergranular Cracks Connecting the Flaws (the cracks are indicated by arrows)

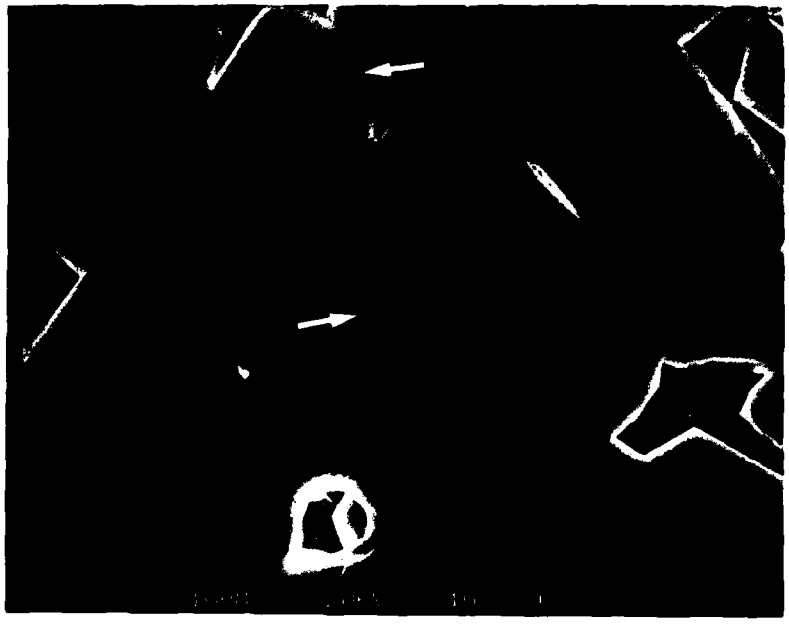

Fig. 5-7 Scanning Electron Micrograph Revealing Some Inherent Flaws and Intergranular Cracks Connecting the Flaws (the cracks are indicated by arrows)

Fig. 5-8
Scanning Electron Micrograph Revealing Some Inherent Flaws and Intergranular Cracks Connecting the Flaws.
(the cracks are indicated by arrows)

Fig. 5-9 Scanning Electron Micrograph Revealing Some Inherent Flaws and Intergranular Cracks Connecting the Flaws. (the cracks are indicated by arrows)

Fig. 5-10 Scanning Electron Micrograph Revealing a Machining Crack(A) Which is Connected to the Near-by Flaw by a Fine Crack(B).

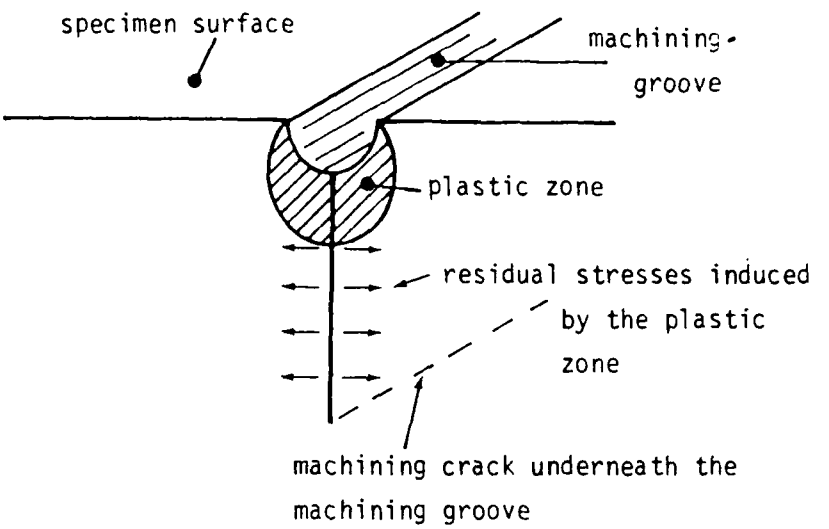

Fig. 5-11 Schematic Representation of Machining Crack with Residual Stresses Due to Plastic Zone.

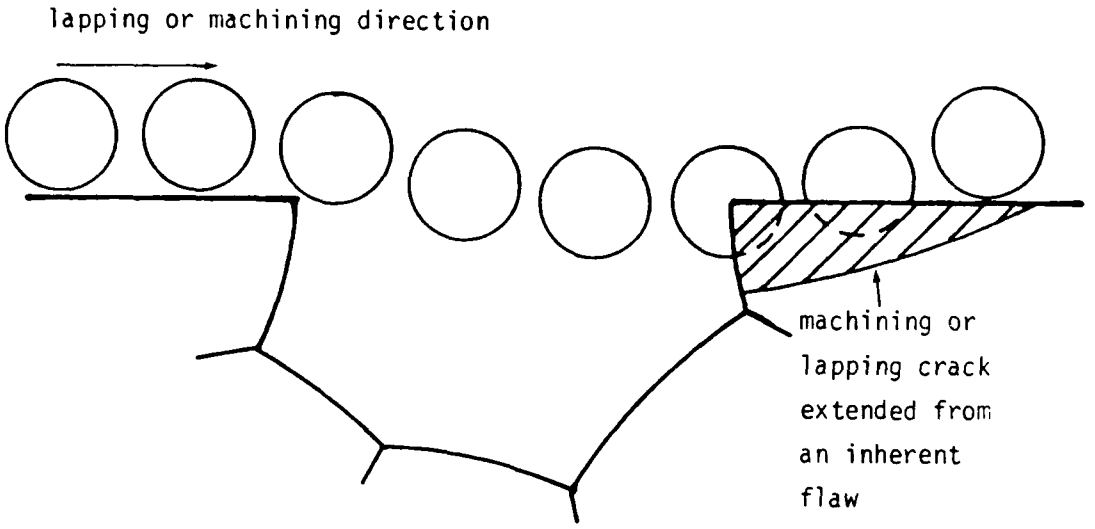

Fig. 5-12 Schematic Representation of Machining Crack Formation Due to Interaction of Hard Particles with an Inherent Flaw.

It seems that machining cracks are more pronounced at the inherent flaws; therefore, machining cracks may act as an extension of flaws. The phenomena can be called "Comet-tails", and a typical example is shown in Fig. 5-13.

Another important point to be noticed is that in delayed fracture, it was found that sites for crack origins can be multiple as seen in Fig. 5-4, depending upon applied stress and time. Some crack sites may be potentially critical, and some may not. Since many crack sites appear with time under a constant stress, it indicates that a worst crack site for the strength test (fast fracture) may not be the worst crack site for the delayed fracture test. In other words, for a given stress, microscopic cracks emanate from inherent flaws and coalesce with time to form a macroscopic crack which may become stable due to the local microstructural heterogeneity, meantime other microscopic cracks interact and coalesce to form other macrocracks which may become stable, and so on. In order to cause catastrophic failure, either the coalesced macroscopic crack grows to a critical size or the stress intensity factor of a total assembly of small cracks exceeds the critical value. A detailed discussion on the micromechanisms of slow crack growth will be presented in the following section.

Fig. 5-13 Scanning Electron Micrograph Revealing a Grain Pull-out(G) and a Comet-tail(C).

2. Micromechanisms of Slow Crack Growth in Delayed Fracture of Alumina

A scenario of slow crack growth in delayed fracture can be written as follows based upon direct observation made in the present study:

(1) The specimen surface has a random distribution of the inherent flaws as shown in Fig. 5-14a. There are some potential sites for crack origins.

(2) Small cracks start emanating from the flaws due to stress enhanced chemical reaction. The local stress intensity factor is affected by the interaction of the microscopic cracks, and crack velocity is affected by the local heterogeneity as shown in Fig. 5-14b.

(3) Some microscopic cracks, which grew from the inherent flaws, dynamically coalesce to form a larger crack. Then there are two possibilities from this point in order to cause catastrophic failure: (a) the coalesced crack continues to grow to the critical size, or (b) the stress intensity factor of a total assembly of small cracks exceeds the critical value.

Two important questions arise concerning crack growth behavior:

(1) How does a microscopic crack grow; does it follow the well-established slow crack growth law given

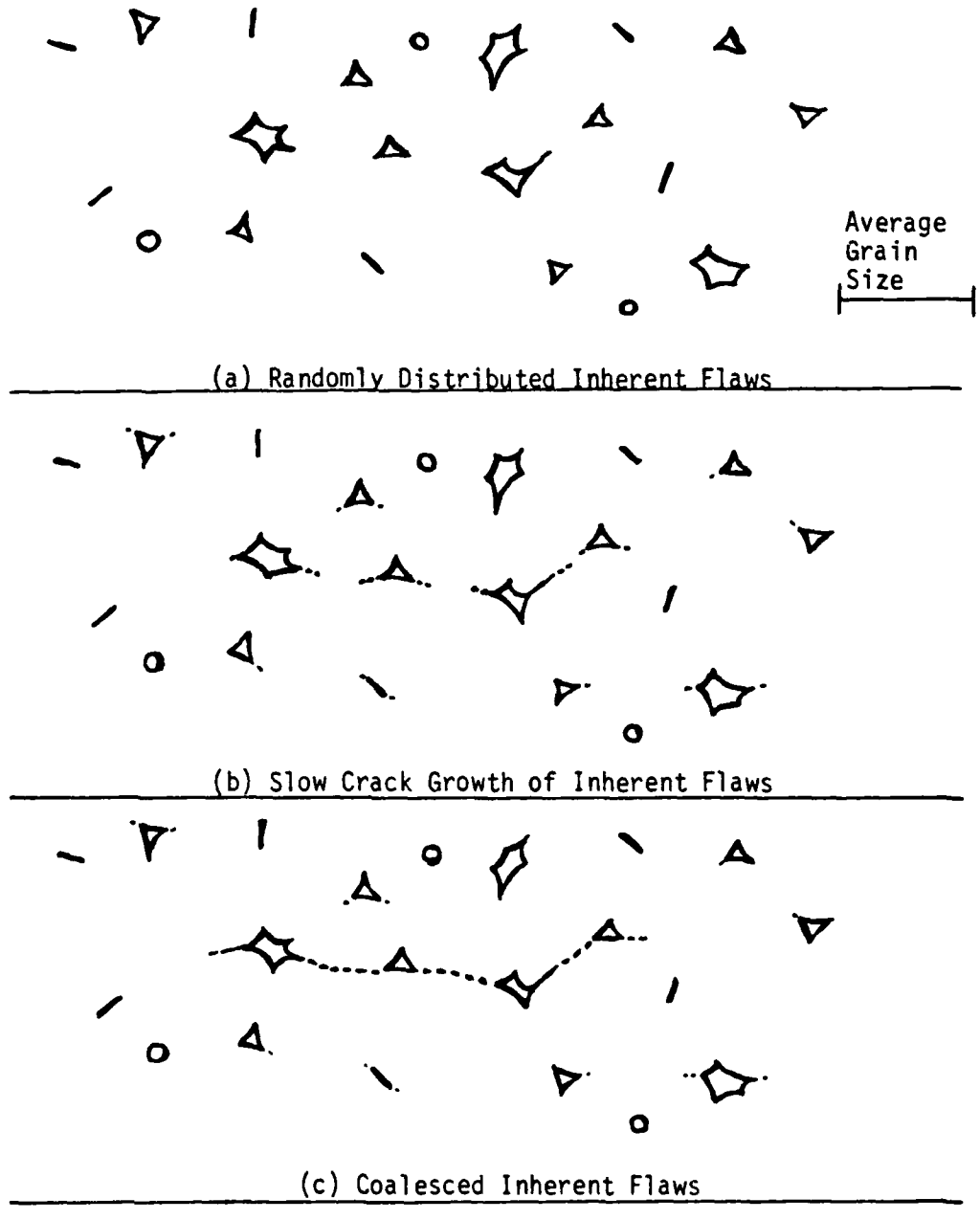

Fig. 5-14. A Scenario of Slow Crack Growth in Delayed Fracture

in eq. (2-14)?

$$da/dt = A K^n \qquad (2\text{-}14)$$

(2) How is crack growth affected by the interaction and coalescence of cracks?

The objective of this section is to provide answers to the above questions. In section 2.1, the microscopic single crack growth law, using the concept of the effective critical stress intensity factor, will be proposed. In section 2.2, a mathematical model will be used to demonstrate the effect of the interaction and coalescence of microscopic cracks of the time-to-failure in delayed fracture using the single crystal critical stress intensity factor. In section 2.3, the single microscopic crack growth law and the concept of the interaction and coalescence of cracks will be combined to obtain the generalized microscopic crack growth law. Calculated time-to-failure based upon the proposed analysis will then be compared with the experimental data and with the conventional approach. It will be shown that the proposed analysis gives much better prediction than the existing one.

2.1 The Single Microscopic Crack Growth Law

It is generally accepted that slow crack growth from inherent flaws often precedes fracture of a ceramic material.[50,75] If a microscopic crack grows from an inherent flaw, then the accuracy of a calculated time-to-failure based upon the macroscopic crack growth law given in eq. (2-14) and eq. (2-15) becomes questionable since the critical size is in a microscopic dimension for a reasonable operating stress.

When a microscopic crack exists in a grain, the crack must behave as if it were in a single-crystal solid. It has been known that the fracture energies for single crystal and polycrystalline solids of the same material are often different due to microscopic heterogeneities.[50] In fact, an entire curve of slow crack growth law for the single crystal sapphire in (1012) plane[4] lies below what is generally believed as the static fatigue threshold for a coarse-grained (25 μ) polycrystalline alumina[31] in 50% relative humidity as shown in Fig. 5-15. Therefore, it is necessary to have a "microscopic crack growth law" in order to characterize behavior of a microscopic crack. In this section, an isolated microscopic crack growth law will be developed based upon the local effective critical stress intensity factor concept.

In order to construct the microscopic crack growth law, the following assumptions were made:

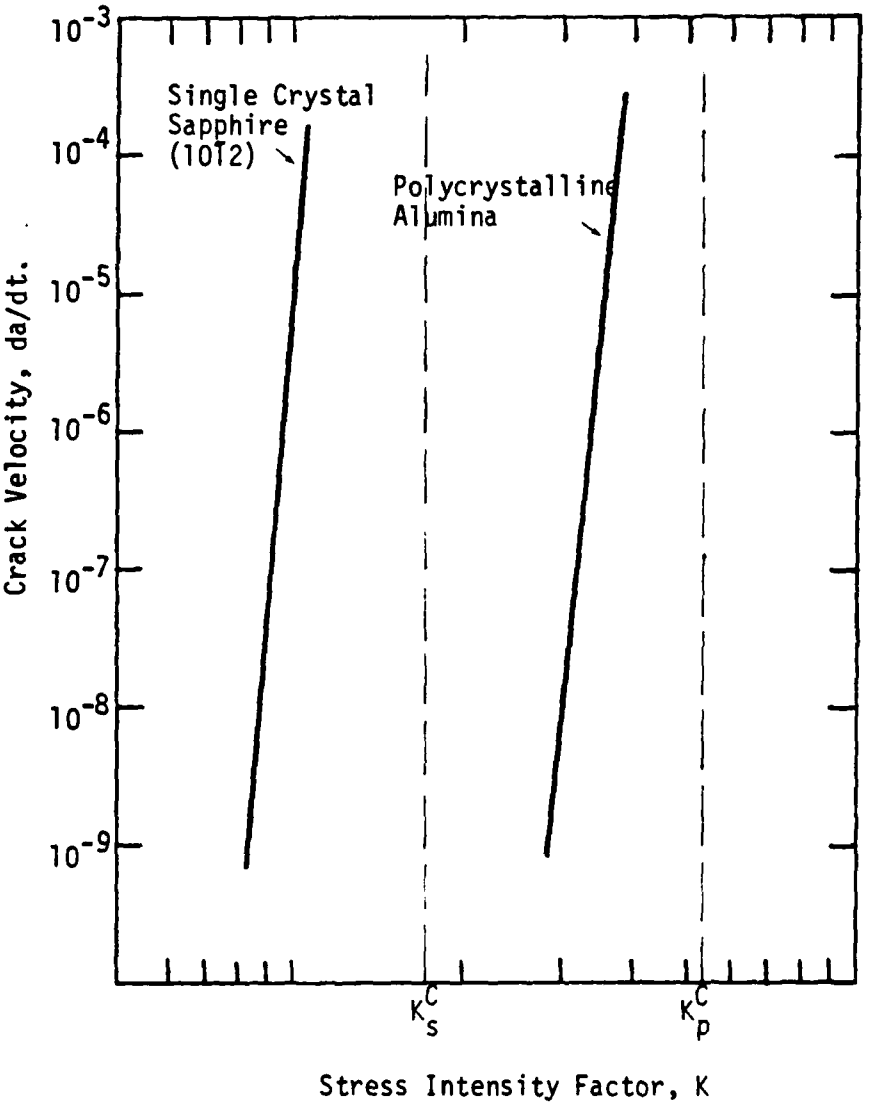

Fig. 5-15 Crack Velocity vs Stress Intensity Factor Obtained From Single Crystal Sapphire[4] and Polycrystalline Alumina in 50 % Relative Humidity.[31]

(1) the material constants under a certain environment, A, B, and n in eq. (2-14) and eq. (2-15), evaluated from the conventional macroscopic crack growth law, are valid,

(2) the local heterogeneity due to residual stresses or different crystal orientations can be expressed solely in terms of the effective critical stress intensity factor, K^C_{eff}, and

(3) crack velocity at an instant can be given as a function of the ratio between the stress intensity factor and the local effective critical stress intensity factor, that is

$$da/dt = v = B(K/K^C_{eff})^n \qquad (5\text{-}1)$$

where K^C_{eff} = the local effective critical stress intensity factor

Equation (5-1) is a general case of the macroscopic crack growth law formulated by Sines[34] given in eq. (2-15).

In order to justify the assumptions (1) to (3), the slow crack growth curves shown in Fig. 5-15 were replotted in Fig. 5-16 according to eq. (5-1). A good matching of the curves can be seen; therefore, it was confirmed that the assumptions are appropriate.

The local heterogeneity is almost always present in any polycrystalline material due to different crystal

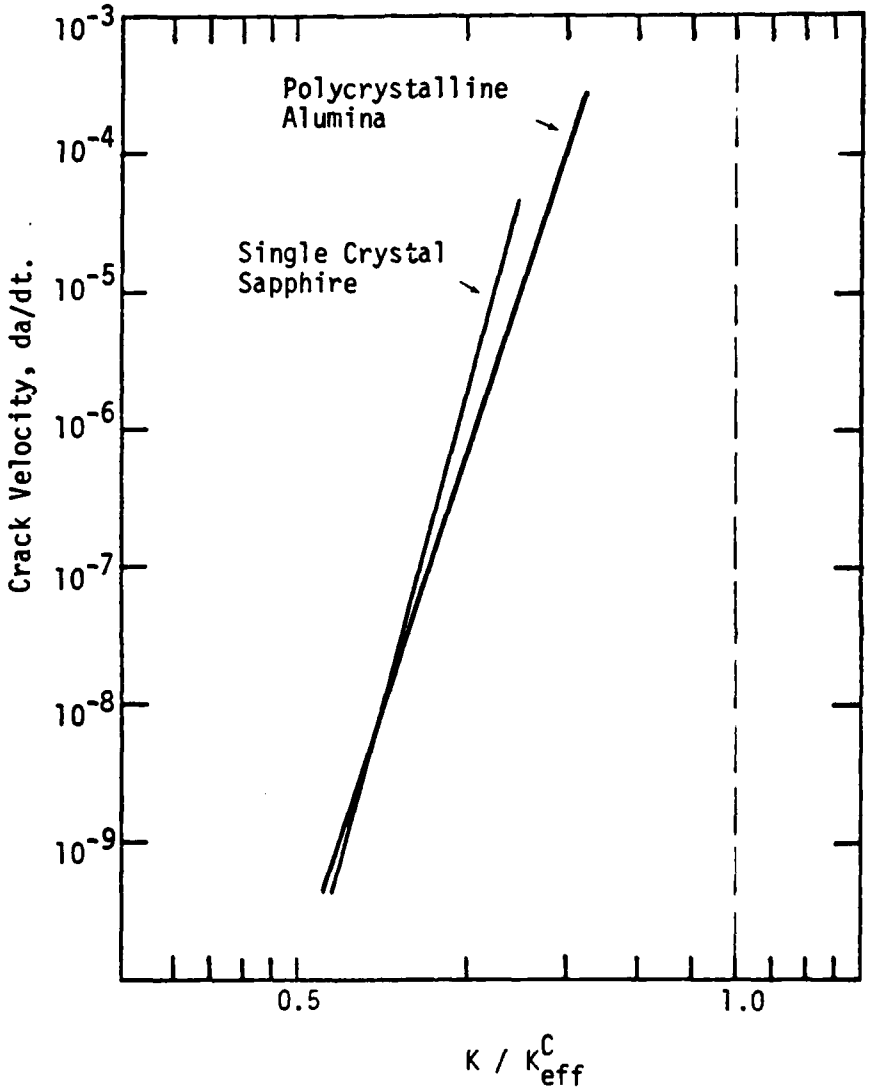

Fig. 5-16 Replotted Crack Velocity vs Stress Intensity Factor Shown in Fig. 5-15; Stress Intensity Factor Is Normalized According to Eq.(5-1)

orientations, fracture energy anisotropy of crystal planes, or localized residual stresses. If a crack propagates through the different heterogeneities, the local crack velocity must be controlled by the local heterogeneity. Therefore, eq. (5-1) may be interpreted as a group of lines with B and n being constant and with K^C_{eff} being the only variable as schematically illustrated in Fig. 5-17. Figure 5-17 represents an example of the single microscopic crack growth model which is proposed here. The implication of the law is that the crack growth rate shifts as the crack tip encounters different local heterogeneities. For example, a crack may encounter a grain unfavorably oriented for crack growth or a residual compressive stress, then the growth rate shifts down to an appropriate one of the lines to accommodate the change. This is illustrated in Fig. 5-18. A microscopic crack is assumed to exist within a grain in this example, as shown in Fig. 5-19. When an appropriate external load is applied, the crack starts to propagate. When the crack reaches the next band of grains, at point A, the growth rate shifts due to the different local heterogeneity. The growth rate shifts again at B and C. When the crack encounters a band of grains with many grains unfavorably oriented, the crack velocity drops dramatically at D. The crack velocity becomes so low that the crack may look as though it were arrested. When the crack slowly propagates and reaches the next band of grains, the rate

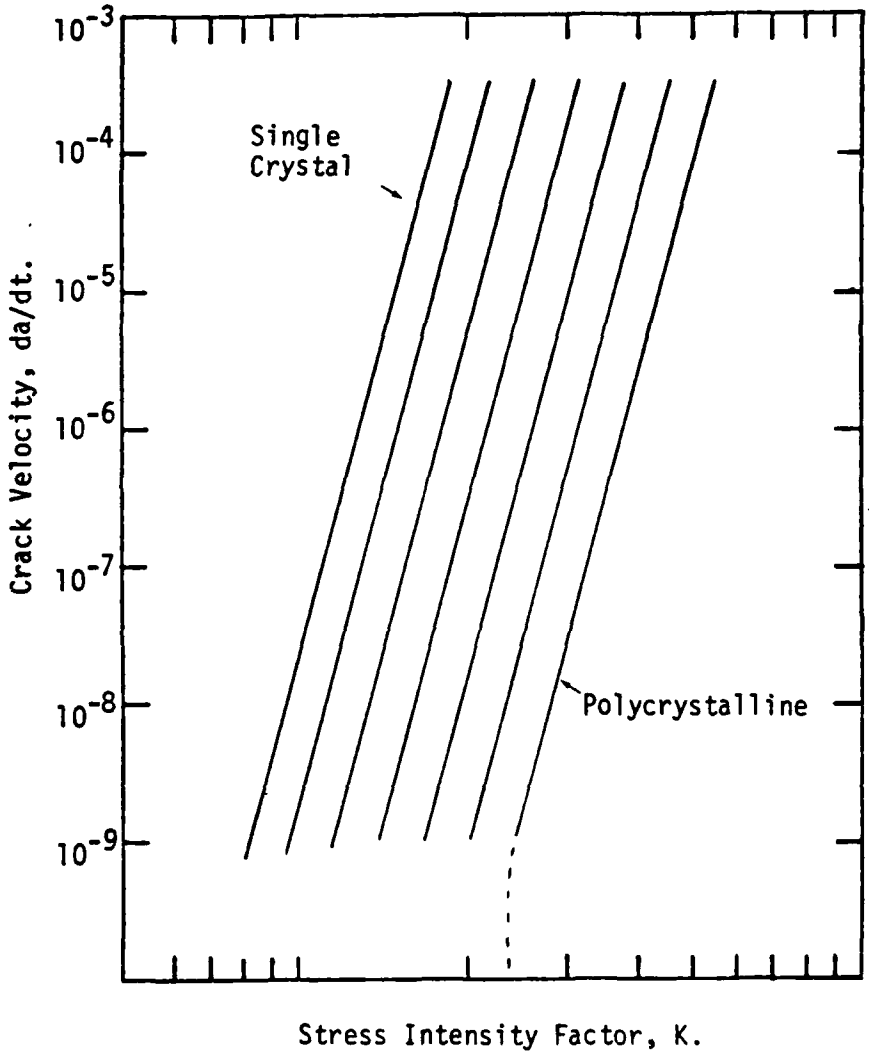

Fig. 5-17 The Single Microscopic Crack Growth Law Shown As A Group of Discrete Crack Growth Line.

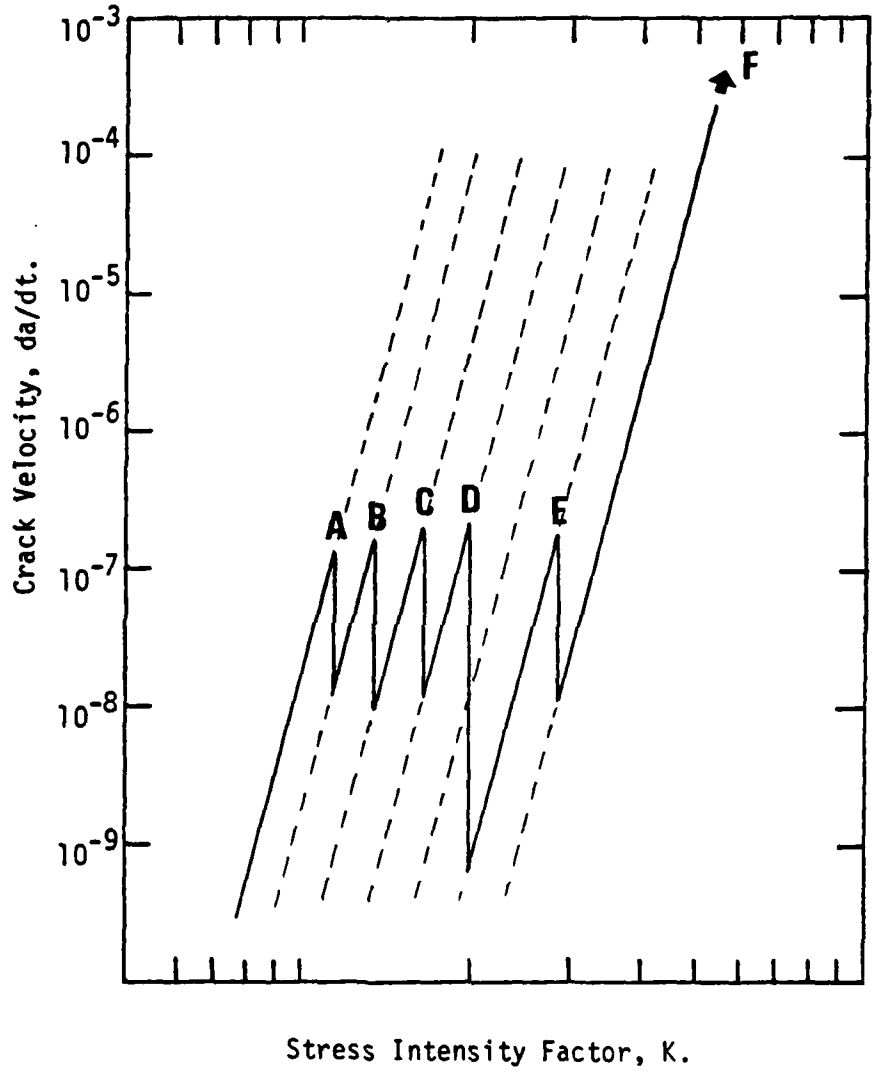

Fig. 5-18 An Example of The Microscopic Crack Growth.

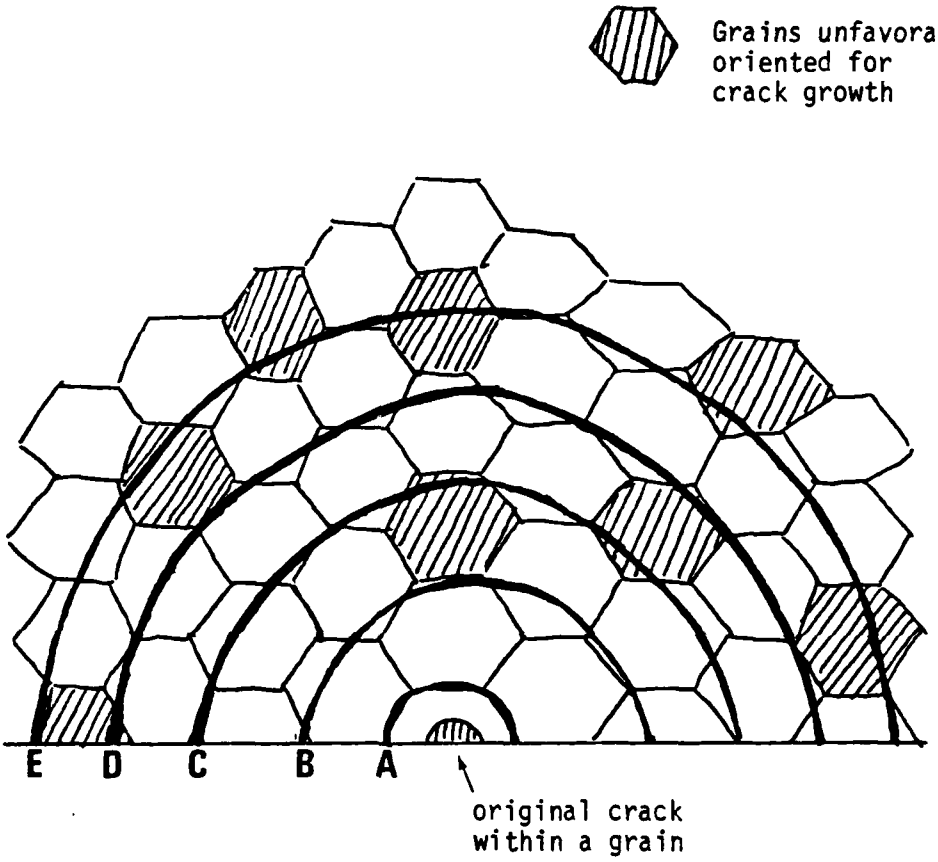

Fig. 5-19 Crack Growth Through Different Local Heterogeneities and Anisotropies.

shifts again at E. At this point the crack might be large enough to average out the local heterogeneities; therefore, it starts to behave like a macroscopic crack, and it follows the well-established macroscopic crack growth law until the crack size becomes critical for catastrophic failure. A possible example of crack growth shown in Fig. 5-18 somewhat resembles the crack growth curve taken from the Space Shuttle tile[76] which is highly anisotropic material.

Since any crystalline material is anisotropic in microscopic dimensions, the proposed approach seems reasonable. This approach also explains the possibility of the existence of a different crack growth law near the static fatigue threshold as speculated by Soma et al.[52] Kirchner[75] used only the single crystal and the polycrystalline fracture energy to calculate the time-to-failure in a very large-grained alumina, but did not consider the transition regime; therefore, when the grain size is not so large, the calculation is not applicable.

It has been demonstrated here that a microscopic crack may grow according to several discrete crack growth rates due to local heterogeneity. It is now essential to investigate how the local heterogeneity changes; thus, the discrete crack growth rates may be determined for the microscopic crack regime.

It has been shown that the effective critical stress intensity factor has a functional relation with crack-to-

grain size ratio[48-51] as schematically shown in Fig. 2-11. The reason why there is such a transition regime in the effective critical stress intensity factor, or the effective fracture energy, is the following:

Single crystals have a wide variation in fracture energy depending upon the crystal orientation. When a crack has microscopic dimensions, fracture is affected by the microstructural heterogeneity. However, when a crack is sufficiently large, the effect of the local heterogeneity lessens or averages out; therefore, fracture is controlled by an intermediate value. In other words, a cleavage plane in a single crystal may have a smaller fracture energy and another plane may have larger fracture energy than the polycrystalline value, as schematically shown in Fig. 5-20. Wiederhorn[77] studied the fracture energy of sapphire in different crystal planes, namely the (0001) basal plane, the $(10\bar{1}0)$ prismatic plane, and the $(\bar{1}012)$ rhombohedral plane. The fracture energies for the latter two planes were 7.3 and 6.0 J/m^2. The fracture energy for the basal plane could not be measured because the fracture path did not follow the basal plane; therefore, he concluded that the value must be greater than the observed value of 40 J/m^2. It is important to notice that there are 18 planes of $(10\bar{1}0)$ and $(\bar{1}012)$ and only one plane of (0001) in a unit cell. Therefore, the probability of finding a lower energy plane is much greater than that of finding a higher one.

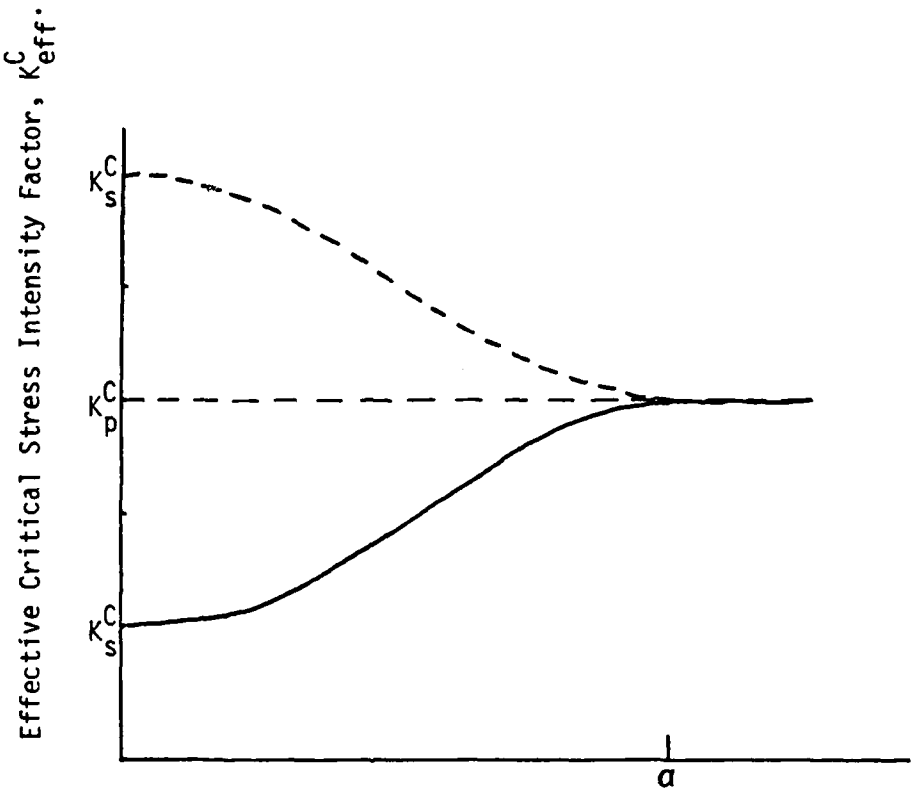

Fig. 5-20 Functional Relationship Between The Effective Critical Stress Intensity Factor and Crack-to-Grain Size Ratio. a is the critical value above which the effective critical stress intensity factor is constant, K^C_p.

This greater probability is even magnified by Sohncke's normal stress law[78] which states that the normal stress component on cleavage planes starts to decrease significantly only at ± 40 degrees from the plane perpendicular to the applied tensile axis. The fact that the basal plane has the highest fracture energy and the others have much lower values was verified by Becher[79] as shown in Fig. 5-21. Implications are that a microscopic crack started on a cleavage plane of a grain will have more chance of encountering the planes of lower fracture energy as the crack advances, and that the transition to the polycrystalline regime must be smooth rather than abrupt. A similar phenomenon of transition in fracture energy was studied in the case of residual stresses induced by phase transformation of $BaTiO_3$.[80] Since alumina has the hexagonal structure, the effect of induced residual stresses due to differences in the coefficient of thermal expansion may have to be taken into consideration. However, for the sake of simplicity, the effect is neglected in the present study.

If the effective critical stress intensity factor is assumed to have a functional relationship with crack-to-grain size ratio as shown in Fig. 2-11, that is to say K^C_{eff} approaches K^C_p and K^C_s asymptotically, a possible functional relation may be written as

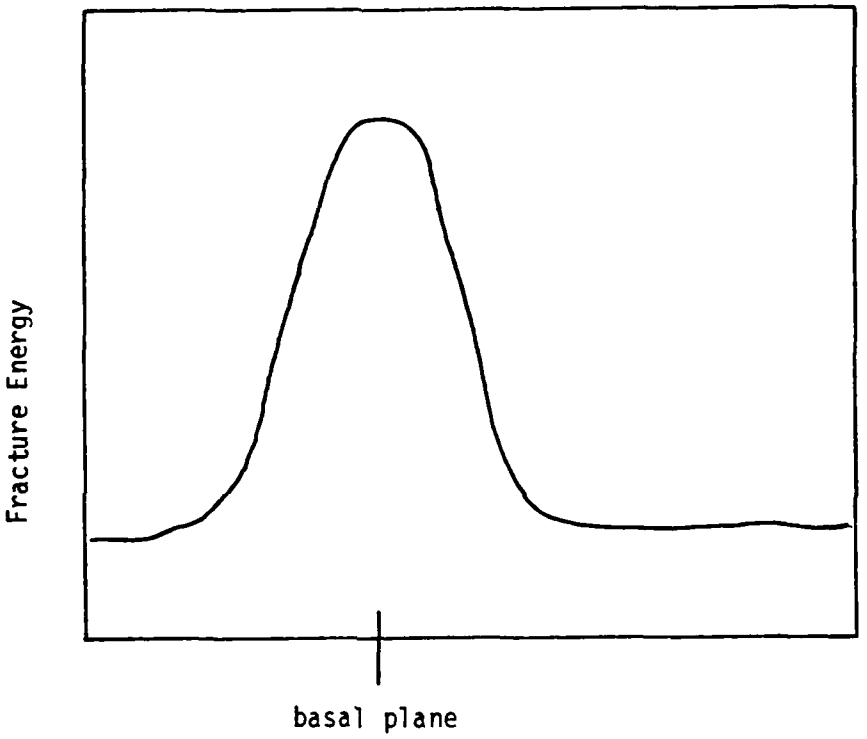

Fig. 5-21 Fracture Energy of Single Crystal Al_2O_3 as a Function of Crystal Orientation.

Notice that the fracture energy is low in wide range of orientations and very high in the basal plane.[79]

$$K^C_{eff} = \begin{cases} K^C_p\{1 - \beta + \beta\cos(\frac{a}{d\alpha} - 1)\pi\} & \frac{a}{d\alpha} < 1 \\ K^C_p & \frac{a}{d\alpha} > 1 \end{cases} \qquad (5\text{-}2)$$

$\beta = 1/2(1 - K^C_s/K^C_p)$

α = a critical value of a/d above which $K^C_{eff} = K^C_p$

K^C_p = polycrystalline critical stress intensity factor

K^C_s = single crystal critical stress intensity factor

a = one-half crack length

d = grain size

Although Virkar et al.[51] used a function of the form:

$$K^C_{eff} = K^C_s[1 + \kappa\,(1 - e^{-\chi^2})] \qquad (5\text{-}3)$$

where $\kappa = K^C_p/K^C_s - 1$

$\chi = a/d\omega$

ω = dimensionless constant

the author chose the expression in eq. (5-2) for each of mathematical manipulation since both curves give the similar behavior: K^C_{eff} approaches K^C_p and K^C_s asymptotically.

If we assume that microscopic crack growth depends solely upon the local effective critical stress intensity factor given in eq. (5-2), a grain-sized crack growth

according to the solid line in Fig. 5-22. Notice that a local crack velocity depends upon the functional relation selected. From eq. (5-1), a local velocity at a beginning of j-th band of grains can be obtained as

$$\left(\frac{da}{dt}\right)_j = B\left(\frac{K}{K^C_{eff}}\right)^n$$

$$= B\left(\frac{Y\sigma\sqrt{jd}}{K^C_{eff}}\right)^n$$

$$= \begin{cases} B\left(\frac{Y\sigma\sqrt{d}}{K^C_p}\right)^n \left\{\frac{\sqrt{j}}{1-\beta+\beta\cos\left(\frac{j}{\alpha}-1\right)\pi}\right\}^n & \frac{a}{d\alpha} < 1 \\ B\left(\frac{Y\sigma\sqrt{dj}}{K^C_p}\right)^n & \frac{a}{d\alpha} > 1 \end{cases} \qquad (5\text{-}4)$$

The local crack velocity changes rapidly as shown in Fig. 5-23. In Fig. 5-23, the effective critical stress intensity factors and the local crack velocities are plotted against the crack-to-grain size ratio with various values of α, the critical value of crack-to-grain size ratio above which the critical stress intensity factor is constant, K^C_p. Region I, II, III, and IV shown in Fig. 5-23 are defined as follows: Region I is a low crack velocity region where on or two grain sized crack just started. Region II is where the crack-to-grain size ratio is about two to three, and crack velocity has its maximum. Region III is where the crack-to-grain size ratio is about four to eight depending upon

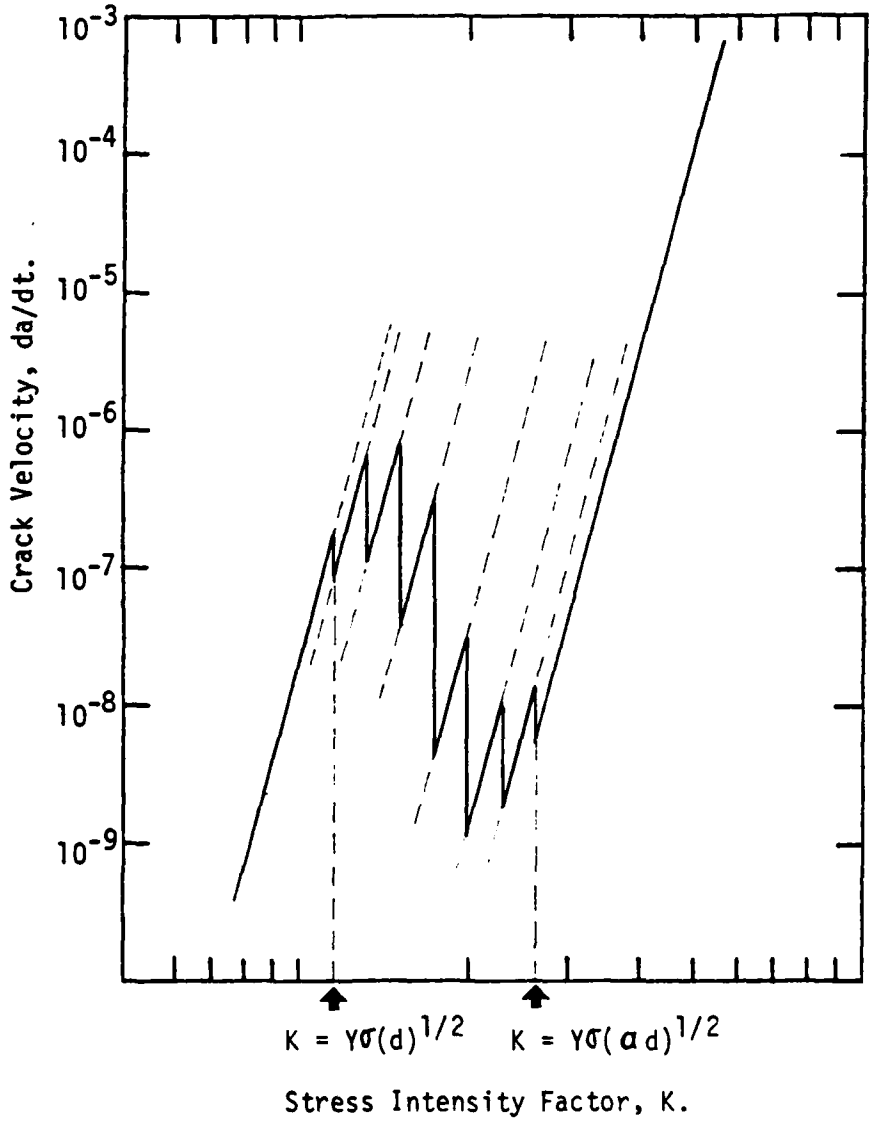

Fig. 5-22 The Microscopic Crack Growth Law Based Upon Eq.(5-2).

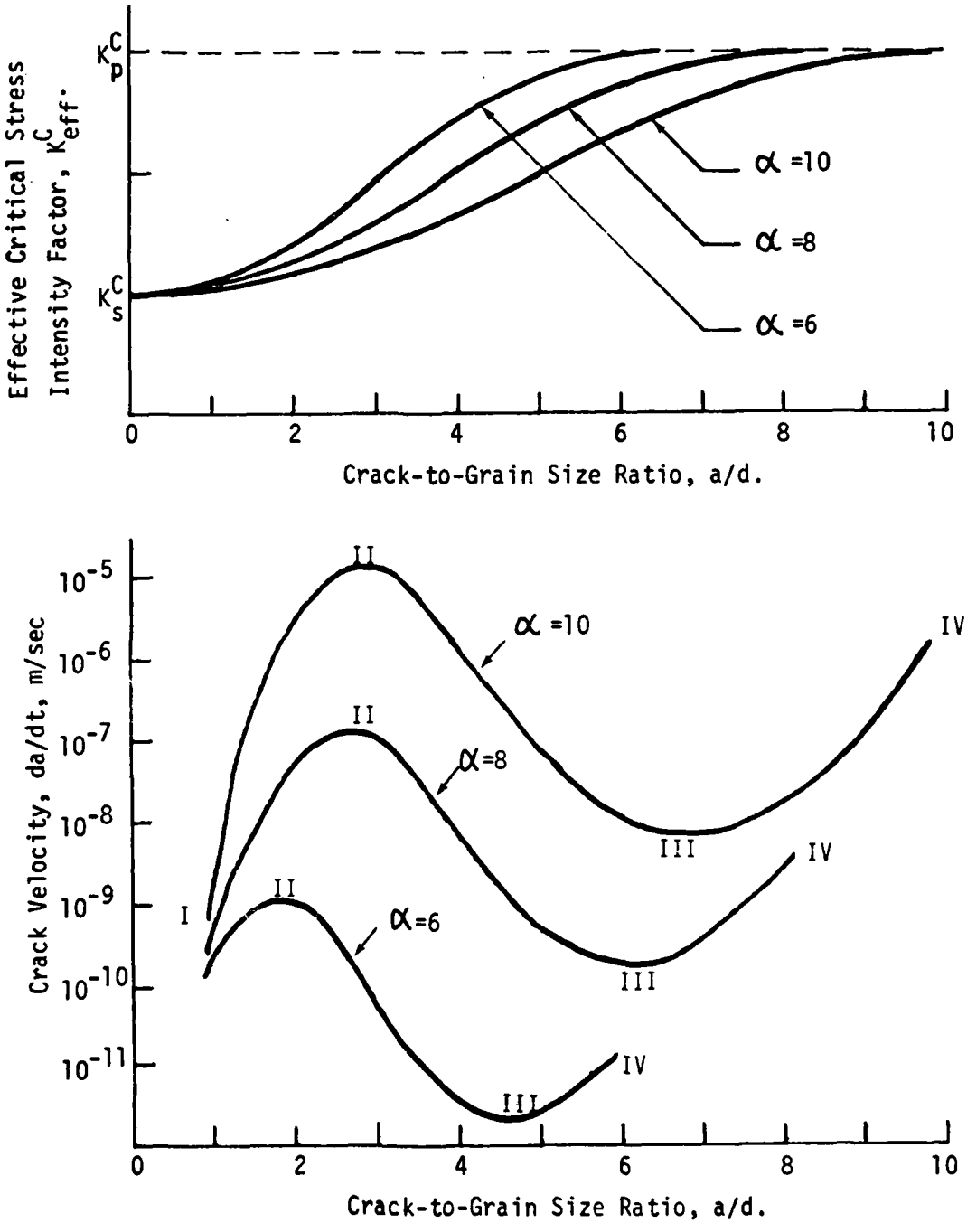

Fig. 5-23 (a) The Effective Critical Stress Intensity Factor As Function of Crack-to-Grain Size Ratio with Various α, (b) The Crack Velocity As Function of a/d and α.

the value of α, and crack velocity has its minimum. Region IV is the macroscopic crack growth region where crack growth is controlled solely by the macroscopic crack growth law. This is the only region to which the conventional approach applies. Notice that the difference between the maximum and the minimum crack velocities is two orders of magnitude. An implication is that subcritical crack growth can readily occur when cracks are microscopic; therefore, the assumption of neglecting subcritical crack growth, generally made in calculating time-to-failure or fracture toughness from an observed flaw size, becomes questionable. Another implication is that there is a stable crack size for a given grain sized material corresponding to Region III where crack velocity is minimum. Therefore, in the strength test (fast fracture) grain sized cracks readily propagate to form stable cracks; the stable cracks subcritically propagate according to the macroscopic crack growth law to become the critical cracks for the fast fracture tests. In the delayed fracture tests, grain sized cracks propagate according to the microscopic crack growth law in Region I and II and slow down in Region III. The cracks slowly propagate to overcome Region III and continue to grow according to the well-established macroscopic crack growth law. If this is true, then the stablized cracks should be observed in delayed fracture test since their sizes are $a = 150$ to $250\ \mu$ for the specimen used in the present study.

In fact, sizes of clusters of grain sized cracks or larger cracks revealed by the fluorescent dye penetrant in Fig. 5-4 are between 350 μ and 480 μ in length. Those values translate to the crack-to-grain size ratio a/d = 5.5 and 7.5, which are close to the crack sizes in Region III in Fig. 5-23 for α = 6 - 10.

The time-to-failure for the case shown in Fig. 5-22 can be calculated by adding the incremental time spent in each growth law as follows:

$$t_f = \sum_{j=1}^{\alpha-1} \int_{K = Y\sigma\sqrt{jd}}^{K = Y\sigma\sqrt{(j+1)d}} (K/v)\,dK + \int_{K = Y\sigma\sqrt{\alpha d}}^{K = Y\sigma\sqrt{a_{cr}}} (K/v)\,dK \qquad (5\text{-}5)$$

where $v = da/dt = B(K/K^C_{eff})^n$

Notice that the first term in eq. (5-5) is the time spent in the microscopic crack growth region and the second term is time spent in the macroscopic region. Equation (5-5) can be written as

$$t_f = \frac{2}{B(n-2)}\left(\frac{K^C_p}{Y\sigma}\right)^n \sum_{j=1}^{\alpha} \{1 - \beta + \beta\cos(\tfrac{j}{\alpha} - 1)\pi\}^n (jd)^{\frac{2-n}{2}} \qquad (5\text{-}6)$$

Figure 5-24 shows the calculated time-to-failure for one and two grain-sized initial cracks with α = 6, 8, and 10. The values used in the calculations are: K^C_p = 5.3 MPa $m^{1/2}$, K^C_s = 1.7 MPa $m^{1/2}$, d = 32 μ, B = 6.74, Y = 1.27, and n = 31.

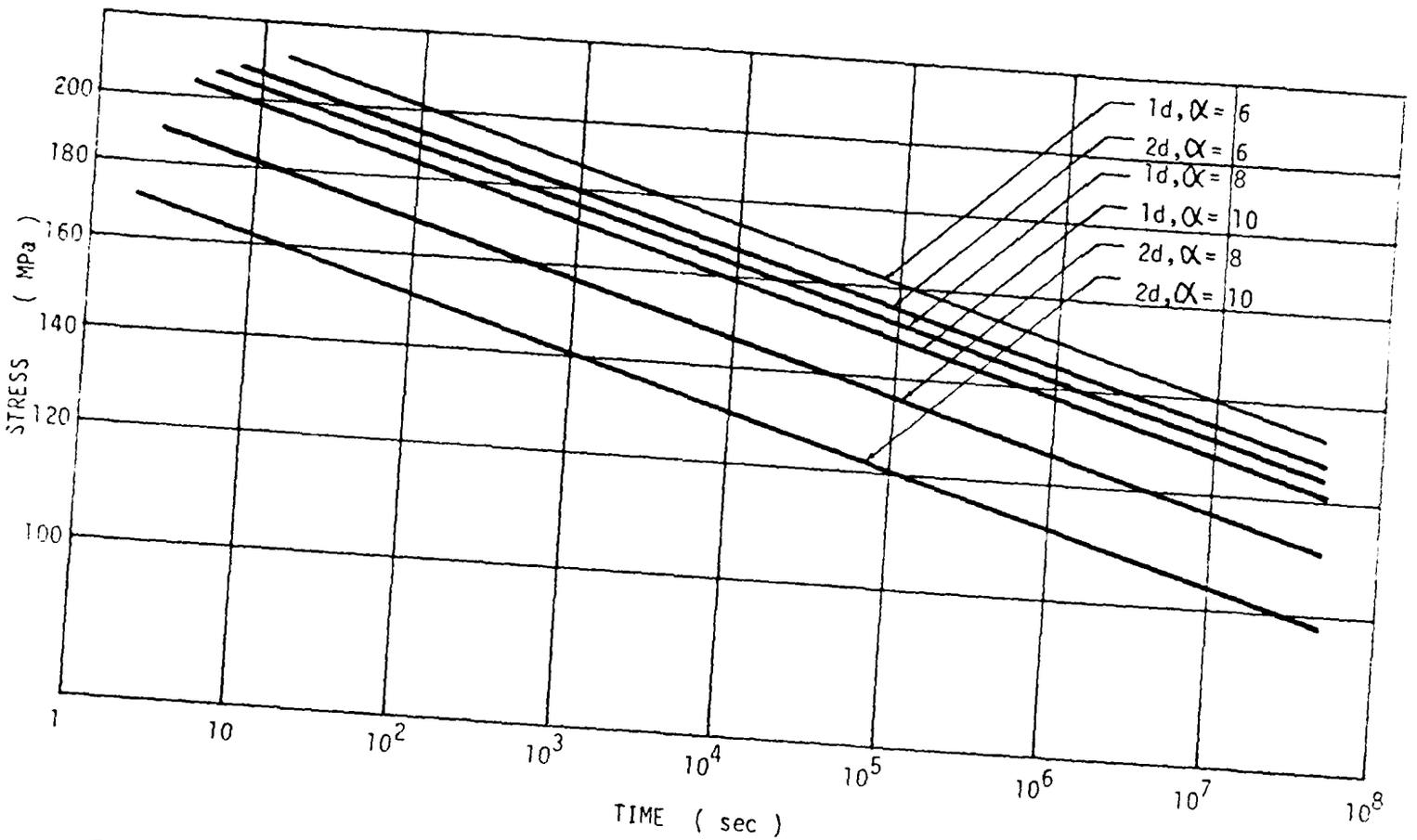

Fig. 5-24 Calculated Time-to-Failure Based Upon The Microscopic Crack Growth Law.

Figure 5-24 illustrates, for example, a two grain-sized crack fails after 2×10^6 sec (23 days) at 120 MPa for $\alpha = 8$. If the conventional approach is used, given in eq. (2-17), the time-to-failure is calculated to be 9.23×10^{17} sec (30 years) for the same crack at the same stress level. The reason why the conventional approach gives such a long time-to-failure is because the initial stress intensity factor for the two grain-sized crack is only 0.86 MPa $m^{1/2}$, and this value is well below the so-called static fatigue threshold. Therefore, the crack growth law had to be excessively extrapolated to calculate the time-to-failure.

Another comparison can be made when the initial crack sizes are compared for the same time-to-failure. If the time-to-failure is 2×10^6 sec, the proposed approach gives the initial crack size of 32 μ; whereas the conventional approach requires 200 μ in order to have the same time-to-failure. No crack of this size was observed in the present study; most inherent flaws were grain-sized and less than 40 μ.

It will be shown later that the calculated time-to-failure based upon the isolated microscopic crack growth law which is proposed here gives good prediction, and can be used as an upper bound for the time-to-failure because the value decreases when the interaction and coalescence of cracks are involved.

2.2 Crack Interaction and Coalescence

It was found from direct observation that the initial stage of slow crack growth involved interaction and coalescence of microscopic inherent flaws and that the predominant mode of cracking was intergranular. The interaction and coalescence of cracks has been analyzed mainly from three points of view: microcrack formation around the crack tip,[81] fracture of a body with a number of cracks present,[46,58] and in metals interaction between a main crack and the nearby slip band.[56] In the present study, since a number of inherent flaws are interacting, the simplest model is "N equal-length collinear cracks in a plate under uniaxial tensile stress field perpendicular to the crack plane" as shown in Fig. 5-25. Crack length is taken as 2a, and the distance between the centers is taken as 2b. Although the actual crack configuration is different, the model is good as far as interaction is concerned.

Meredith and Pratt,[46] from fractographic evidence in a porous alumina, inferred that existing flaws coalesced to form a larger crack prior to fracture. Using a model of an infinite number of collinear cracks, they were able to correlate the stress necessary to coalesce the nearby flaws as shown in Fig. 5-26 with the fracture strength. Singh et al.[58] analyzed the effect of collinear crack interaction on the crack stability and propagation behavior in a brittle material subjected to thermal shock. They showed

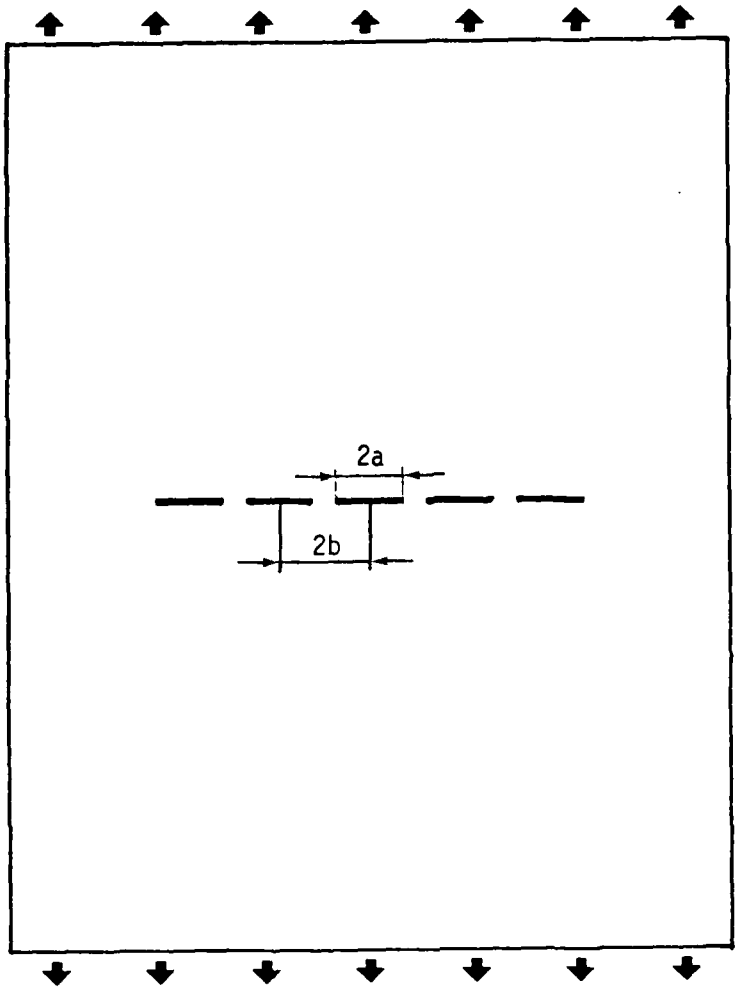

Fig. 5-25 N Equal Length Collinear Cracks In A Plate Under Uniaxial Tension. (five cracks are shown)

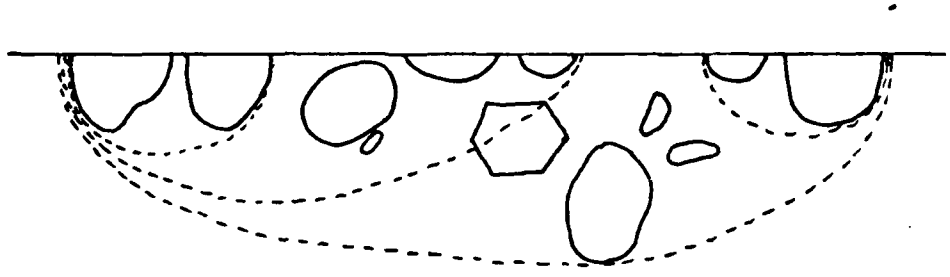

Fig. 5-26 Coalesced Flaws Prior To Failure of Porous Alumina.[46]

that the crack interaction might result in crack coalescence and complete failure.

In this section, the effect of the interaction and coalescence of microscopic cracks on the time-to-failure calculation will be demonstrated using the mathematical model.

The stress intensity factor including interaction term can be given by

$$K = ZY\sigma\sqrt{a} \tag{5-7}$$

where Z = interaction parameter, and a function of a/b

Y = geometrical factor

σ = applied stress

a = crack length

b = distance between the centers of cracks

The interaction parameter Z is a function of a/b as well as number of cracks, N, as indicated in Fig. 5-27.[14] When cracks are located far apart, then Z = 1, indicating no interaction. When N is infinity, the analytical expression for Z is available,[12]

$$Z = \left[\frac{2b}{\pi a} \tan\left(\frac{\pi a}{2b}\right)\right]^{1/2} \tag{5-8}$$

Where N = 2, the interaction parameter can be expressed as

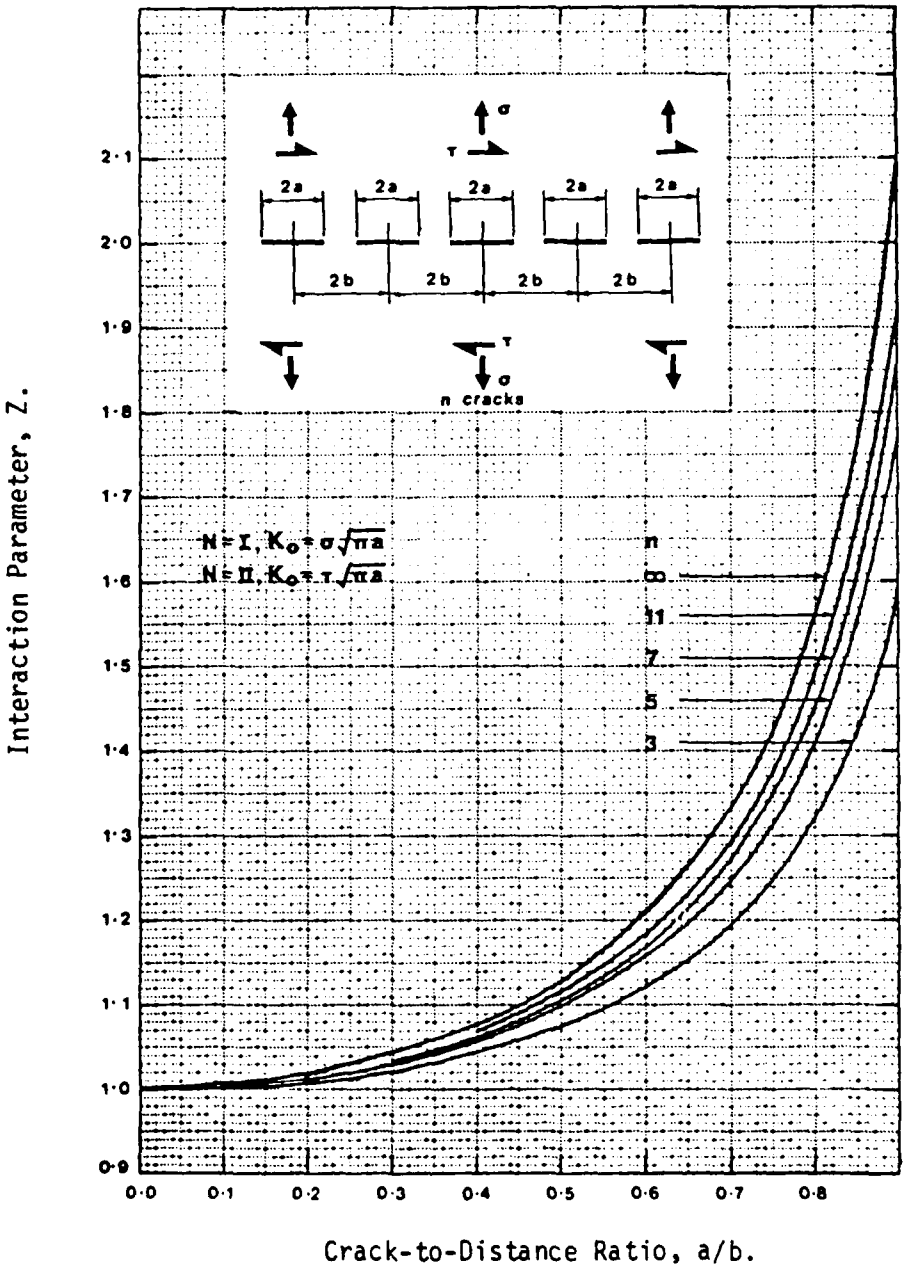

Fig. 5-27 Crack Interaction Parameter for N Equal Length Collinear Cracks.[14]

$$Z_A = \frac{1}{k}\sqrt{\frac{1 + a/b}{\alpha_o a/b}}\left[\frac{E_{(k)}}{K_{(k)}} - \alpha_o^2\right]$$

$$Z_B = \frac{1}{k}\sqrt{\frac{1 + a/b}{a/b}}\left[1 - \frac{E_{(k)}}{K_{(k)}}\right] \qquad (5\text{-}9)$$

where Z_A = interaction parameter for the inner tips of the cracks

Z_B = interaction parameter for the outer tips of the cracks

$\alpha_o = \frac{1 - a/b}{1 + a/b}$

$K_{(k)}$ = the complete elliptic integral of the first kind

$E_{(k)}$ = the complete elliptic integral of the second kind

$k = \sqrt{1 - a^2}$

Equation (5-9) cannot be expressed analytically, but can be evaluated numerically as shown in Appendix B.

Once Z is evaluated, then the stress intensity factor can be calculated by eq. (5-7). Therefore, if the crack growth law is given, time spent in slow crack growth up to dynamic coalescence ("Pop-in") can be calculated accordingly, which may be the time-to-failure in some cases and might be a portion of the time-to-failure in other cases.

The fracture energy of grain-sized cracks emanating from the inherent flaws is controlled by the single-crystal fracture energy, or grain-boundary fracture energy.

Therefore, the single crystal critical stress intensity factor will be used in calculating the time-to-coalescence as illustrated in Fig. 5-28. Since the interaction parameter, Z, increases as cracks grow toward each other, the incremental time had to be calculated.

Assuming that the interaction parameter, Z, is constant over an incremental time period,

$$\begin{cases} \frac{da}{dt} = B\left(\frac{K}{K_s^C}\right)^n \\ K = ZY\sigma\sqrt{a} \end{cases}$$

Thus

$$\Delta t_i = \frac{2}{B(n-2)}\left(\frac{K_s^C}{Y\sigma}\right)^n \left(\frac{1}{Z_{i+\frac{1}{2}}}\right)^{n-2} \left\{\left(\frac{1}{a_i}\right)^{\frac{n-2}{2}} - \left(\frac{1}{a_{i+1}}\right)^{\frac{n-2}{2}}\right\} \tag{5-10}$$

The time-to-coalescence can be obtained by adding the incremental time as follows:

$$t_c = \sum_{i=1}^{m} \frac{2}{B(n-2)}\left(\frac{K_s^C}{Y\sigma}\right)^n \left(\frac{1}{Z_{i+\frac{1}{2}}}\right)^{n-2} \left\{\left(\frac{1}{a_i}\right)^{\frac{n-2}{2}} - \left(\frac{1}{a_{i+1}}\right)^{\frac{n-2}{2}}\right\} \tag{5-11}$$

where $Z_{i+\frac{1}{2}}$ = average interaction parameter in the period

i = i, 2, 3, ... m

Figure 5-29 to Fig. 5-32 show the results of calculated time-to-coalescence from eq. (5-11) for various cases. The

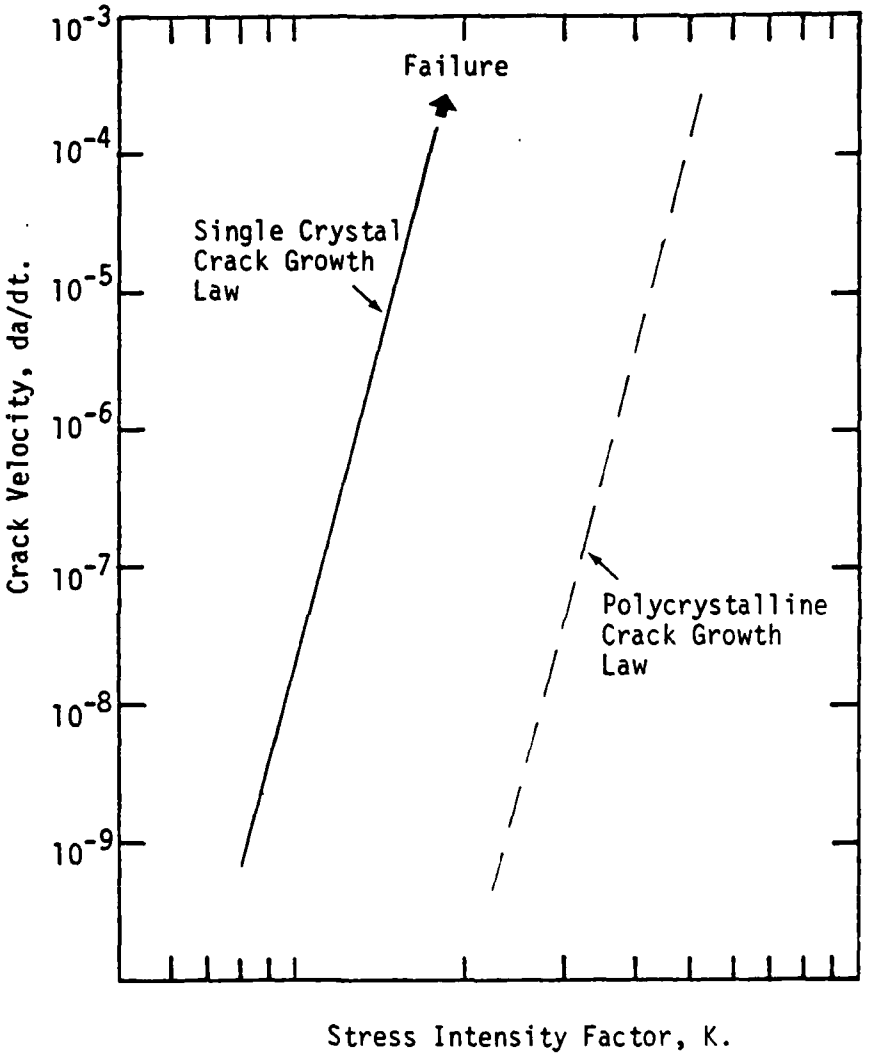

Fig. 5-28 Slow Crack Growth Solely Controlled By The Single Crystal Critical Stress Intensity Factor.

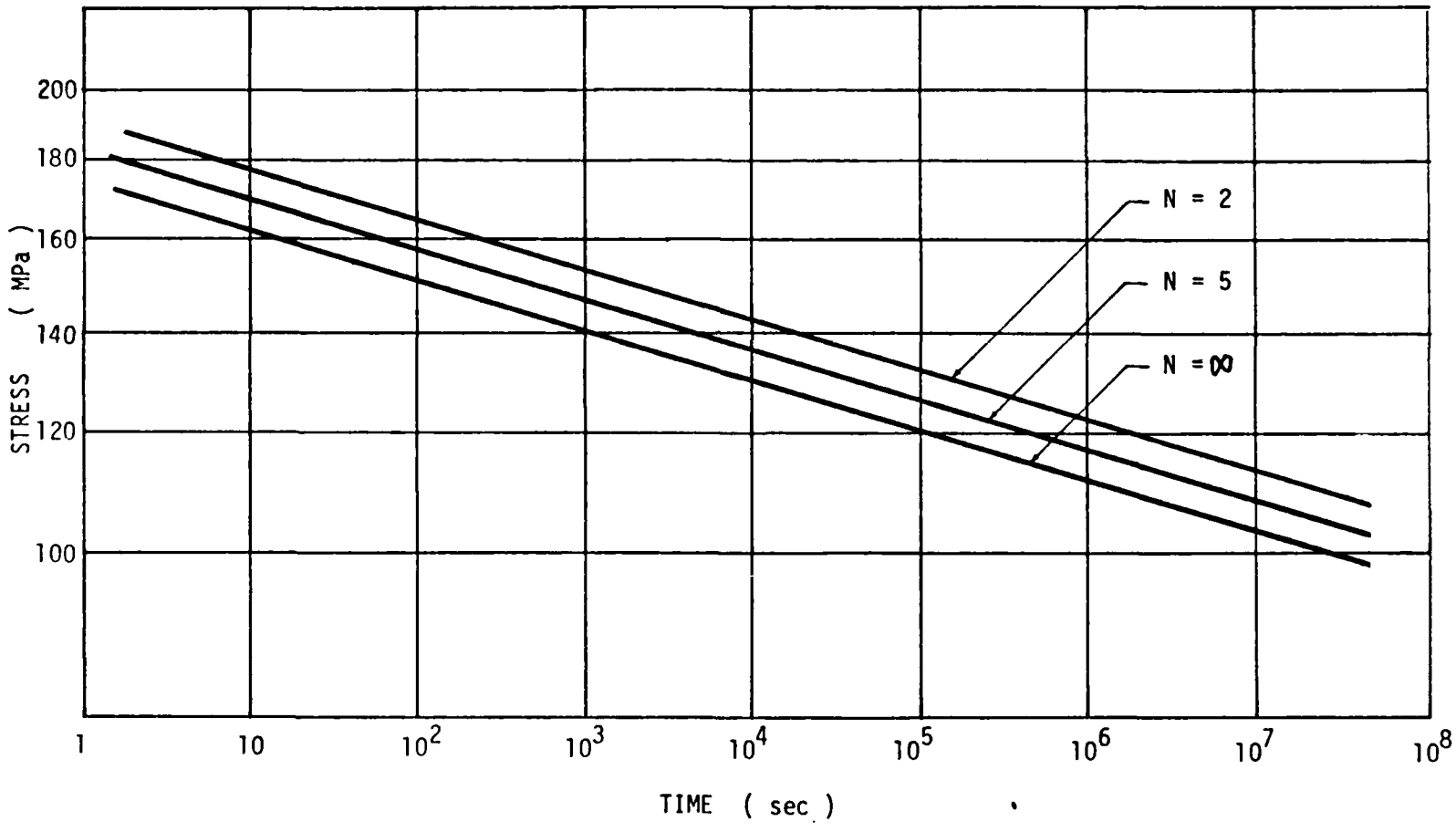

Fig. 5-29 Calculated Time-to-Coalescence for a = 16 μ, a/b = 0.5

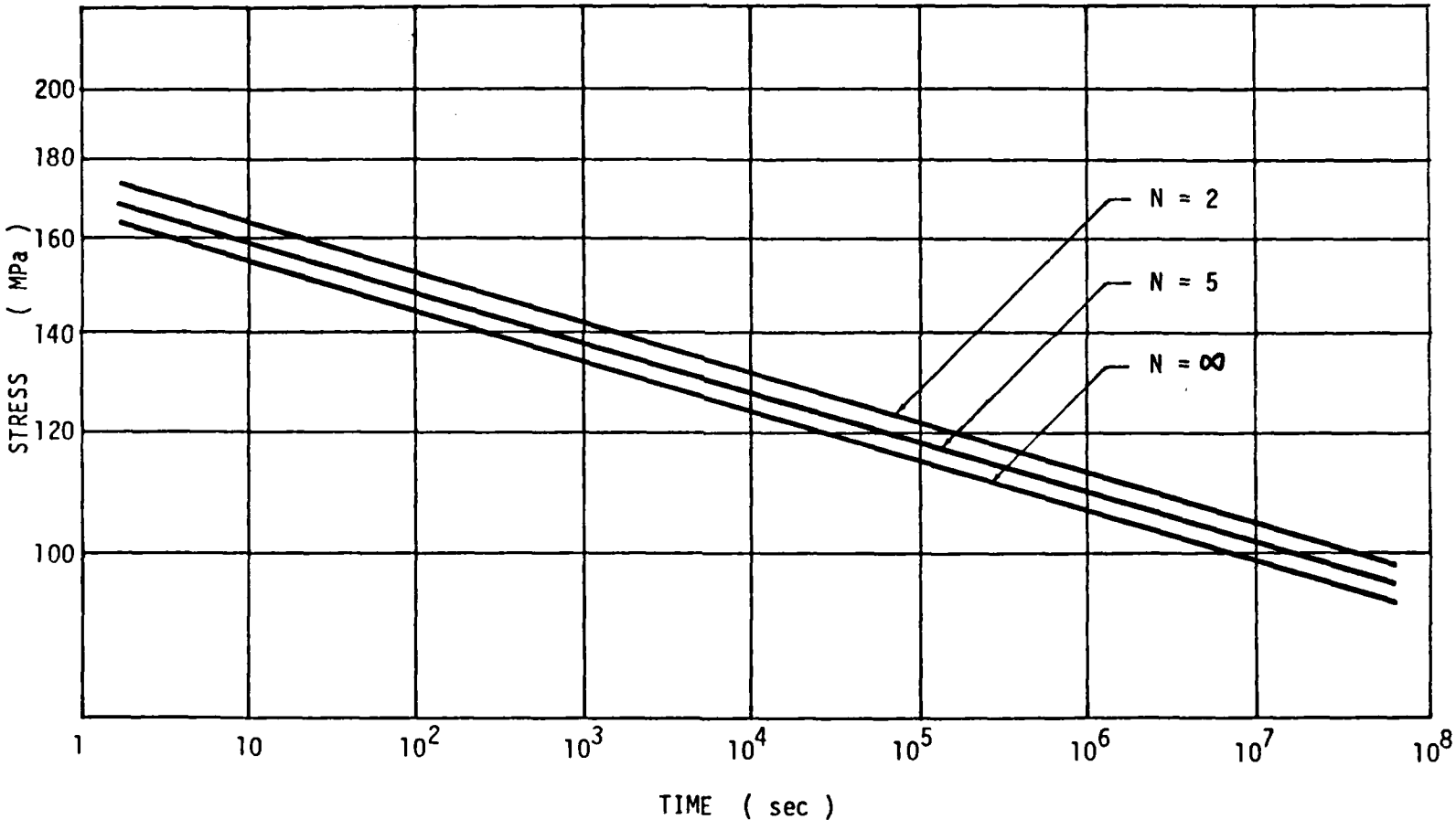

Fig. 5-30 Calculated Time-to-Coalescence for a = 20 μ, a/b = 0.4

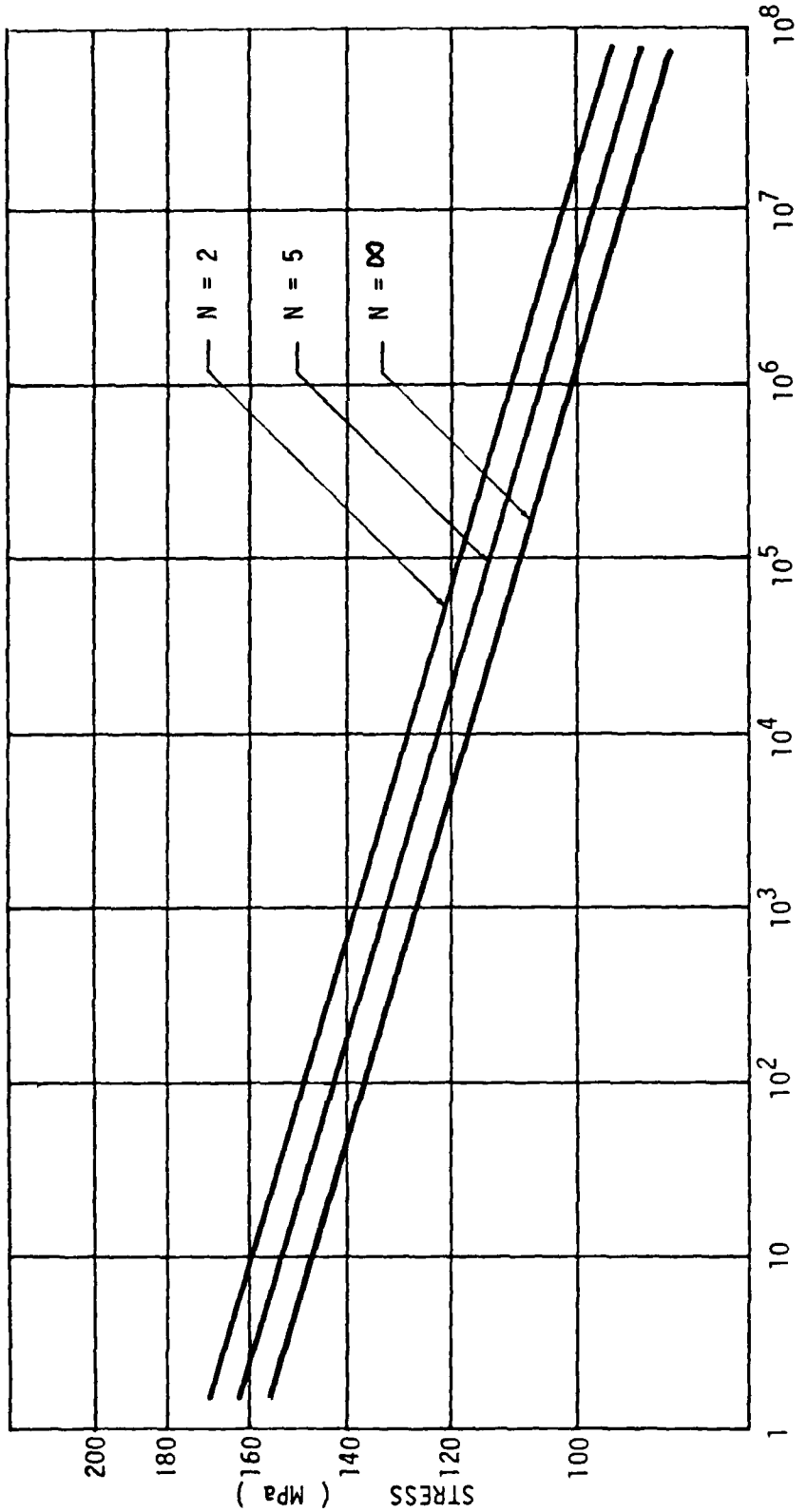

Fig. 5-31 Calculated Time-to-Coalescence for a = 20 μ, a/b = 0.5

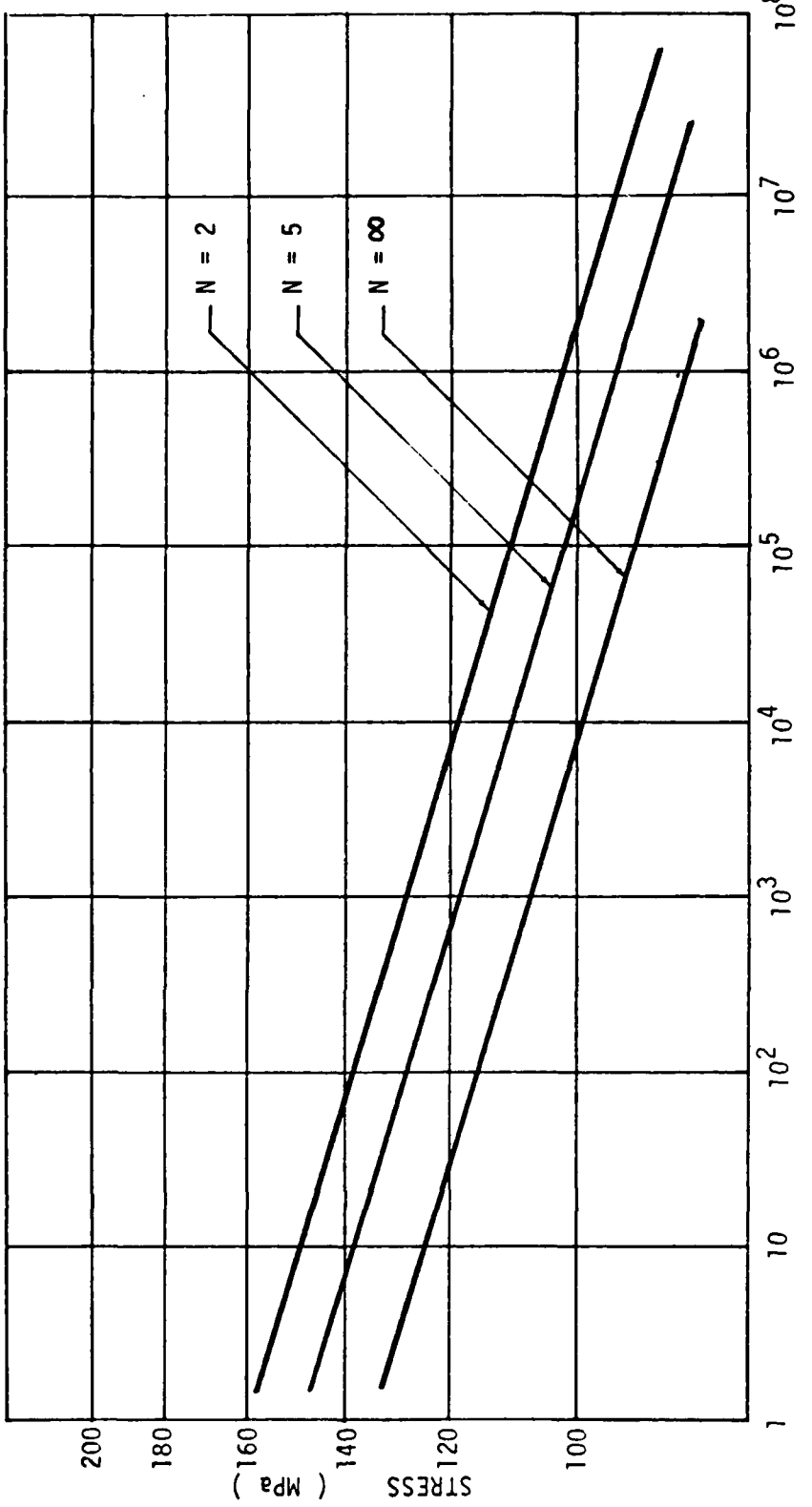

Fig. 5-32 Calculated Time-to-Coalescence for a = 20 μ, a/b = 0.67

calculations were done with N = 2, 5, and ∞. Values of a and b in Fig. 5-29 are 16μ and 32μ respectively, indicating grain-sized cracks with one grain between them. Figure 5-30, Fig. 5-31, and Fig. 5-32 show calculated time-to-coalescence for a = 20 μ with a/b = 0.400, a/b = 0.500, and a/b = 0.667, respectively. Notice that when N is large as soon as the grain-sized cracks coalesce, immediate failure results because the coalesced crack is larger than the critical size. Therefore, the time-to-coalescence is equal to the time-to-failure. On the other hand, if the number of cracks is small, that is the coalesced crack is smaller than the critical size, the coalesced crack will continue to grow according to the microscopic crack growth law proposed in section 2.1.

As the microscopic crack growth law for an isolated crack may serve as an upper bound for the time-to-failure, the time-to-failure based upon the interaction and coalescence of the infinite number of grain-sized cracks may serve as a lower bound. This crack growth behavior is illustrated in Fig. 5-33. The shortest time-to-failure can be obtained from the infinite number of grain-sized cracks interacting and coalescing result in fracture. Notice that the amount of crack growth required for coalescence may be so small that the actual failure-causing crack propagation may never be observed in this case. The longest time-to-failure can be obtained from an isolated grain-sized

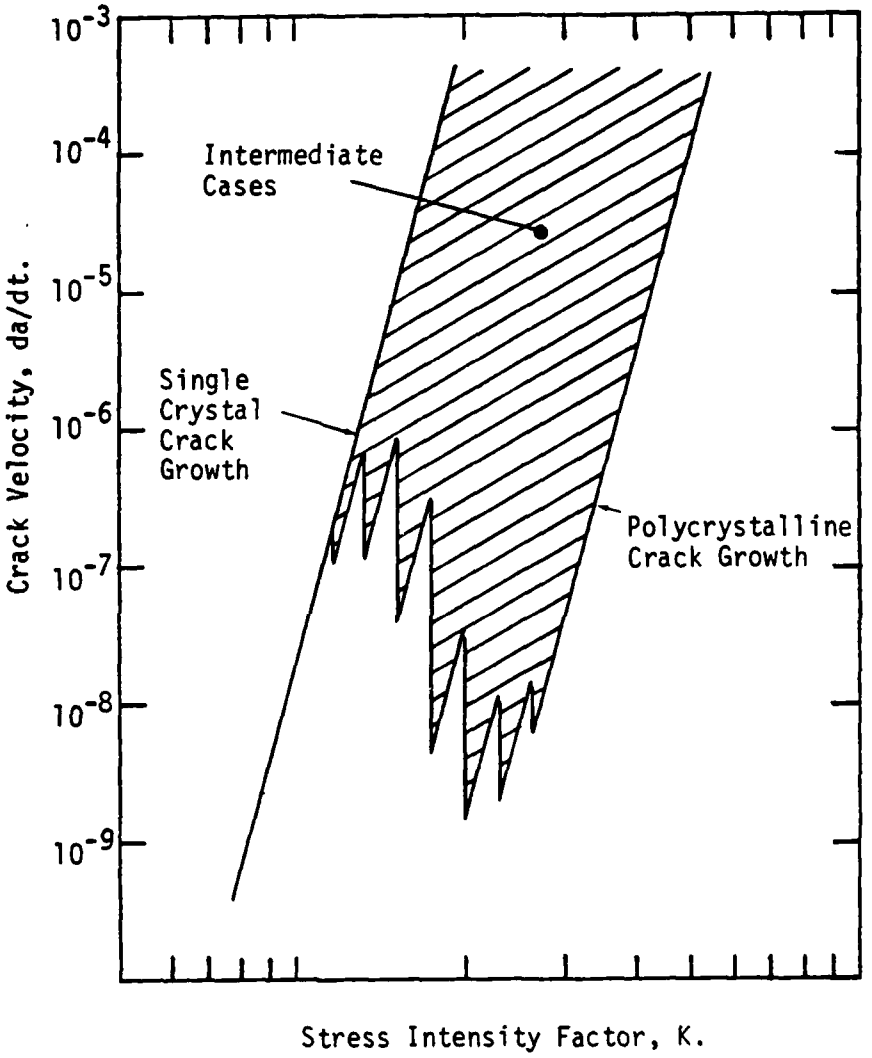

Fig. 5-33 Crack Growth for Various Cases.

crack propagating according to the microscopic crack growth law without interaction. All other cases should fall into the shaded area in Fig. 5-33. For example, when five grain-sized cracks (a = 16 μ, b = 32 μ) coalesced to form a larger crack (a = 144 μ) which has the crack-to-grain size ratio 4.5. The coalesced crack will continue to propagate according to the microscopic crack growth law and eventually according to the macroscopic growth law.

2.3 The Generalized Microscopic Crack Growth Law

The effect of interaction and coalescence of grain-sized cracks on the time-to-failure has been demonstrated in the last section. Now the concept of interaction and coalescence of multiple cracks is combined with the single microscopic crack growth law established in the previous section to construct the generalized microscopic crack growth law.

Important points to be remembered from the previous sections concerning the microscopic crack growth law are:

(1) The local crack velocity is solely controlled by the local effective critical stress intensity factor, K^C_{eff}, as given in eq. (5-1).

(2) The effective critical stress intensity factor has a functional relation with the crack-to-grain size ratio given in eq. (5-2).

(3) Crack velocity for a given applied stress reaches a maximum at about crack size four to six times the grain size.

(4) The interaction and coalescence of multiple cracks have significant effect on the time-to-failure.

Combining eq. (5-2) and eq. (5-11), the general expression of the time-to-failure for the microscopic crack growth with interaction and coalescence of multiple cracks can be given

$$\begin{cases} t_f = \sum_{i=1}^{m} \frac{2}{B(n-2)} \left(\frac{K^C_{eff}}{Y\sigma}\right)^n \left(\frac{1}{Z_{i+\frac{1}{2}}}\right)^{n-2} \left\{ \left(\frac{1}{a_i}\right)^{\frac{n-2}{2}} - \left(\frac{1}{a_{i+1}}\right)^{\frac{n-2}{2}} \right\} \\ K^C_{eff} = \begin{cases} K^C_p \{1 - \beta + \beta \cos(\frac{a}{d\alpha} - 1)\pi\} & \frac{a}{d\alpha} < 1 \\ K^C_p & \frac{a}{d\alpha} > 1 \end{cases} \end{cases} \quad (5\text{-}12)$$

where $\beta = \frac{1}{2}(1 - \frac{K^C_s}{K^C_p})$

α = a critical value of a/d above which $K^C_{eff} = K^C_p$

K^C_p = polycrystalline critical stress intensity factor

K^C_s = single crystal critical stress intensity factor

a = one-half crack length

d = grain diameter

Equation (5-12) allows calculation of the time-to-failure for a variety of crack configurations. For example, a realistic model of crack configuration of the alumina used in the present study may be "three collinear grain-sized cracks (a = 20 μ, a/b = 0.5)" as shown in Fig. 5-34(a). Time necessary to coalesce the cracks is calculated from eq. (5-12) to be 7.29×10^4 sec for σ = 120 MPa. This resultant crack (a = 100 μ) grows accorsing to the microscopic crack growth law. Time-to-failure for this resultant crack is

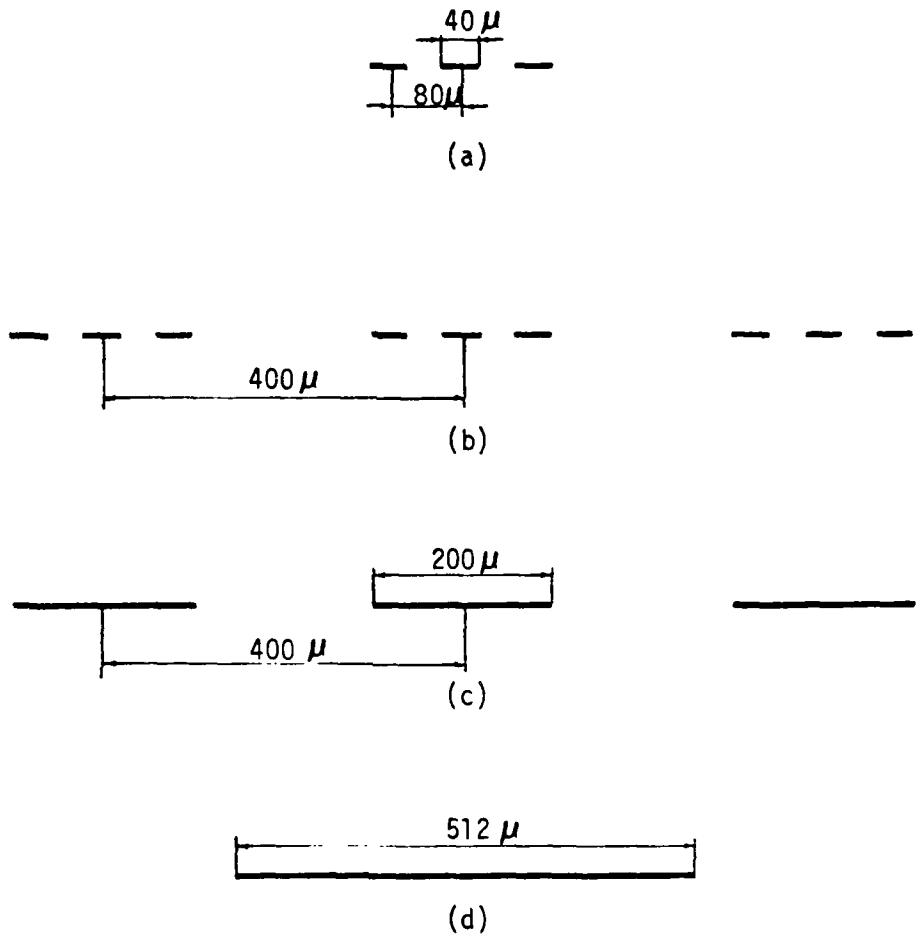

Fig. 5-34 Possible Models of Assemblies of Cracks.

Notice that the time-to-failure for (b) and (d) are the same.

calculated to be 5.74×10^4 sec. Therefore, the total time-to-failure is 1.30×10^5 sec.

A striking phenomenon is observed when there are other sets of small cracks close together as shown in Fig. 5-34(b). In this case, the time required to coalesce the three small cracks is the same as before; however, as soon as the small cracks coalesced to become three larger cracks as shown in Fig. 5-34(c), the specimen fails catastrophically. It is because the crack velocity of the coalesced cracks (a = 100 μ) is in Region II of very high velocity which is even more enhanced by the interaction with the other coalesced cracks. Therefore, it takes only 3.94 sec to failure. The equivalent size of a single crack, which gives the same time-to-failure under the same applied stress, obtained from the conventional approach is a = 256 μ as shown in Fig. 5-34(d). It should be noted that no crack of a = 256 μ was observed as an initial crack in the present study. The observed initial flaw sizes were all microscopic, a = 20 μ to 40 μ. It has been demonstrated that a ceramic specimen can fail from this microscopic crack growth with the interaction and coalescence of multiple microscopic cracks in a short time. If this is a failure mechanism in delayed fracture of polycrystalline ceramics, non-destructive testing may not be able to reveal the existence of crack propagation because the amount of subcritical crack growth from the individual inherent flaws is very small before the crack coalescence.

Now that the microscopic crack growth law with interaction and coalescence of cracks has been developed, the experimental data and the predicted values are compared.

The time-to-failure observed in the present experiment are plotted in Fig. 5-35. Also plotted are the time-to-failure based upon the microscopic crack growth law with a single grain-sized crack ($a = 16\ \mu$, $\alpha = 10$) and based upon the interaction and coalescence of multiple microscopic cracks ($a = 20\ \mu$, $a/b = 0.5$, $N = \infty$). As can be seen the experimental results almost fall within the upper and the lower bounds of curves. The times-to-failure of the assembly of cracks shown in Fig. 5-34(b) also falls within the curves.

To illustrate how the conventional approach with a simplistic assumption of the single macroscopic crack differs from the proposed approach, calculated times-to-failure using the conventional approach are plotted in Fig. 5-36 with various assumed initial crack sizes along with the same experimental results shown in Fig. 5-35. In order to have reasonable values of time-to-failure, the initial crack size must be larger than $a = 200\ \mu$. As mentioned earlier, no crack of that size was observed as an initial crack in the present study.

Therefore, it has been confirmed that the proposed microscopic crack growth law gives much better prediction than the conventional approach.

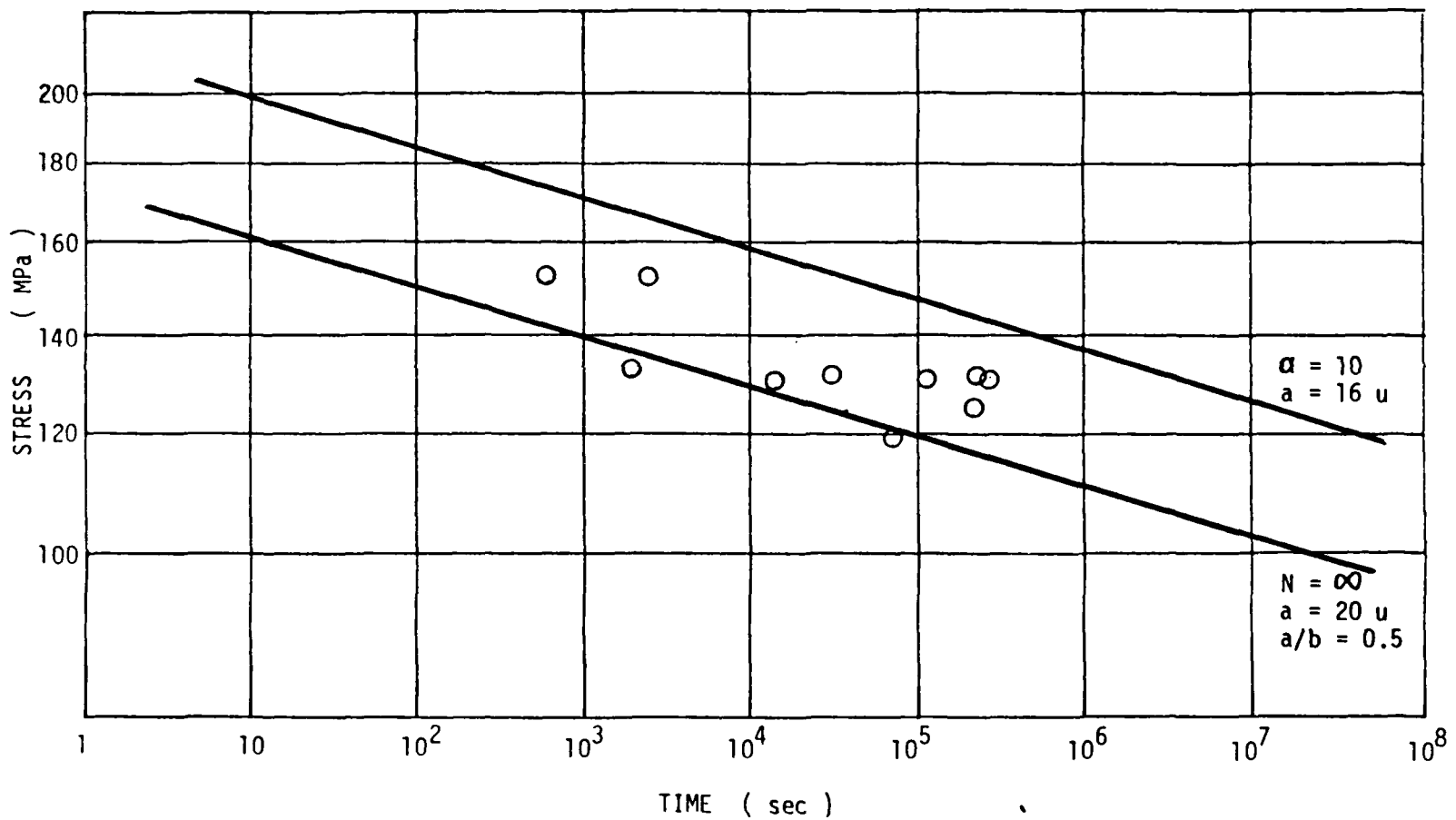

Fig. 5-35 Calculated Time-to-Failure Based Upon The Proposed Microscopic Crack Growth Law and Experimental Data.

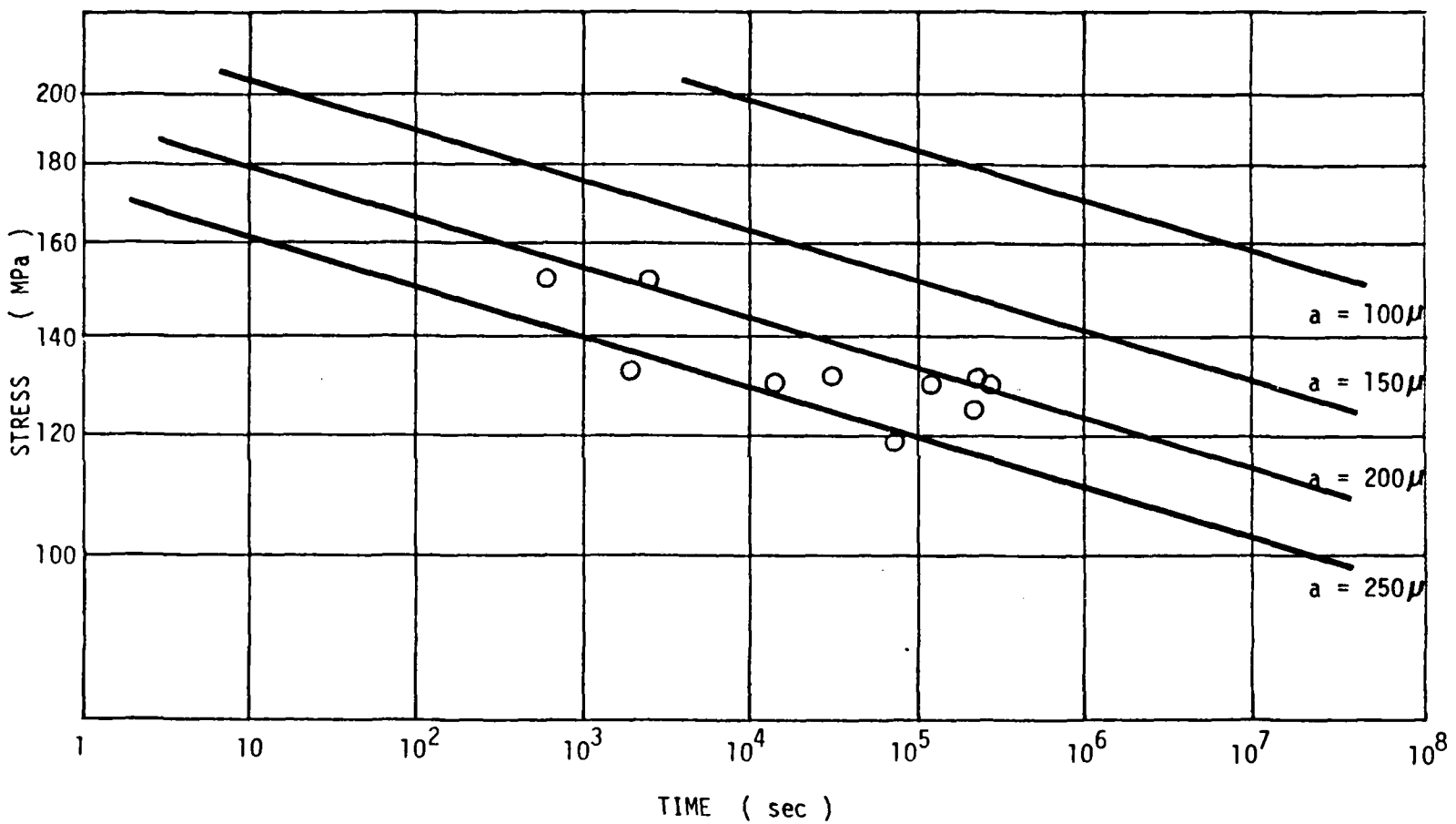

Fig. 5-36 Calculated Time-to-Failure Based Upon The Conventional Approach and Experimental Data.

Before leaving this section, the following important points should be recognized:

(1) A surface of a ceramic contains a larger number of inherent flaws which, either by themselves or as assemblies, become potential sites for crack origins. In delayed fracture crack origins can be multiple.

(2) Microscopic cracks grow rapidly in the very early stage, Region II, of delayed fracture and slow down as they approach macroscopic size, in Region III.

(3) Crack initiation and propagation usually involve interaction and coalescence of nearby flaws.

(4) A specimen can fail without having a single worst crack when there are many microscopic cracks close together.

(5) The coalescence of the microscopic cracks may occur in a very short time without being revealed by non-destructive testing because an amount of subcritical crack growth from the individual inherent flaws can be very small before the coalescence.

(6) The isolated microscopic crack growth law provides the upper bound, and the analysis based upon interacting microscopic cracks provides the lower bound in calculation of the time-to-failure.

3. Applicability of Existing Time-to-Failure and Proof Testing Concepts

It has been demonstrated in section 2.1 and 2.2 that the proposed slow crack growth law should be applied when the initial crack is microscopic or the interaction of multiple cracks exists. The conventional approach is to extrapolate the macroscopic crack growth law to calculate time-to-failure. The extrapolated portion of the growth law is well below the threshold value for static fatigue crack growth of polycrystalline ceramics. This is illustrated in Fig. 5-37. Notice that the extrapolated initial crack velocity is unrealistically slow. When the proposed growth law is used, crack velocity in the initial stage becomes substantially higher. Therefore, calculated time-to-failure from the proposed growth law is shorter than that from the conventional approach. Consequently, the conventional approach gives a non-conservative prediction; however, this non-conservative prediction is partially or sometimes excessively compensated by conservative estimation of the initial crack size. But there is no guarantee that the predictions will always come out conservative.

Therefore, it is necessary to reexamine applicability of the existing time-to-failure and proof testing concepts, in order to predict time-to-failure more accurately. In this section, applicability is studied for two cases: (1) when a single microscopic crack is assumed and (2) when the

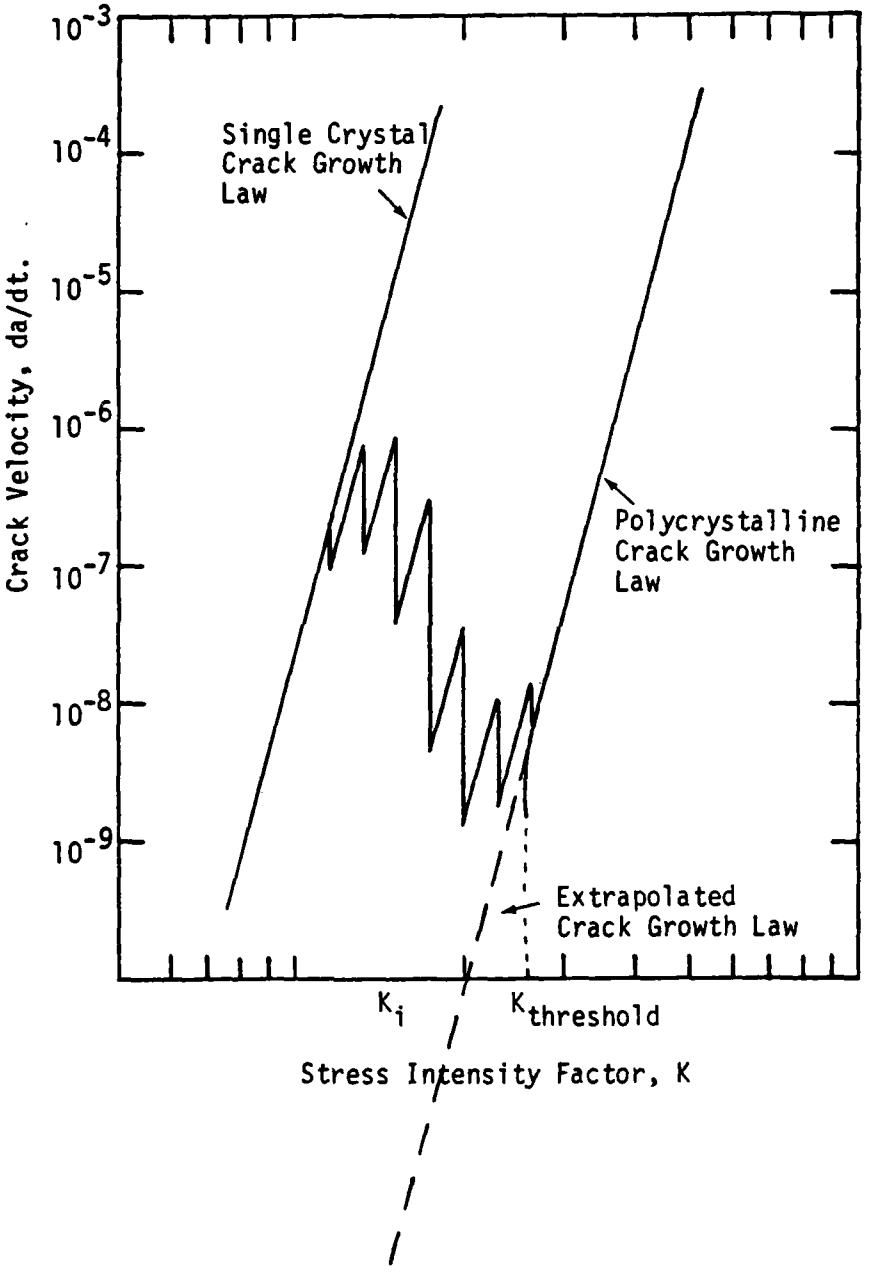

Fig. 5-37 Extrapolated Crack Growth Law In The Conventional Approach.

interaction and coalescence of multiple cracks are assumed.

(1) When a Single Microscopic Crack is Assumed

It was indicated in section 2.1 that the rapid change in local crack velocities between Region II and Region III might give rise to the "stable crack size" for a given grain-sized material, and that the critical crack size for the fast fracture tests might have a dimension close to the crack size corresponding to Region III in Fig. 5-23. This can be verified in the following example:

The average tensile strength of Aℓ-300 is 191.7 MPa when measured with the constant stress rate of 20 MPa/sec. The critical crack size for fracture can be calculated from eq. (2-10) to be a = 474 μ. If these values are used to calculate the initial strength in the absence of subcritical crack growth from eq. (2-20), the initial strength is 279 MPa. The critical crack size which gives the strength 279 MPa is a = 224 μ. This crack size translates to the crack-to-grain size ratio of a/d = 7, which corresponds to the crack size in Region III for α = 8 to 10.

The above example confirms validity of the concept of "stable crack size" for a given grain-sized material.

If the initial crack size exceeds the stable crack size, the time-to-failure can be calculated solely from the existing approach, provided that the interaction of the macroscopic cracks can be neglected. This condition may be satisfied when the applied stress level is sufficiently

high, for example, 90% of the fracture strength. Because subcritical crack growth in Region II in Fig. 5-23 is significantly rapid, the stable crack size may readily be reached as the specimen is loaded. In this case, the existing time-to-failure concept applies, and it can be calculated from the macroscopic crack growth law as proven by Soma et al.[52] They showed that the calculated time-to-failure combined with the concept of the statistical initial crack distribution gave good prediction when the applied stresses were larger than 85% of the fracture strength. The initial crack size is obtained by calculating the amount of subcritical crack growth prior to fracture under a constant stress rate experiment.[40] An error can be introduced in the calculation due to simple extrapolation of the macroscopic crack growth law into microscopic crack growth region. The extrapolated crack size is much larger than the actual size which leads to a conservative estimation of the initial crack size as shown in Fig. 5-38.

As mentioned earlier, this overestimation of the initial crack size may compensate for the non-conservative prediction of the initial crack velocity. If the same example is used, the estimated initial crack size is a = 224 μ. The time-to-failure for this crack using the conventional approach is 5×10^5 sec for σ = 120 MPa as shown in Fig. 5-36. On the other hand, the actual initial crack size may be two grain-sized. The time-to-failure for the

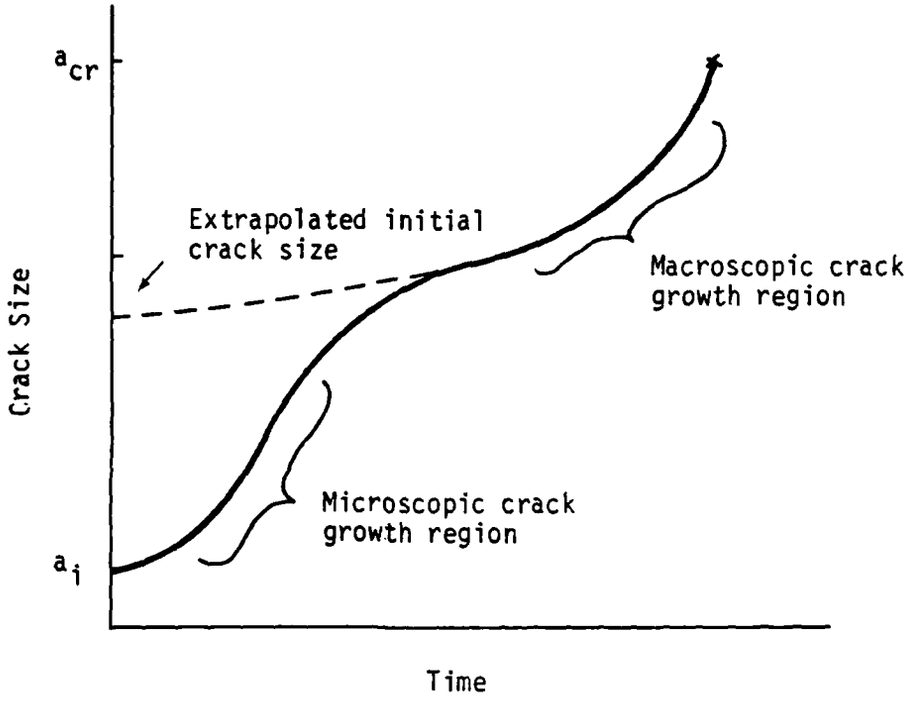

Fig. 5-38 Extrapolated Initial Crack Size In The Conventional Approach.

two grain-sized crack is 2.5×10^6 sec for $\alpha = 8$ and $\sigma = 120$ MPa as shown in Fig. 5-24. This is an example in which the conservative estimation of the initial crack size over-compensated for the non-conservative prediction of crack velocity. However, if $\alpha = 10$ is assumed, the calculated time-to-failure for $\sigma = 120$ MPa is 1×10^5 sec, which is shorter than the predicted value from the conventional approach. Therefore, it can be suggested that when the applied stress is small, the time-to-failure should be calculated from the proposed crack growth law.

A similar argument applies to proof testing. It is applicable when the proof stress level is sufficiently high so that a microscopic crack propagates subcritically to become a macroscopic crack during the proof stressing. However, when the proof stress is small, the conventional approach makes the same two errors: conservative estimation of the initial crack size and non-conservative estimation of crack velocity. Therefore, the conventional approach may not apply.

(2) When the Interation and Coalescence of Cracks is Assumed

As shown previously, when the initial crack size is macroscopic, or when it becomes macroscopic upon loading, the conventional approach may apply. Such conditions are satisfied when the applied stress or the proof stress is sufficiently large so that nearby flaws interact and

coalesce to form a macroscopic crack, provided that the interaction with other macroscopic crack is neglected. However, when there are multiple macroscopic or microscopic cracks close together, the conventional approach fials to predict the time-to-failure. This is illustrated in the following example:

Proof testing is used to estimate the initial crack size. The maximum possible crack size after the proof testing can be given

$$a_i = (K^C_{eff}/Z\,Y\,\sigma_p)^2 \qquad (5\text{-}13)$$

where K^C_{eff} = the effective critical stress intensity factor

Z = interaction parameter

Y = geometrical factor

σ_p = the proof stress

When the conventional approach is used, that is when a single macroscopic crack is assumed, the maximum possible crack size after a proof stress of 191 MPa for example, is calculated to be a = 477 μ from eq. (5-13) as shown in Fig. 5-39(a). This estimated crack size is unreasonably large, and cracks of this size have never been observed in the present study. Nevertheless the crack of the estimated size is supposed to propagate according to the macroscopic

(a)

a = 477 μ, a/b = 0.000, N = 1, K^C_{eff} = 5.30, Z = 1.000

(b)

a = 95 μ, a/b = 0.300, N = 5, K^C_{eff} = 2.43, Z = 1.030

(c)

a = 40 μ, a/b = 0.575, N = , K^C_{eff} = 1.84, Z = 1.200

(d)

a = 40 μ, a/b = 0.701, N = 3, K^C_{eff} = 1.84, Z = 1.200

(a =154 μ, a/b = 0.600, N = 5, K^C_{eff} = 3.39, Z = 1.160)

Fig. 5-39 Maximum Possible Assemblies of Cracks After The Proof Test (σ_p = 191 MPa)

crack growth law until it reaches the critical size. The critical size for a given applied stress can be given as

$$a_{cr} = (K^C_{eff}/Z\,Y\sigma)^2 \qquad (5\text{-}14)$$

where σ = the applied stress

Time-to-failure after the proof test can be calculated from

$$t_f = \frac{2K^{C^2}_{eff}}{Y^2\sigma^2 B(n-2)}\left(\frac{\sigma_p}{\sigma}\right)^{n-2} \qquad (5\text{-}15)$$

For the operating stress level of 90 MPa, the calculated time-to-failure is 6.60×10^4 sec.

If the same concept is applied to the proposed microscopic crack growth law, many combinations of cracks can be thought of as the maximum possible crack. Three different assemblies of cracks were considered here as shown in Fig. 5-39(b), (c) and (d). Crack size, a, crack-to-distance ratio, a/b, number of cracks, N, effective critical stress intensity factor for the crack size with a = 10, K^C_{eff}, and interaction parameter, Z for the assemblies of cracks shown in Fig. 5-39(a), (b), (c), and (d) are summarized in Table 5-2. Notice that the assembly of cracks shown in Fig. 5-39(d) may be the most realistic model.

Calculated times-to-failure are shown in Table 5-3. Although the time-to-failure for (b) is larger than that for (a), the single crack, the time-to-failure for (c) and

AD-A113 012 CALIFORNIA UNIV LOS ANGELES DEPT OF MATERIALS SCIEN--ETC F/G 11/6
IDENTIFICATION OF FLAWS RESPONSIBLE FOR CRACK INITIATION AND MI--ETC(U)
FEB 82 G SINES, T OKADA AFOSR-77-3425

UNCLASSIFIED AFOSR-TR-82-0225 NL

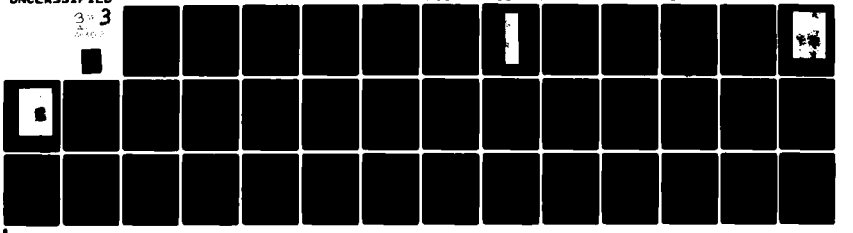

END
DATE FILMED
5-82
DTIC

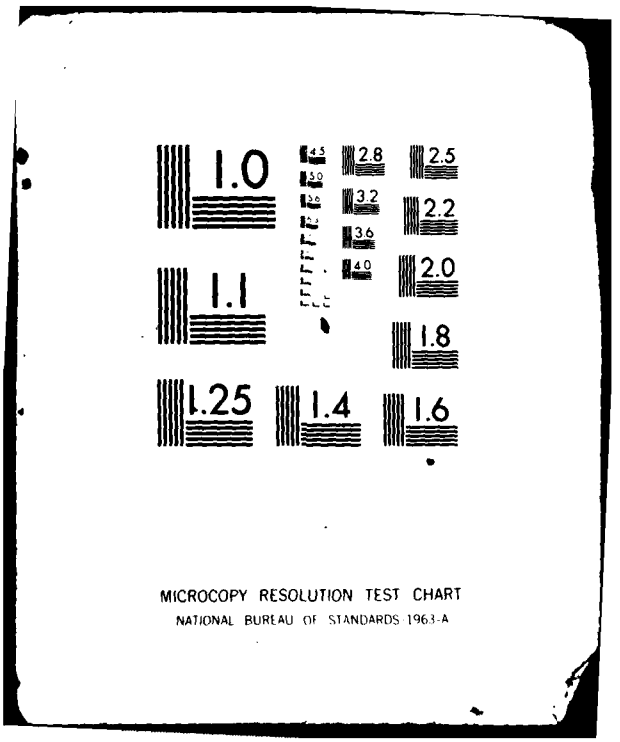
1.0
1.1
1.25
1.4
1.6
1.8
2.0
2.2
2.5
2.8
3.2
3.6
4.0
4.5
5.0
MICROCOPY RESOLUTION TEST CHART
NATIONAL BUREAU OF STANDARDS 1963-A

Table 5-2. The Maximum Possible Assemblies of Cracks After The Proof Test (σ_p=191 MPa)

	(a)	(b)	(c)	(d)
a (μ)	477	95	40	40 (154)
a/b	0.000	0.300	0.575	0.701 (0.600)
N	1	5		3 (5)
K^C_{eff} (MPam$^{1/2}$)	5.30	2.43	1.84	1.84 (3.39)
Z	1.000	1.030	1.200	1.200 (1.160)

Table 5-3. Times-to-Failure After The Proof Test.(sec) (σ_p=191 MPa)

(a)	(b)	(c)	(d)
$6.64X10^4$	$1.07X10^6$	$4.82X10^3$	$4.94X10^3$

(d) are an order of magnitude shorter than that for (a).

It has been clearly demonstrated that an assembly of small cracks, which may not be readily observable due to their smallness, can be very dangerous in delayed fracture; microstructural anisotropies and the interaction and coalescence of cracks are combined to result in much shorter time-to-failure.

Although the non-conservative prediction in time-to-failure might be compensated by overestimation of the initial crack size in some cases, there is no guarantee that the compensated prediction is always conservative. In order to ensure an accurate prediction in time-to-failure, better understanding of physical phenomena in the microscopic dimensions is important, especially when delayed fracture is involved. The proposed microscopic crack growth law may contribute to deeper understanding and better prediction in time-to-failure.

4. Comments on Improving Slow Crack Growth Resistance

It is generally accepted that fracture toughness must be increased in order to improve resistance to slow crack growth and fracture. Attempts have been made to increase fracture toughness by phase transformation[82] and circumferential microcracking.[83] In addition to the above mentioned toughening mechanisms, the following points have been found important in the present study:

(1) a critical value in crack-to-grain size ratio, α, above which the crack behaves as a macroscopic crack, must be small for a material of a given grain size as demonstrated in Fig. 5-23,

(2) a number of flaws interacting, N, should be small, and

(3) a ratio between crack size and their spacing, a/b, should be small.

The first may be achieved by selecting a material which has a greater probability of having cleavage planes of high fracture energy as pointed out by Rice et al.[49] In other words, a functional relationship between single crystal fracture energy and crystal orientation should look like one shown in Fig. 5-40 in order to have more resistance to slow crack growth. The second and third may be satisfied through a better processing exercise. The final product should have uniform distribution of flaws throughout the material, as well as high density, because the local

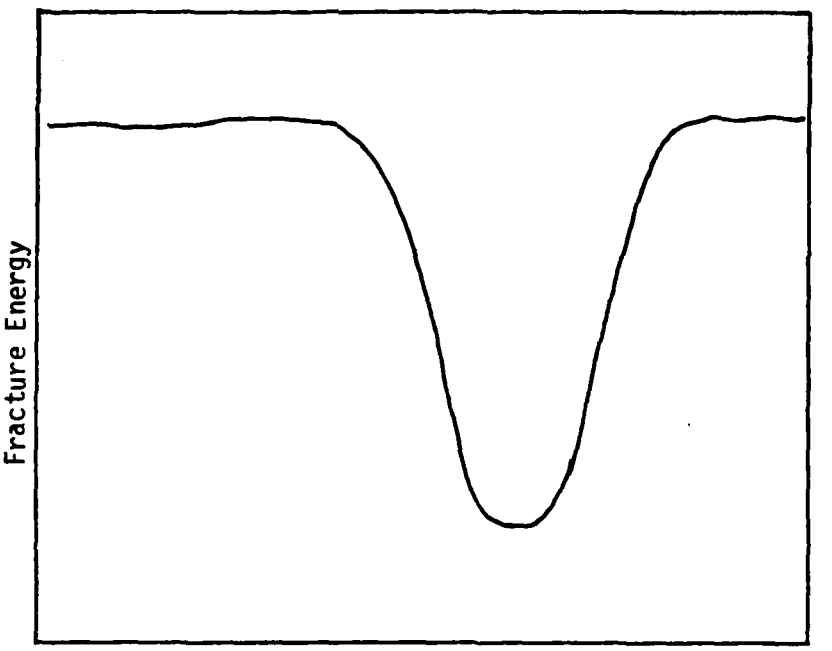

Fig. 5-40 Single Crystal Fracture Energy as a Function of Crystal Orientation for The Improved Crack Growth Resistance.

conglomeration of flaws tends to create unfavorable flaw interaction which leads to premature failure. The uniform microstructural flaw distribution may best be obtained through a new processing technique, "Colloidal/Filtration Consolidation", proposed by Aksay and Lange.[84]

5. *Mode of Fracture:* Whether Intergranular of Transgranular

Since it was found that a crack origin primarily consists of coalesced inherent flaws along grain boundaries, the crack origin area should have a high percentage of intergranular failure on a fracture surface. Also it is known that aluminas exhibit some transgranular cracking when the crack travels fast at room temperature. Therefore, it was of interest to examine the fracture surfaces to study differences in percent of intergranular failure between the crack origin and the rest of the fracture surface.

Specimens which had cracked transversely all the way across, as well as specimens tested in three- and four-point bending in the preliminary tests, were reexamined with the fracture surface exposed. The scanning electron microscopy was used to study the fracture surface. Since most of the crack origins were revealed previously by the fluorescent dye penetrant, the scanning electron micrographs were compared with the optical micrographs with the dye in order to ensure the location of the true origins.

The fracture surfaces were carefully examined with scanning electron microscope, and an example is shown in Fig. 5-41. Notice that there is a morphological transition from high percentage of intergranular failure to low percentage of intergranular failure. The former corresponds to the crack origin area revealed by the dye penetrant,

Fig. 5-41 Scanning Electron Micrograph Showing The Morphological Transition From High Percent-Intergranular-Failure To Low Percent-Intergranular-Failure.

and the latter corresponds to the region of fast fracture. This phenomenon is rather common to many other polycrystalline ceramics as reported elsewhere.[86-90]. It is reasonable to see such morphological transitions from an energy point of view: When crack growth is slow, the kinetic energy is small, therefore, the tortuous crack path might be favorable if the grain boundary has lower fracture energy than the crystal. When crack growth is rapid, the kinetic energy becomes large so that the transgranular cracking becomes favorable. However, it should be noted that the morphological transition shown in Fig. 5-41 was less pronounced in most cases and that the aid of the fluorescent dye penetrant was necessary to locate the real origins in the present study.

6. Slow Crack Growth in Compression

It has been well known that the compressive strength of a ceramic material is generally much higher than the tensile strength.[91] Some theories of fracture in compression have been proposed since Griffith published his second paper in 1924.[15,16,92-94] Although the theories predict the ratio of compressive to tensile strength being three to ten as shown in Fig. 5-42, the actual compressive strength can be 18 times the tensile strength as reported by Adams.[92] This is because the established criteria are damage criteria, not necessarily fracture criteria. Cracks start to emanate from inherent flaws at an applied stress level of three to ten times the tensile strength; however, the cracks do not propagate catastrophically. It requires further stress to grow the cracks. The extent of damage induced by the applied stress in compression has not be explored.

Since the compressive strength is much higher than the tensile strength, it is naturally desirable to use ceramics under compressive loads. This may be achieved by utilizing materials with high tensile strength, such as carbon-carbon composites, to prestress the ceramics into high compression. The assembly of the prestressed ceramics and the tension members can best be used in high temperature, high operating stress applications such as turbine engine blades and the receiver tubes in central receiver solar thermal power plants. It requires some design changes; however, the

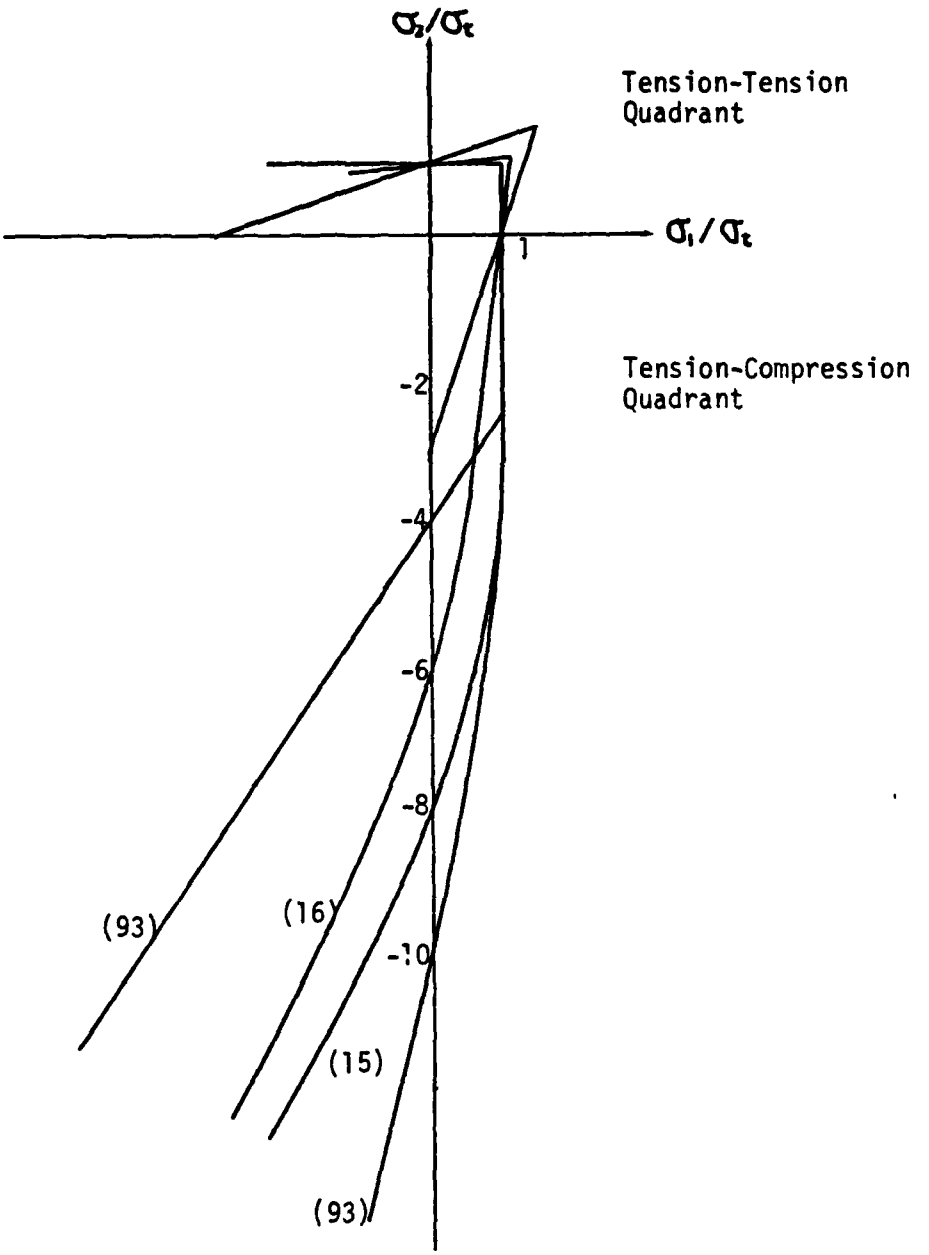

Fig. 5-42 Fracture Criteria in Biaxial Stress Field.
Numbers in parentheses indicate references.

advantage in strength is so great that the extra cost in design change can be easily compensated. If the ceramic materials are used in compression, there might be slow crack growth which ultimately leads to the delayed fracture in compression. Therefore, delayed fracture in compression was briefly studied.

The eccentrically loaded column testing system is capable of maintaining large compressive stresses on the opposite side of the tensile surface of the specimen. The microscopic examination technique was applied to the compressive surface as described in Chapter III. Figure 5-43(a) shows the optical micrograph with the fluorescent dye of a compressive surface after the specimen was loaded at 1,175 MPa for 20 hours. Figure 5-43(b) shows the same area after 114 hours. Although it was expected to see linear arrays of fluorescent dye spots parallel to the compressive loading axis, there was no change observed at this stress level. The scanning electron microscopy was not carried out since no linear array of the fluorescent spots was observed.

The maximum compressive stress on the surface was approximately ten times the maximum tensile stress on the opposite surface; but slow crack growth was not observed on the compressive surface although there was extensive crack growth on the tensile surface. Therefore, it can be concluded that the ceramic material, A(-300, has high resistance to slow crack growth in compression up to 6.5 times the tensile strength.

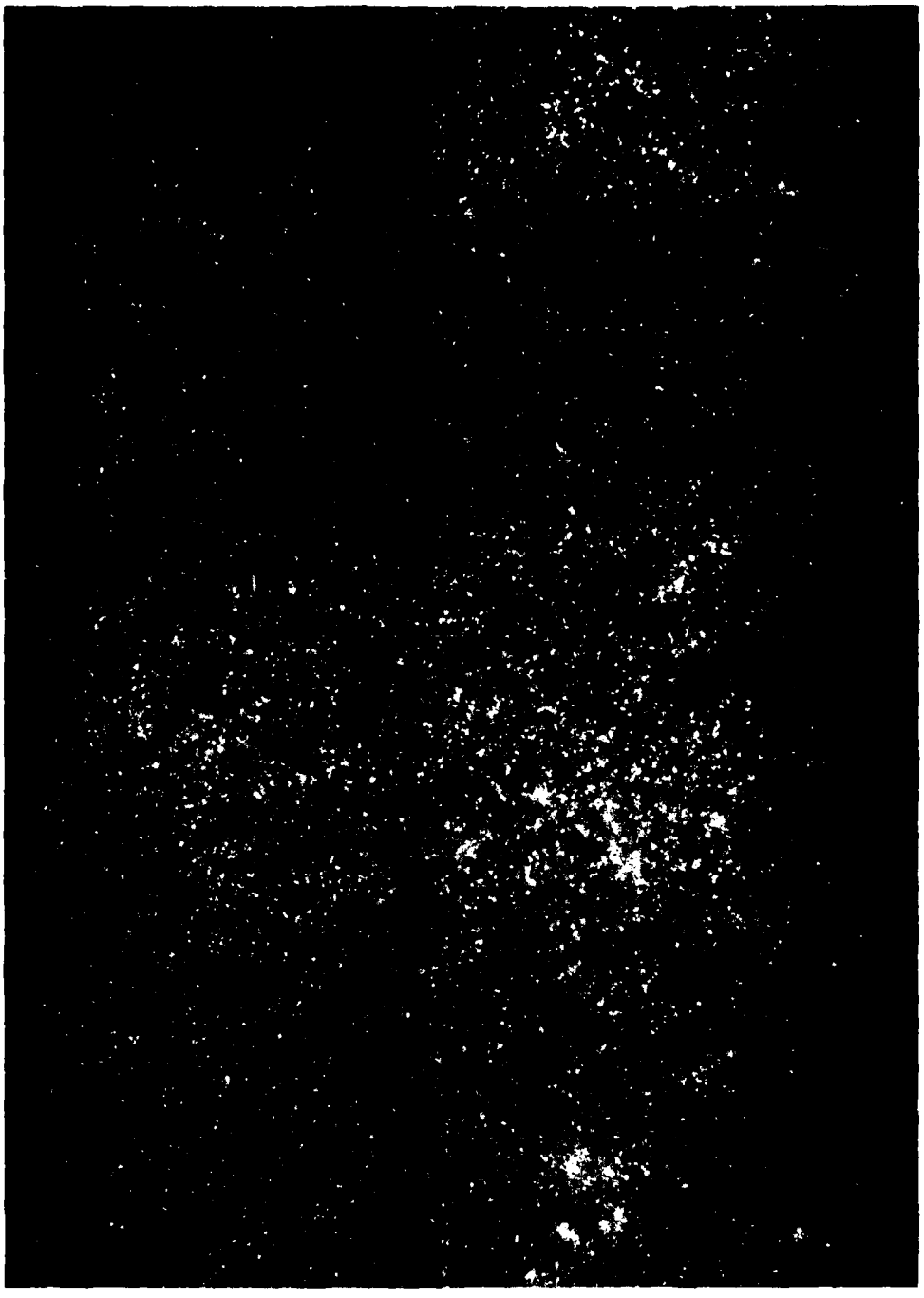

Fig. 5-43 (a) Composite Optical Micrograph with Fluorescent Dye Penetrant on a Compressive Surface after 20 hours at 1,175 MPa.

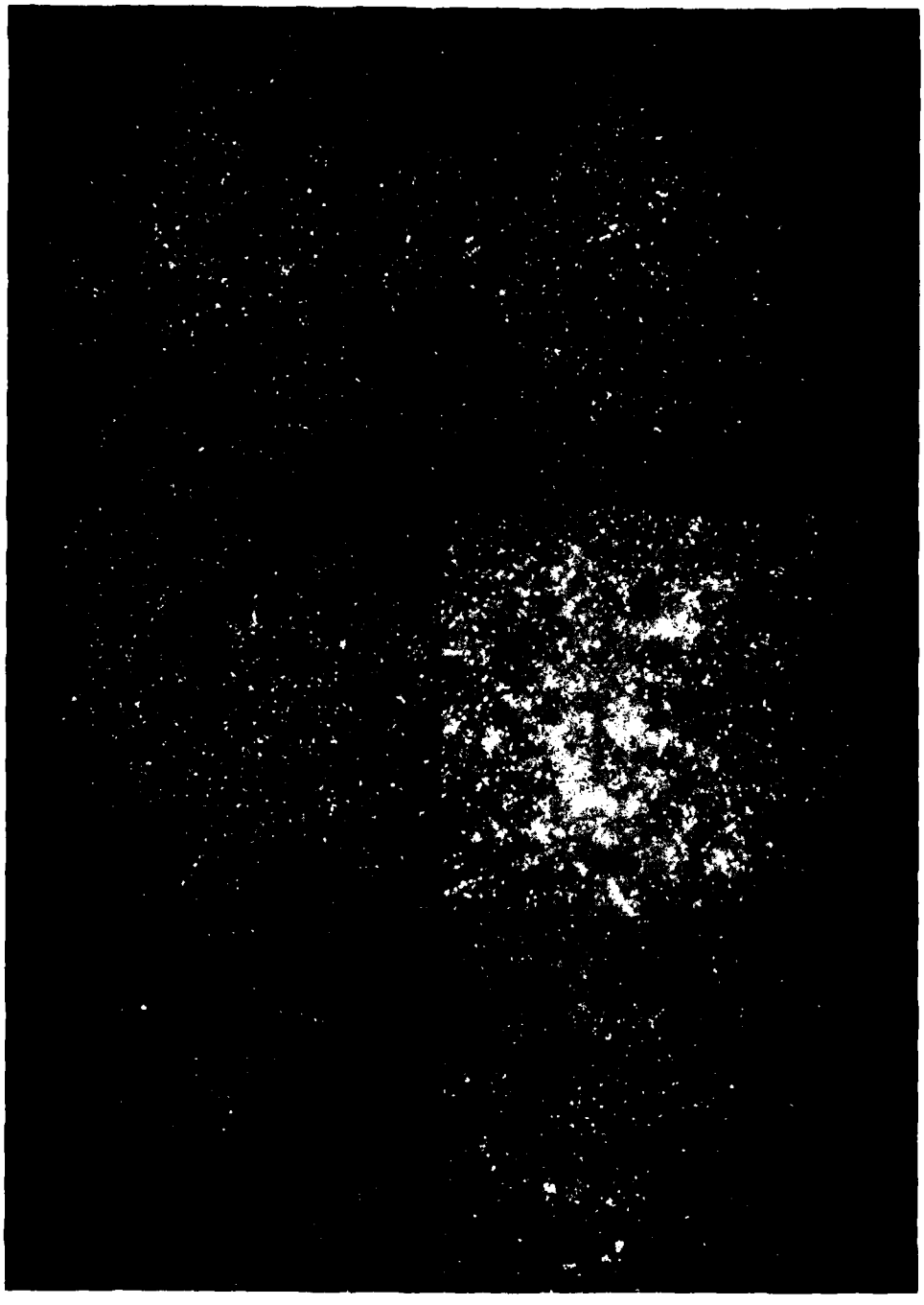

Fig. 5-43 (b) Composite Optical Micrograph with Fluorescent Dye Penetrant on the Compressive Surface Shown in Fig. 5-43 (a) after 114 hours at 1,175 MPa.

CHAPTER VI

CONCLUDING REMARKS

The linear elastic fracture mechanics has been an excellent tool in quantitative analysis of fracture strength and crack growth behavior. However, the author often questioned the validity of simple extrapolation of macroscopic fracture mechanics, where the material is assumed to be homogeneous and isotropic, into the microscopic region, where there are local heterogeneities and anisotropies. In order to verify or refute the validity, it was necessary to directly observe crack origins and microscopic crack growth behavior, not to observe crack tip behavior of a macroscopic crack.

To serve the purpose economically and accurately, the eccentrically loaded column testing apparatus was designed and fabricated, and extensive microscopic examination was conducted. However, the specimens prematurely failed due to inaccurate load path; and the microscopic examination was unsuccessful in the initial stage of the research. It was finally discovered, after an extensive effort, that fluorescent dye could penetrate into a crack only when the penetrant was present at the sites while cracks were forming because the cracks emanating from inherent flaws were so small and tightly closed. Meantime, the other problem of load path accuracy in the eccentrically loaded column

specimen was solved by introducing shallow V-grooves in the loading blocks and by using the positive alignment jig.

Surfaces of the ceramic material, Aℓ-300, contained numerous numbers of inherent flaws. There are some potential crack sites on a surface, especially where some inherent flaws conglomerate. It was found that the crack initiation occurs not necessarily from a single worst flaw, but by interaction and coalescence of near-by flaws after a small amount of crack growth from the individual flaws. The predominant mode of the early stages of slow crack growth was intergranular; it is reasonable because the glassy phase at grain boundaries is more susceptible to the attack by the water in the environment and because the kinetic energy of the crack in the initial stages is so low that crack front can wander easily.

It was also found that the crack sites are multiple in a specimen; therefore, it may be suggested that the worst crack site for the strength test may not be the worst crack site for the delayed fracture test because the microstructural heterogeneity and anisotropy control the local crack velocity in slow crack growth.

The isolated microscopic crack growth law has been developed based upon the concept of the effective critical stress intensity factor. The implication is that a microscopic crack grows rapidly in the very early stage of delayed fracture, denoted Region II, and slows down as it

approaches the macroscopic size in Region III. This phenomenon gives rise to the concept of "stable crack size" for a given grain-sized material. The existence of the stable crack size was confirmed from the experimental observation and from calculation of the critical crack size for the fast fracture test.

The effect of interaction and coalescence of multiple cracks was shown to be significant. It was found that when there are many microscopic cracks close together, the coalescence of the cracks can occur in a very short time without cracks being revealed by non-destructive testing because an amount of subcritical crack growth from the individual inherent flaws can be very small before the coalescence.

The isolated microscopic crack growth law and the interaction and coalescence concept were combined to construct the generalized microscopic crack growth law. The proposed analysis permits calculation of the time-to-failure for many assemblies of cracks. It was demonstrated that the proposed microscopic crack growth model gives much better prediction than the conventional approach. It was also found that in order for the conventional approach to be reasonable, unrealistically large initial cracks had to be assumed; no such cracks were observed in the present study.

Applicability of the existing time-to-failure and the proof testing concepts were reexamined. It was found that

the existing approach gives non-conservative prediction in time-to-failure; but this non-conservative prediction is partially or often excessively compensated by the conservative estimation of the initial crack size. However, there is no guarantee that the compensated prediction comes out conservative.

Some suggestions were made in order to improve resistance to slow crack growth: The material may have a low fracture energy plane in its single crystal, but the majority of the cleavage plane should have higher fracture energies. The conglomeration of inherent flaws must be avoided; it may be achieved by obtaining a uniform microstructure.

Since the compressive strength of ceramics has been known to be much greater than the tensile strength, it is naturally desirable to use ceramics in compression. Therefore, slow crack growth in compression was briefly studies; but no slow crack growth was observed up to compressive stress 6.5 times the tensile strength.

In order to achieve accurate time-to-failure predictions, better understanding of the physical phenomena in microscopic dimensions is important, especially when delayed fracture is involved. The author hopes that the proposed analysis based upon observation of microscopic crack growth will contribute to deeper understanding and better prediction in time-to-failure.

Suggestions for Future Study

There are some topics to be studied in the future regarding the present research:

(1) Instead of the fluorescent dye penetrant, the silver nitrate solution can be used, provided that the problem of corrosion associated with it can be solved. If the silver nitrate solution is used, the specimen can be directly subjected to the scanning electron microscopy; first with the primary mode to locate crack origins, and second with the secondary mode to identify and characterize the flaws. This can greatly reduce the amount of time it takes in tedious work of superimposing the dye spots to the optical micrograph and to the scanning electron micrograph.

(2) Since visual identification of microscopic crack growth has been made, the acoustic emission (AE) might be a useful tool to verify the proposed microscopic crack growth. The microscopic cracks grow rapidly at the beginning and slows down or even arrest, and then grow rapidly again in the macroscopic region. The behavior might be observed using AE. The crack coalescence might be verified by AE, too. When cracks coalesce, the amount of AE must suddenly increase. Then AE decreases after the coalescence unless the coalesced crack is large enough to cause catastrophic failure.

REFERENCES

1. R.P. Wei, "Some Aspects of Environment-Enhanced Fatigue-Crack Growth," Eng. Fract. Mech., 1 (1970) 633-651.
2. R.P. Wei and G.W. Simmons, "Recent Progress in Understanding Environment Assisted Fatigue Crack Growth," Int. Jour. Fract., 17 (1981) 235-247.
3. S.M. Wiederhorn, "Effects of Environment on the Fracture of Glass," Environment-Sensitive Mechanical Behavior, Edited by A.R.C. Westwood and N.S. Stoloff, Gordon and Breach, New York (1966) 293-317.
4. S.M. Wiederhorn, "Subcritical Crack Growth in Ceramics," Fracture Mechanics of Ceramics, vol. 2. Edited by R.C. Bradt, D.P.H. Hasselman, and F.F. Lange, Plenum Press, New York (1974) 613-646.
5. J.B. Watchman Jr., "Highlights of Progress in the Science of Fracture of Ceramics and Glass," Jour. Am. Ceram. Soc., 57 (1974) 509-519.
6. O.L. Anderson and P.C. Grew, "Stress Corrosion Theory of Crack Propagation with Application to Geophysics," Rev. Geophys. Space Phys., 15 (1977) 77-104.
7. C.E. Inglis, "Stresses in a Plate Due to the Presence of Cracks and Sharp Corners," Trans. Inst. Nav. Arch., 55 (1913) 219.

8. A.A. Griffith, "The Phenomena of Rupture and Flow in Solids," Phil. Trans. Roy. Soc. Lond., A221 (1920) 163-198.

9. E. Orowan, "Fundamentals of Brittle Behavior in Metals," Fatigue and Fracture of Metals, John Wiley & Sons, Inc., New York (1952) 139-167.

10. G.R. Irwin, "Fracture Dynamics," Fracturing of Metals, ASM (1948) 147-166.

11. H.M. Westergaard, "Bearing Pressure and Cracks," Jour. Appl. Mech., 6 (1939) 49-54.

12. P.C. Paris and G.C. Sih, "Stress Analysis of Cracks," Fracture Toughness Testing and its Applications, ASTM STP 381, ASTM (1965) 30.

13. G.R. Irwin, "Analysis of Stresses and Strains Near the End of a Crack Traversing a Plate," Jour. Appl. Mech., 24 (1957) 361-364.

14. D.P. Rooke and D.J. Cartwright, Compendium of Stress Intensity Factors, The Hillingdon, Uxbridge, Middx (1976).

15. A.A. Griffith, "Theory of Rupture," Proc. First Int. Cong. for Appl. Mech., Delft (1924) 55-63.

16. H.W. Babel and G. Sines, "Biaxial Fracture Criterion for Porous Brittle Materials," Jour. Basic Eng., 90 (1968) 285-291.

17. L. Grenet, Bull. Soc. Encour. Ind. Mat., 4 (1899) 839, Partial translation may be found in F.W. Preston, "The

Time Factor in the Testing of Glassware," Jour. Am. Ceram. Soc., 18 (1935) 220-224.

18. E.F. Poncelet, "Fracture and Comminution of Brittle Solids," Metals Tech., 11 (1944) 1-20.

19. J.B. Murgatroid, "Mechanism of Brittle Rupture in Glass," Jour. Soc. Glass Tech., 28 (1944) 406-31T.

20. N.W. Taylor, "Mechanism of Fracture of Glass and Similar Brittle Solids," Jour. Appl. Phys., 18 (1947) 943-955.

21. D.A. Stuart and O.L. Anderson, "Dependence of Ultimate Strength of Glass Under Constant Load on Temperature, Ambient Atmosphere, and Time," Jour. Am. Ceram. Soc., 36 (1953) 416-424.

22. R.E. Mould and R.D. South[illegible], "Strength and Static Fatigue of Abraded Glass Under Controlled Ambient Conditions: II, Effect of Various Abrasions and Universal Fatigue Curve," Jour. Am. Ceram. Soc., 42 (1959) 582-592.

23. R.J. Charles and W.B. Hillig, "Kinetics of Glass Failure of Stress Corrosion," Symposium sur la Resistance Mecanique du Verre et les Moyens de l'Ameliorer, Charloeroi, Belgium (1962) 511-527.

24. W.B. Hillig and R.J. Charles, "Surface, Stress-Dependent Surface Reaction, and Strength," High Strength Materials, Edited by V.F. Zackey, John Wiley & Sons, Inc., New York (1965) 682-705.

25. N.I. Muskhelishvili, "Some Basic Problems of the Mathematical Theory of Elasticity," Groningon-Holland (1953) 337.

26. S.M. Wiederhorn and L.H. Boltz, "Stress Corrosion and Static Fatigue of Glass," Jour. Am. Ceram. Soc., 53 (1970) 543-548.

27. R.H. Doremus, "Modification of the Hillig-Charles Theory for Static Fatigue of Glass," Eng. Fract. Mech., 13 (1980) 945-953.

28. T.C. Baker and F.W. Preston, "Fatigue of Glass Under Static Loads," Jour. Appl. Phys., 17 (1946) 170-178.

29. E.B. Shand, "Experimental Study of Fracture of Glass, I, The Fracture Process," Jour. Am. Ceram. Soc., 37 (1954) 52-60.

30. E.B. Shand, "Experimental Study of Fracture of Glass, II, Experimental Data," Jour. Am. Ceram. Soc., 37 (1954) 559-572.

31. A.G. Evans, "A Method for Evaluating the Time-Dependent Failure Characteristics of Brittle Materials--and its Application to Polycrystalline Alumina," Jour. Mat. Sic., 7 (1972) 1137-1146.

32. S.M. Wiederhorn, "Influence of Water Vapor on Crack Propagation in Soda-Lime Glass," Jour. Am. Ceram. Soc., 50 (1967) 407-414.

33. S.M. Wiederhorn, "Prevention of Failure in Glass by

Proof-Testing," Jour. Am. Ceram. Soc., 56 (1973) 227-228.

34. G. Sines, "Rationalized Crack Growth and Time-to-Failure of Brittle Materials," Jour. Am. Ceram. Soc., 59 (1976) 370-371.

35. W.P. Minnear and R.C. Bradt, "(K-V) Diagrams for Ceramic Materials," Jour. Am. Ceram. Soc., 58 (1975) 345-346.

36. S.M. Wiederhorn, H. Johnson, A.M. Diness, and A.H. Heuer, "Fracture of Glass in Vacuum," Jour. Am. Ceram. Soc., 57 (1974) 336-341.

37. S.W. Freiman, K.R. McKinney and H.L. Smith, "Slow Crack Growth in Polycrystalline Ceramics," Fracture Mechanics of Ceramics, Vol. 2, Edited by R.C. Bradt, D.P.H. Hasselman, and F.F. Lange, Plenum Press, New York (1974) 659-676.

38. A.G. Evans and S.M. Wiederhorn, "Proof Testing of Ceramic Materials - An Analytical Basis for Failure Prediction," Int. Jour. Fract., 10 (1974) 379-392.

39. S.M. Wiederhorn, A.G. Evans, E.R. Fuller, and H. Johnson, "Application of Fracture Mechanics to Space-Shuttle Window," Jour. Am. Ceram. Soc., 57 (1974) 319-323.

40. A.G. Evans, "Slow Crack Growth in Brittle Materials Under Dynamic Loading Conditions," Int. Jour. Fract., 10 (1974) 251-259.

41. C.P. Chen, "Fatigue Failure of a Polycrystalline Alumina Ceramic at Several Temperatures," Ph.D. Dissertation, University of California, Los Angeles (1972).

42. W. Weibull, "A Statistical Distribution Function of Wide Applicability," Jour. Appl. Mech., 18 (1951) 293-297.

43. R.W. Davidge, J.R. McLaren, and G. Tappin, "Strength Probability Time (SPT) Relationships in Ceramics," Jour. Mat. Sci., 8 (1973) 1699-1705.

44. L.A. Simpson, "Discrepancy Arising from Measurement of Grain-Size Dependence of Fracture Energy of $A\ell_2O_3$," Jour. Am. Ceram. Soc., 56 (1973) 610-611.

45. L.A. Simpson, I.G. Ritchie, and D.J. Lloyd, "Cause of the Discrepancy Resulting from Testing Methods in the Relation of Grain Size and Fracture Energy in $A\ell_2O_3$," Jour. Am. Ceram. Soc., 58 (1975) 537-538.

46. H. Meredith and P.L. Pratt, "The Observed Fracture Stress and Measured Value of K_{IC} in Commercial Polycrystalline Aluminas," Special Ceramics, Vol. 6, Edited by P. Popper (1975) 107-122.

47. J.G. Bruce and B.G. Koepke, "Evaluation of K_{IC} by the Double-Torsion Technique," Jour. Am. Ceram. Soc., 60 (1977) 284-285.

48. J.P. Singh, A.V. Virkar, D.K. Shetty, and R.S. Gordon, "Strength-Grain Size Relations in Polycrystalline

Ceramics," Jour. Am. Ceram. Soc., 62 (1979) 179-183.

49. A.G. Evans, "A Dimensional Analysis of the Grain-Size Dependence of Strength," Jour. Am. Ceram. Soc., 63 (1980) 115-116.

50. R.W. Rice, S.W. Freiman, and J.J. Mecholsky, Jr., "The Dependence of Strength-Controlling Fracture Energy on the Flaw-Size to Grain-Size Ratio," Jour. Am. Ceram. Soc., 63 (1980) 129-136.

51. A.V. Virkar, D.K. Shetty, and A.G. Evans, "Grain-Size Dependence of Strength," Jour. Am. Ceram. Soc., 64 (1981) C56-C57.

52. T. Soma, M. Matsui, I. Oda, and N. Yamamoto, "Applicability of Crack Propagation Data to Failure Prediction in Porcelain," Jour. Am. Ceram. Soc., 63 (1980) 166-169.

53. U. Lindborg, "A Statistical Model for the Linking of Microcracks," Acta Metal., 17 (1969) 521-526.

54. R.A. Hunt, "A Theory of the Statistical Linking of Microcracks Consistent with Classical Reliability Theory," Acta Metal., 26 (1978) 1443-1452.

55. R. Badaliance and G.D. Gupta, "Growth Characteristics of Two Interacting Cracks," Eng. Fract. Mech., 8 (1976) 341-353.

56. T. Yokobori, T. Yoshida, H. Kuroda, A. Kamei, and S. Konosu, "Non-Linear Interaction Between Main Crack and Near-By Slip Band," Eng. Fract. Mech., 7 (1975) 377-388.

57. T.A. Pucik, "Elastostatic Interaction of Cracks in the Infinite Plate," Ph.D. Dissertation, California Institute of Technology, Pasadena (1972).

58. J.P. Singh, C. Shih, and D.P.H. Hasselman, "Analysis of Effect of Crack Interaction on Nature of Strength Loss in Thermally Shocked Brittle Ceramics," Jour. Am. Ceram. Soc., 64 (1981) C106-109.

59. T.E. Adams, D.J. Landini, C.A. Schumacher, and R.C. Bradt, "Micro- and Macro-Crack Growth in Alumina, Refractories," Ceramic Bull., 60 (1981) 730-735.

60. R.W. Rice, "Processing Induced Sources of Mechanical Failure in Ceramics," Processing of Crystalline Ceramics, Edited by H. Palmour III, R.F. Davis, and T.M. Hare, Plenum Publishing Co. (1978) 303-319.

61. R.W. Rice and J.J. Mecholsky, Jr., "The Nature of Strength Controlling Machined Flaws in Ceramics," NRL Memorandum Report 4077, Naval Research Lab. (1979).

62. R.W. Rice, J.J. Mecholsky, S.W. Freiman, and S.M. Morey, "Failure Causing Defects in Ceraminics: What NDE Should Find," NRL Memorandum Report 4075, Naval Research Lab. (1979).

63. H.P. Kirchner and R.M. Gruver, "Fracture Mirrors in Polycrystalline Ceramics and Glass," Fracture Mechanics of Ceramics, Vol. 1, Edited by R.C. Bradt, D.P.H. Hasselman, and F.F. Lange, Plenum Press, New York (1973) 309-321.

64. R.W. Rice, "Fractographic Identification of Strength Controlling Flaws and Microstructure," Fracture Mechanics of Ceramics, Vol. 1, Edited by R.C. Bradt, D.P.H. Hasselman, and F.F. Lange, Plenum Press, New York (1973) 323-345.

65. R.W. Rice, "Fracture Topography of Ceramics," Materials Science Research, VII, Edited by V.D. Frechette, W.C. LaCourse, and V.L. Burdick, Plenum Press, New York (1974) 439-472.

66. V.D. Frechette, "Characteristics of Fracture-Exposed Surfaces," Proc. Brit. Ceram. Soc., 5 (1965) 97-106.

67. Lih-Jou Chung, "A Fractographic Study of Pure Dense Aluminum Oxide," Master's Thesis, University of California, Los Angeles (1979).

68. M.J. Noone and R.L. Mehan, "Observation of Crack Propagation in Polycrystalline Ceramics and its Relationship to Acoustic Emissions," Fracture Mechanics of Ceramics, Vol. 1, Edited by R.C. Bradt, D.P.H. Hasselman, and F.F. Lange, Plenum Press, New York (1973) 201-229.

69. Magnaflux Corporation, "Fluorescent Penetrant Testing," Chicago, Ill. (1977).

70. D.J. Green, Private Communication.

71. G. Sines and M. Adams, "Compression Testing of Ceramics," Fracture Mechanics of Ceramics, Vol. 3, Edited by R.C. Bradt, D.P.H. Hasselman, and F.F. Lange,

Plenum Press, New York (1978) 403-434.

72. O. Schwaninger, "A 2000-Ton Compression Testing Machine," Proc. Inst. Mech. Eng., 180, Part 3A (1965) 380-387.

73. C.D. Pears and F.S. Digesu, "Gas-Bearing Facilities for Determining Axial Stress-Strain and Lateral Strain of Brittle Materials to 5500 F," ASTM Proc., 65 (1965) 885-873.

74. H.Y.B. Mar and W.D. Scott, "Fracture Induced in $A\ell_2O_3$ Bicrystals by Anisotropic Thermal Expansion," Jour. Am. Ceram. Soc., 53 (1970) 555-558.

75. H.P. Kirchner and J.M. Ragosta, "Crack Growth From Small Flaws in Larger Grains in Alumina," Jour. Am. Ceram. Soc., 63 (1980) 490-495.

76. D.J. Green, "Strength/Sonic Velocity Correlation for LI2200 Space Shuttle Tiles," Presented at the 34th Pacific Coast Regional Meeting, Newport Beach, CA (1981).

77. S.M. Wiederhorn, "Fracture of Sapphire," Jour. Am. Ceram. Soc., 52 (1969) 485-491.

78. E. Schmid and W. Boas, "Plasticity of Crystals, English Translation by Chapman and Hall (1950) 169.

79. P.F. Becher, "Fracture-Strength Anisotropy of Sapphire," Jour. Am. Ceram. Soc., 59 (1976) 59-61.

80. R.C. Pohanka, S.W. Freiman, and B.A. Bender, "Effect of the Phase Transformation on the Fracture Behavior

of $BaTiO_3$," Jour. Am. Ceram. Soc., 61 (1978) 72-75.

81. R.G. Hoagland and J.D. Embury, "Treatment of Inelastic Deformation Around a Crack Tip Due to Microcracking," Jour. Am. Ceram. Soc., 63 (1980) 404-410.

82. C.J. Tranter, "The Opening of a Pair of Coplanar Griffith Cracks Under Internal Pressure," Quart. Jour. Mech. and Appl. Math., Vol. XIV (1961) 283-292.

83. F.F. Lange, "Transformation Toughening," in five parts, to be published in Jour. Mat. Sci., 1982.

84. A.G. Evans and K.T. Faber, "Toughening of Ceramics by Circumferential Microcracking," Jour. Am. Ceram. Soc., 64 (1981) 394-398.

85. I. Aksay and F.F. Lange, "Colloidal/Filteration Consolidation Route to Unform Ceramic Microstructure," to be published.

86. M. Srinivasan, R.H. Smoak, and J.A. Coppola, "Static Fatigue Resistance of Sintered Alpha SiC," Am. Ceram. Soc. Bull., 57 (1978) 1064.

87. K.R. McKinney, J.J. Mecholsky, and S.W. Freiman, "Delayed Failure in Chemically Vapor Deposited ZnSe," Jour. Am. Ceram. Soc., 62 (1979) 336-340.

88. R.K. Govila, K.R. Kinsman, and P. Beardmore, "Phenomenology of Fracture in Hot-Pressed Silicon Nitride," Jour. Mat. Sci., 14 (1979) 1095-1102.

89. J.J. Mecholsky, "Intergranular Slow Crack Growth in MgF_2," Jour. Am. Ceram. Soc., 64 (1981) 563-566.

90. H.P. Kirchner and R.M. Gruver, "Fractographic Criteria for Subcritical Crack Growth Boundaries in 96% $A\ell_2O_3$," Jour. Am. Ceram. Soc., 63 (1980) 169-174.

91. R.W. Rice, "The Compressive Strength of Ceramics," Materials Science Research, Vol. 5, Plenum Press, New York (1971) 195-229.

92. M.A. Adams, "The Strength of Brittle Ceramics in Compressive Stress States," Ph.D. Dissertation, University of California, Los Angeles (1972).

93. F.A. McClingtock and J.B. Walsh, "Friction on Griffith Cracks in Rocks Under Pressure," Proc. of the Fourth U.S. National Congress of Applied Mech. (1962) 1015-1021.

94. B. Cotterel, "Brittle Fracture in Compression," Int. Jour. Fract., 8 (1972) 192-208.

Appendix A. Time-to-Failure

1. Time-to-failure under constant load

For slow crack growth, relationship between velocity of the crack and the stress intensity factor can be given

$$v = \frac{da}{dt} = B\left(\frac{K_I}{K_{IC}}\right)^n \qquad \text{for region I} \tag{A-1}$$

$$v = \frac{da}{dt} = v_T \qquad \text{for region II}$$

where B, v_T = constant

n = crack growth exponent

The stress intensity factor can be expressed

$$K_I = Y\sigma a^{1/2} \tag{A-2}$$

where Y = geometrical factor

Under constant σ, the time-to-failure t_f is given by integrating eq. (A-1)

$$t_f = \int dt = \int_{a_i}^{a_c} \frac{da}{v} \tag{A-3}$$

where a_i = initial crack size

a_c = critical crack size

Rewriting eq. (A-2)

$$dK_I = \frac{1}{2} Y\sigma \left(\frac{1}{a}\right)^{1/2} da$$

or

$$da = \frac{2K_I}{\sigma^2 Y^2} dK_I$$

Substituting into eq. (A-3)

$$t_f = \frac{2}{Y^2\sigma^2} \int_{K_{Ii}}^{K_{IC}} \frac{K_I}{v} dK_I$$

Then

$$t_f = \frac{2}{Y^2\sigma^2} \left\{ \frac{K_{IC}^n}{B} \int_{K_{Ii}}^{K_T} K_I^{(1-n)} dK_I + \frac{1}{B'} \int_{K_T}^{K_{IC}} K_I dK_I \right\} \qquad \text{(A-4)}$$

where K_T = stress intensity factor at transition of region I and II

Since most of the life is spent in region I, eq. (A-4) becomes

$$t_f = \frac{2K_{IC}^n}{Y^2\sigma^2 B(n-2)} \left\{ K_{Ii}^{(2-n)} - K_T^{(2-n)} \right\} \qquad \text{(A-5)}$$

In general, n is a large number (n > 20 typically) then

$$t_f \approx \frac{2K_{IC}^n K_{Ii}^{(2-n)}}{Y^2 \sigma^2 B(n-2)}$$

or

$$t_f \approx C \frac{a_i^{\left(\frac{2-n}{2}\right)}}{\sigma^n}$$

where

$$C = \frac{2K_{IC}^n}{Y^n B(n-2)}$$

Therefore, if the initial crack size is known, the time-to-failure is obtained from eq. (A-6). Instead of measuring actual a_i, proof stress σ_p can be used to assume the initial crack size. If we apply the proof stress σ_p which is somewhat higher than σ, the maximum possible crack size which barely survived the proof stress can be obtained as follows:

$$K_{IC} = Y\sigma_p a_i^{1/2} \tag{A-7}$$

Thus

$$a_i = \left(\frac{K_{IC}}{Y\sigma_p}\right)^2$$

or

$$K_{Ii} = \frac{\sigma}{\sigma_p} K_{IC} \tag{A-8}$$

Therefore, eq. (A-6) becomes

$$t_f = \frac{2K_{IC}^2 \sigma_p^{(n-2)}}{Y^2 \sigma^n B(n-2)} \tag{A-9}$$

2. Time-to-failure under constant stress rate σ

From eq. (A-2)

$$K_I = Y\sigma a^{1/2} \tag{A-2}$$

The crack velocity can be given in relation with the stress rate as follows

$$\frac{da}{dt} = \left(\frac{\partial a}{\partial \sigma}\right)_K \frac{d\sigma}{dt} \tag{A-10}$$

The other partial derivatives vanish for constant stress rate conditions because K is a unique function of v. Rewriting eq. (A-10) gives

$$d\sigma = \frac{\sigma}{v}\, da \tag{A-11}$$

From eq. (A-1)

$$\begin{aligned} v &= B\left(\frac{K_I}{K_{IC}}\right)^n && \text{for region I} \\ v &= v_T && \text{for region II} \end{aligned} \tag{A-1}$$

But it was shown by Evans[40] that the crack growth after region II occurs at constant stress. Therefore, only region I is considered in this Appendix. Then

$$v = B\left(\frac{Y\, a^{1/2}}{K_{IC}}\right)^n \tag{A-12}$$

Substituting eq. (A-12) for eq. (A-11) and integrating

$$\int_0^{\sigma_f} \sigma^n d\sigma = \frac{\dot{\sigma} K_{IC}^n}{B Y^n} \int_{a_i}^{a_c} \left(\frac{1}{a}\right)^{\frac{n}{2}} da$$

or

$$\frac{\sigma_f^{n+1}}{n+1} = \frac{2\dot{\sigma} K_{IC}^n}{B\, Y^n (2-n)} \left\{ \left(\frac{1}{a_c}\right)^{\frac{n}{2}-1} - \left(\frac{1}{a_i}\right)^{\frac{n}{2}-1} \right\} \tag{A-13}$$

Since n is a large number, eq. (A-13) reduces to

$$\sigma_f = \{\frac{2\dot{\sigma}K_{IC}^n(n+1)}{BY^n(n-2)} (\frac{1}{a_i})^{\frac{n}{2}-1}\}^{\frac{1}{n+1}} \quad \text{(A-14)}$$

If we use the concept of initial strength σ_f^*, the fracture strength without slow crack growth,

$$a_i = \frac{K_{IC}^2}{Y^2\sigma_f^{*2}} \quad \text{(A-15)}$$

Then eq. (A-14) becomes

$$\sigma_f = \{\frac{2\dot{\sigma}K_{IC}^2(n+1)\sigma_f^{*(n-2)}}{BY^2(n-2)}\}^{\frac{1}{n+1}} \quad \text{(A-16)}$$

or

$$\sigma^* = \{\frac{BY^2(n-2)\sigma_f^{n+1}}{2\dot{\sigma}K_{IC}^2(n+1)}\}^{\frac{1}{n-2}} \quad \text{(A-17)}$$

Since σ_f in eq. (A-16) is the observed fracture strength, this may be combined with the statistical strength distribution given in eq. (2-23)

$$P = 1 - \exp[-(\frac{\sigma_f - \sigma_u}{\sigma_v})^m] \quad \text{(A-18)}$$

When $\sigma_u = 0$, eq. (A-18) may be written as

$$\log\log[1/(1-P)] = m\log\sigma_f + C \quad \text{(A-19)}$$

$$C = \log\log e - m\log\sigma_v$$

Equation (A-19) is combined with (A-16)

$$\log \log [1/(1-P)] = m \log \frac{2\dot{\sigma} K_{IC}^2 (n+1) \sigma_f^{*(n-2)}}{B Y^2 (n-2)} \frac{1}{n+1} + C$$

or (A-20)

$$\log \frac{\sigma_f^*}{K_{IC}} = \frac{n+1}{m(n-2)} \{\log \log [1/(1-P)] - C\}$$

$$- \frac{1}{n-2} \log \frac{2\dot{\sigma} K_{IC}^n (n+1)}{B Y^2 (n-2)} \quad \text{(A-21)}$$

Equation (A-21) describes the initial strength distribution in the absence of subcritical crack growth. Since the initial stress intensity factor can be written as

$$K_{Ii} = Y\sigma\sqrt{a_i} \quad \text{(A-22)}$$

and

$$K_{IC} = Y\sigma_f^*\sqrt{a_i} \quad \text{(A-23)}$$

then combining eq. (A-22) and eq. (A-23),

$$K_{Ii} = \frac{K_{IC}}{\sigma_f^*} \quad \text{(A-24)}$$

Substituting eq. (A-24) into eq. (A-21)

$$\log K_{Ii} = \log\sigma + \frac{1}{n-2} \log \frac{2\dot{\sigma} K_{IC}^n (n+1)}{B Y^2 (n-2)}$$

$$- \frac{n+1}{m(n-2)} \{\log \log [1/(1-P)] - C\} \quad \text{(A-25)}$$

From eq. (A-6)

$$\log t_f = \log \frac{2K_{IC}^n}{Y^2\sigma^2 B(n-2)} - (n-2)\log K_{Ii} \qquad \text{(A-26)}$$

Substituting eq. (A-25) into eq. (A-26), the time-to-failure is given by

$$\log t_f = \log \frac{1}{\sigma^n (n+1)\dot{\sigma}} + \frac{n+1}{m}\{\log\log[1/(1-P)] - C\} \qquad \text{(A-27)}$$

Appendix B. Power Series Expression for Elliptic Integrals

1. The elliptic integral of the first kind.

$$K_{(k,\phi)} \equiv \int_0^{\phi} \frac{d\theta}{\sqrt{1-k^2\sin^2\theta}} \qquad k^2 < 1 \qquad \text{(B-1)}$$

The integrand of the integral may be expanded in the binomial theorem in the form

$$(1-k^2\sin^2\theta)^{-1/2} = 1 + \frac{k^2}{2}\sin^2\theta + \frac{3k^4}{8}\sin^4\theta + \ldots \qquad \text{(B-2)}$$

for $k^2 < 1$.

In our case

$$k = \sqrt{1-\alpha^2}$$

where $\alpha = \frac{1-a/b}{1+a/b}$

Since a convergent series

$$1 + \frac{k^2}{2} + \frac{3k^4}{8} + \ldots$$

serves as an M series, (B-2) is uniformly convergent in any interval of θ; therefore, we can integrate (B-1) term by term to obtain

$$K_{(k,\phi)} = \phi + \frac{k^2}{2}\int_0^{\phi} \sin^2\theta d\theta + \frac{1.3}{1.2}k^4\int_0^{\phi}\sin^2\theta d\theta + \ldots$$

$$\ldots + \frac{1x3x5\ldots(2n-1)}{2x4x6\ldots2n}k^{2n}\int_0^{\phi}\sin^{2n}\theta d\theta \qquad \text{(B-3)}$$

For the complete elliptic integral of the first kind, by Wallis' formula

$$\int_0^{\frac{\pi}{2}}\sin^m\theta d\theta = \frac{1x3x5\ldots x(m-1)}{2x4x6x\ldots xm}\frac{\pi}{2}$$

Since m is an even integer (m = 2n) in our case, we have

$$K_{(k)} = \frac{\pi}{2}[1 + (\frac{1}{2})^2k^2 + (\frac{1x3}{2x4})^2k^4 + \ldots$$

$$+ \{\frac{1x3x5x\ldots x(2n-1)}{2x4x\ldots x2n}\}^2 k^{2n}] \qquad \text{(B-4)}$$

The elliptic integral of the second kind

$$E_{(k,\phi)} \equiv \int_0^{\phi}\sqrt{1 - k^2\sin^2\theta}\, d\theta \qquad k^2 < 1 \qquad \text{(B-5)}$$

Similarly, by the binomial theorem

$$(1 - k^2\sin^2\theta)^{1/2} = 1 - \frac{1}{2}k^2\sin^2\theta - \frac{1}{8}k^4\sin^4\theta\ldots$$

and the final expression is

$$E_{(k,\phi)} = \phi - \frac{k^2}{2}\int_0^{\phi}\sin^2\theta d\theta - \frac{k^4}{2.4}\int_0^{\phi}\sin^4\theta d\theta$$

$$- \frac{1x3x5\ldots(2n-3)}{2x4\ldots2n}k^{2n}\int_0^{\phi}\sin^{2n}\theta d\theta \qquad \text{(B-6)}$$

For the complete elliptic integral of the second kind, similarly we have,

$$E_{(k)} = \frac{\pi}{2}[1 - (\frac{1}{2})^2k^2 - (\frac{1}{8})(\frac{3}{8})\,k^4 - \ldots.$$

$$- \frac{1x3x\ldots x(2n-1)}{2x4x\ldots x2n}\,\frac{1x3x\ldots x(2n-3)}{2x4x\ldots x2n}\,k^{2n}]$$

or

$$E_{(k)} = \frac{\pi}{2}[1 - (\frac{1}{2})^2k^2 - (\frac{3}{8})^2\,\frac{k^4}{3} - \ldots.$$

$$- \{\frac{1x3x\ldots x(2n-1)}{2x4x\ldots x2n}\}^2\,\frac{k^{2n}}{2n-1}] \qquad \text{(B-7)}$$

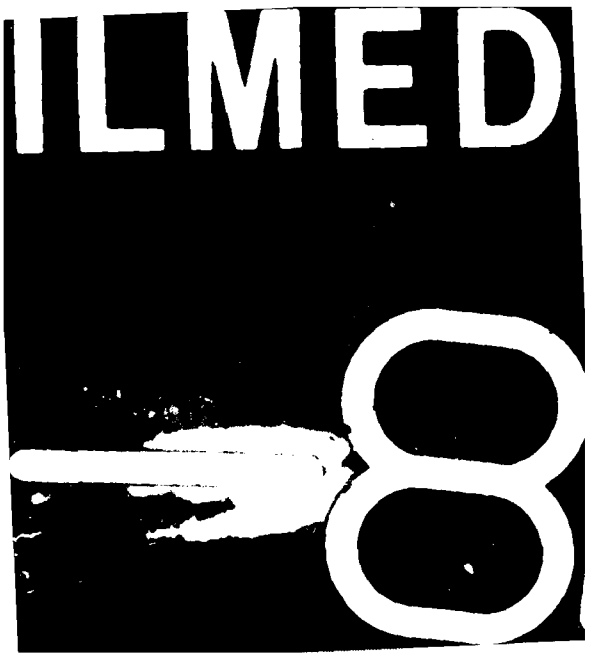
ILMED
8